Jagiellonian University in Kraków
Faculty of Physics, Astronomy and Applied Computer Science

NON-INVASIVE BEAM DIAGNOSTICS WITH SCHOTTKY SIGNALS AND CHERENKOV DIFFRACTION RADIATION

PhD Thesis

BY
KACPER ŁASOCHA

Prepared under the supervision of:
Dr Diogo Miguel Louro Alves
Prof. Dr hab. Elżbieta Richter-Wąs

Kraków, Poland
2022

Version corrected after the original submission

Oświadczenie

Ja, niżej podpisany Kacper Łasocha (nr indeksu: 1090941), doktorant Wydziału Fizyki, Astronomii i Informatyki Stosowanej Uniwersytetu Jagiellońskiego oświadczam, że przedłożona przeze mnie rozprawa doktorska pt. „Non-Invasive Beam Diagnostics with Schottky Signals and Cherenkov Diffraction Radiation'' jest oryginalna i przedstawia wyniki badań wykonanych przeze mnie osobiście, pod kierunkiem dr. Diogo Alvesa oraz prof. dr hab. Elżbiety Richter-Wąs. Pracę napisałem samodzielnie.

Oświadczam, że moja rozprawa doktorska została opracowana zgodnie z Ustawą o prawie autorskim i prawach pokrewnych z dnia 4 lutego 1994 r. (Dziennik Ustaw 1994 nr 24 poz. 83 wraz z późniejszymi zmianami).

Jestem świadom, że niezgodność niniejszego oświadczenia z prawdą ujawniona w dowolnym czasie, niezależnie od skutków prawnych wynikających z ww. ustawy, może spowodować unieważnienie stopnia nabytego na podstawie tej rozprawy.

Kraków, dnia ....

(podpis doktoranta)

STRESZCZENIE

W rozprawie przedstawiono postępy dokonane w dwóch technikach nieinwazyjnej diagnostyki wiązki, analizie sygnałów Schottky'ego i obserwacji dyfrakcyjnego promieniowania Czerenkowa (ChDR).

Sygnały Schottky'ego przejawiają się w natężeniu wiązki w postaci szumu statystycznego, który można analizować po przetworzeniu na domenę częstotliwości. Analiza sygnałów Schottky'ego jest fundamentalną techniką pomiaru parametrów ciągłych wiązek hadronów, ale zadanie to jest znacznie trudniejsze w przypadku wiązek przyspieszanych systemami RF, czyli posiadających strukturę paczek. W rozprawie doktorskiej zaproponowano i rozwinięto nowe podejście oparte na symulacji sygnałów Schottky'ego i porównywaniu ich z uzyskanymi eksperymentalnie. Odpowiednie charakterystyki wiązki służą jako parametry wejściowe do symulacji, a przy pomocy procedur optymalizacyjnych dopasowuje się wartości, które najlepiej odtwarzają mierzone rozkłady sygnałów Schottky'ego. Proponowane podejście zostało zastosowane do danych uzyskanych przez monitor sygnałów Schottkyego w Wielkim Zderzaczu Hadronów (LHC) i porównane z wynikami alternatywnych technik pomiarowych. Usystematyzowano również pewne elementy teorii opisującej sygnały Schottky'ego dla wiązek o strukturze paczek. Pozwoliło to na formalne wyprowadzenia zależności między szerokością spektralną widma Schottky'ego a wartością chromatyczności wiązki.

W drugiej części rozprawy omówiono zastosowanie dyfrakcyjnego promieniowania Czerenkowa w diagnostyce wiązki. Koncepcja ta jest stosunkowo nowa i nadal wymaga szeroko zakrojonych badań zarówno z teoretycznego, jak i praktycznego punktu widzenia. Po krótkiej prezentacji dotychczas stosowanych teoretycznych modeli emisji ChDR w prostych geometriach, przedstawione są systematyczne badania jak parametry wiązki wpływają na właściwości emitowanego promieniowania. Uzupełnieniem tego jest opis nowego modelu półanalitycznego, który pozwala na obliczenie oczekiwanej intensywności promieniowania w przypadku bardziej złożonych wielowarstwowych radiatorów, i wypełnia lukę między uproszczonymi modelami teoretycznymi, a często bardzo czasochłonnymi szczegółowymi symulacjami. Możliwości zaproponowanej metody ilustrują badania wpływu cienkich powłok osadzonych na powierzchni radiatora, zarówno w celu wzmocnienia sygnału, jak i złagodzenia niepożądanych efektów, takich jak tworzenie się chmur elektronowych. W dalszych rozdziałach pracy przedyskutowano możliwości zastosowania urządzeń diagnostycznych opartych na ChDR w Wielkim Zderzaczu Hadronów. Drugą część rozprawy kończy opis dedykowanego eksperymentu przeprowadzonego w 2021 roku na akceleratorze CLEAR w CERN, którego celem było zrozumienie zakresu stosowalności obecnie używanych modeli teoretycznych ChDR. Przedstawiono analizę wyników eksperymentu, które nie potwierdzają weryfikowanych modeli i mogą stanowić punkt wyjściowy do dalszych badań nad zastosowaniem ChDR w diagnostyce wiązki.

ABSTRACT

This dissertation reports on the developments made regarding two techniques used for non-invasive beam diagnostics: the analysis of Schottky signals and the observation of Cherenkov Diffraction Radiation (ChDR).

The Schottky signal manifests itself in the beam intensity in the form of statistical noise, which is typically more conveniently analysed in frequency domain. The analysis of Schottky signals is a fundamental technique for estimating various physical parameters of unbunched hadron beams, but the task is far more challenging in the case of beams accelerated with RF systems, i.e. bunched beams. A new approach based on simulating Schottky signals and comparing them with the experimentally obtained ones is proposed and developed herein. The relevant beam characteristics serve as input parameters for the simulations, and with the help of optmisation routines one obtains the values which fit best to the measured Schottky signals. The proposed approach has been applied to the data acquired by the LHC Schottky Monitor and benchmarked against the results of alternative measurement techniques. The theory of Schottky signals in the presence of bunched beams is revisited as well, and a formal derivation of the relation between the width of the synchro-betatron sidebands in the Schottky spectrum and the value of chromaticity is presented.

The second part of this dissertation discusses the application of Cherenkov Diffraction Radiation in beam diagnostics. The concept is relatively new and still requires extensive studies from both theoretical and practical points of view. A brief presentation of the theoretical models used so far for describing ChDR emission in simple geometries is followed by a systematic study of how relevant beam parameters express themselves in the properties of the emitted radiation. This is supplemented with the development of a new semi-analytical framework, which allows for calculation of the expected radiation yield in the case of a more complex multilayered radiator, and fills the gap between simplified theoretical models and detailed numerical simulations, which often require large computing resources. The performance of the new framework is illustrated with studies on the impact of thin coatings deposited on the radiator surface, either for signal enhancement or to mitigate undesirable effects, such as the creation of electron clouds. In addition, the feasibility of using ChDR-based diagnostic devices in the Large Hadron Collider is preliminarily assessed. This part of the thesis is concluded with the results of a dedicated experiment carried out in 2021 on the CLEAR accelerator at CERN, whose aim was to understand the range of validity of the currently used theoretical models. The obtained results do not confirm the investigated theoretical models and may constitute a starting point for further research on the use of ChDR in beam diagnostics.

PREFACE

This dissertation has been completed in process of my PhD studies at the Faculty of Physics, Astronomy and Applied Computer Science of Jagiellonian University. During this time I had a chance to spend three years in CERN's Beam Instrumentation Group in the framework of CERN Doctoral Student Programme. The results obtained during this time form the core of this thesis.

The first project in which I was involved focused on the analysis of the LHC Schottky spectra. Although the LHC Schottky Monitor was commissioned in 2011, the chromaticity measurements it provided were not precise, and the LHC operators preferred an alternative invasive method estimating the machine chromaticity. One of the reasons for such a situation was a missing important component in the developed theory of Schottky signals. The same procedure for deriving the value of chromaticity from the Schottky spectrum was used both in the cases of bunched and coasting beams, but was justified by the theory only in the second case. My initial goal was to develop an independent method for estimating chromaticity from the measured Schottky signals. This was achieved with the *spectral fitting procedure* I developed, and is described in subsection 2.3.1. In addition, and before using it for chromaticity estimates, the new spectral fitting procedure was applied to the longitudinal Schottky spectrum demonstrating a novel application of the LHC Schottky Monitor - as a longitudinal bunch profile monitor. Furthermore, as I revisited the theory of Schottky signals, the original procedure for chromaticity estimation from the Schottky spectrum was proved in the case of bunched beam and benchmarked against the developed spectrum fitting procedure.

My contributions in the area of Schottky signal analysis were done in a close collaboration with my CERN supervisor Dr Diogo Alves. As a summary, the highlights of my contributions contain the following aspects presented in this thesis:

- Detailed and systematic derivation of the Schottky signal formulae, concluded with proving the *chromaticity formula* for the case of bunched beams and addressing special cases for which it is not valid— subsections 2.2.1 to 2.2.3.

- Development of the matrix formalism, based on which multi-particle Schottky spectra can be calculated from a set of single particle spectra and distribution of synchrotron amplitudes by simple matrix multiplication. It enabled the estimation of beam and machine parameters based on the spectral fitting procedure, in which the parameters are determined with optimisation routines so that a representative metric of the difference between the simulated and the measured spectrum is minimised — subsection 2.3.1.

- Proposing a new robust procedure for the Schottky-based betatron tune calculation — subsection 2.3.2.

- Benchmarking the spectrum fitting procedure applied to the longitudinal Schottky spectra against the results obtained with a wall current monitor — subsection 2.4.1.
- Benchmarking the *chromaticity formula* and a range of spectrum fitting procedure variations applied to the transverse Schottky spectra, against the reference RF-based measurement of chromaticity — subsection 2.4.2.
- Proposing a new approach for reducing the magnitude of spurious coherent components within the Schottky spectrum by gating signals of specifically located bunches — Section 2.5.

The results of this work have been published in two peer-reviewed articles:

1. K. Lasocha, D. Alves, "Estimation of longitudinal bunch characteristics in the LHC using Schottky-based diagnostics", *Phys. Rev. Accel. & Beams* 23, 062803, Jun 2020,
2. K. Lasocha, D. Alves, "Estimation of transverse bunch characteristics in the LHC using Schottky-based diagnostics", *Phys. Rev. Accel. & Beams* 25, 062801, June 2022,

and presented in two talks:

1. "Estimation of Longitudinal Profiles of Ion Bunches in the LHC Using Schottky-Based Diagnostics" at the 8th International Beam Instrumentation Conference, Malmo, Sep 2019 (talk given by D. Alves due to absence of K. Lasocha)
2. "Schottky Noise Diagnostics" at Accelerators' Department seminar, SOLARIS National Synchrotron Radiation Centre, Krakow, Apr 2021.

In parallel, I was involved in the activities of an international endeavour investigating possibilities that Cherenkov diffraction radiation (ChDR) brings to beam diagnostics. The research group, under the leadership of Dr Thibaut Lefèvre, at the moment when I joined had already obtained notable results in the field, such as the first observation of the incoherent ChDR induced by a particle beam or demonstration of bunch length measurements based on coherent ChDR.

My first task was related to the problem of estimating the expected ChDR yield in the presence of thin metallic coatings on the radiator surface. This was motivated by certain theoretical results, which have suggested the possibility of transforming the ChDR spectrum through the excitation of surface plasmon polaritons and significantly enhancing the radiation yield in a narrow frequency range. Based on IW2D, the existing framework for beam impedance calculations in multilayered accelerator structures, I have developed an extension, which allowed for calculation of the EM field in an arbitrary location around the beam. The developed code facilitated investigations of

the impact of radiator coatings on ChDR yield. In particular, it allowed for the determination of beam-radiator configurations that would result in the creation of surface plasmon polariton ChDR resonances, as well as studying the ChDR signal reduction due to the presence of coatings used in accelerator structures for electron-cloud prevention.

In order to cross-validate results of the IW2D calculations, I have compared them to certain previously established theoretical models describing ChDR for simple geometries, obtaining absolute agreement. The mentioned theoretical results, grouped under the name *stationary models*, had not been known before to our team and became a convenient tool for preliminary radiation yield estimation, supporting the previously used *Polarization Current Approach* (PCA), a method developed at Tomsk Polytechnic University in the end of the 2000s.

Studying the spectral distribution of the energy radiated in the form of ChDR as predicted by stationary models and PCA, I observed that although the predictions qualitatively match in the case of low-frequency radiation, the results diverge for high frequencies. This discrepancy was not straightforward to notice, as interest in the field of beam diagnostics was usually focused on the more intensive low-frequency coherent part of the spectrum. However, the difference would become significant in the case of future high-energy lepton accelerators, where diagnostics based on incoherent radiation is feasible. To answer the question of which approach better describes the real-case scenario, I have proposed an experiment to be conducted at CERN's CLEAR facility, for which the beam and radiator properties were chosen in a way to highlight differences between both theoretical models. The experiment was carried out in autumn 2021 and revealed a limited direct applicability of both approaches for this real-case scenario.

Among my contributions in the field of ChDR, presented in this thesis, one can include the following:

- Identifying and analysing theoretical results that might be used for the ChDR yield estimation and benchmarking further results, combined with a systematic review of impact of the relevant beam parameters on ChDR, in collaboration with A. Schlögelhofer — subsection 3.2.1 and Section 3.3.

- Developing the extension to IW2D software, which facilitated the calculation of EM fields in multi-layered structures, and benchmarking its results against established theoretical results, in collaboration with N. Mounet — subsections 3.4.1 to 3.4.4.

- Demonstration of the possibilities that the extended version of IW2D brings to beam diagnostic studies: simulation of ChDR induced by surface plasmon polaritons and estimation of the

reduction of radiation yield due to the presence of specific coatings used to prevent electron cloud build-up — subsections 3.4.5 and 3.5.3.

- Preliminary evaluation of the feasibility of the ChDR-based diagnostic system in the LHC, including discussion on the impact of the LHC beam halo on the emitted ChDR — subsections 3.5.1, 3.5.2 and 3.5.4.

- Designing and conducting an experiment for verification of the existing ChDR models at CERN's CLEAR facility, and analysing its results, in collaboration with C. Davut, S. Mazzoni, C. Pakuza, A. Schlögelhofer and E. Senes — subsections 3.6.1 to 3.6.4.

These activities were performed under the supervision of Dr Thibaut Lefèvre. The results included in this thesis were reported in three conference proceedings:

1. K. Lasocha et al., "Simulation of Cherenkov Diffraction Radiation for Various Radiator Designs", 9th International Beam Instrumentation Conference, Remote, Sep 2020,

2. K. Lasocha et al., "Feasibility Study of ChDR Diagnostic Device in the LHC", 12th International Particle Accelerator Conference, Remote, May 2021,

3. K. Lasocha et al., "Experimental Verification of Several Theoretical Models for ChDR Description", 13th International Particle Accelerator Conference, Bangkok, Jun 2022.

In addition, I had contributed to two other articles on the application of ChDR in beam diagnostics:

1. T. Lefèvre et al., "Cherenkov Diffraction Radiation as a Tool for Beam Diagnostics", 8th International Beam Instrumentation Conference, Malmo, Sep 2019,

2. D. Harryman et al., "Properties of Cherenkov Diffraction Radiation as Predicted by the Polarisation Currents Approach for Beam Instrumentation", 9th International Beam Instrumentation Conference, Remote, Sep 2020.

I have also given several seminars at CERN and UJ on this topic and two talks dedicated to a wider audience:

1. "Verification Experiment of Cherenkov Diffraction Radiation Theories at CLEAR Facility" at 42nd CLIC Project Meeting, CERN, May 2022,

2. "Experimental Verification of Several Theoretical Models for ChDR" at 13th International Particle Accelerator Conference, Bangkok, Jun 2022.

During my PhD studies at WFAIS UJ and CERN I also participated in other projects that were ultimately not included in this dissertation. I was a member of a team led by Prof. Elzbieta Richter-Was, which investigated how the substructure and pattern of hadronically decaying τ leptons can be useful in determining the CP state of the Higgs boson in the $H \to \tau\tau$ decay. I was responsible for maintaining the deep neural network used for the analysis and post-processing of the obtained results. Together with Dr Diogo Alves I have investigated the possibilities of bunch longitudinal phase-space reconstruction based on a Kalman filter. I have also authored one of the two algorithms used for the automatic detection of transverse beam instabilities in the LHC. These activities resulted in the following peer-reviewed articles:

1. T.E. Levens, K. Lasocha, T. Lefèvre, M. Gasior, R. Jones, T. Wlostowski, J.P. Ellis, R.J. Steinhagen, "Automatic detection of transverse beam instabilities in the Large Hadron Collider", Phys. Rev. Accel. Beams 22, 112803, Nov 2019.

2. K. Lasocha, E. Richter-Was, D. Tracz, Z. Was, P. Winkowska, "Machine learning classification: Case of Higgs boson CP state in $H \to \tau\tau$ decay at the LHC", Phys. Rev. D 100, 113001, Dec 2019,

3. K. Lasocha, E. Richter-Was, M. Sadowski, Z. Was, "Deep neural network application: Higgs boson CP state mixing angle in $H \to \tau\tau$ decay at the LHC", Phys. Rev. D 103, 036003, Feb 2021,

4. D. Alves, K. Lasocha, "Kalman filter-based longitudinal phase-space reconstruction method for hadron machines", Phys. Rev. Accel. Beams 24, 072801, Jul 2021.

For the last year of my PhD studies I have returned to Kraków and was fully stationed at Jagiellonian University. During this time, I got involved in activities of the Diagnostics and Electronics Section of the SOLARIS National Synchrotron Light Source. I was working on the diffraction radiation based bunch length monitoring system for the SOLARIS injector and POLFEL, the first Polish free electron laser. I also had the opportunity to become a member of the ATLAS Collaboration, where I followed studies on the precision measurements for the Run 2 luminosity and preparation for the Run 3 data taking.

TABLE OF CONTENTS

LIST OF FIGURES

ACKNOWLEDGMENTS

Throughout my PhD studies, I have been fortunate to work under the guidance of very valuable and helpful people. I would like to thank my university supervisor, Elżbieta Richter-Wąs, for believing in me and carefully overseeing my path of development in the field of physics. I am equally grateful to Diogo Alves, under whose direct care I spent 3 years at CERN, for countless discussions and his urge to fully understand every posed problem. Finally, I would like to thank Thibaut Lefèvre for his guidance, knowledge and support shown on many levels.

I deeply appreciate the good advice I have received from experts in the field of ChDR: P. Karataev and A. Potylitsyn. I am happy to have had the opportunity to work with and benefit from the experience of N. Mounet, S. Mazzoni and A. Curcio. I acknowledge the role of M. Wendt, who was the first to introduce me to Schottky noise analysis.

Working on my doctoral project would be much more difficult if it were not for my colleagues who, like me, were taking their first steps in the field of accelerator physics. I would especially like to mention A. Schlögelhofer, with whom I have always been able to discuss new ideas and who often supported me with his knowledge of experimental physics and English grammar. In addition, I appreciate the collaboration with other students involved in ChDR studies: E. Senes, C. Pakuza, C. Davut and D. Harryman. Special thanks go also to M. Wyszyński and B. Latacz.

It is impossible to ignore the role of other people in my development, with whom I shared my time at Beam Instrumentation Group. I would like to thank T. Levens for knowing the answer to every question. I am grateful to M. Krupa and M. Gąsior for their cordiality and constant willingness to help. I owe a lot to J. Spencer for being a wonderful officemate and friend. I would like to thank the members of the IQ and BP sections for all the cups of coffee we drank and the discussions that were held.

My gratitude is also due to the staff and professors of the Faculty of Physics, Astronomy and Applied Computer Science of the Jagiellonian University. Thanks to their goodwill, I was able to expand my knowledge and attend their courses remotely, even before the Covid pandemic forced everyone to do so. I would also like to thank the ZFGM Division for warmly welcoming me after my return to Krakow and for providing good conditions for work and development.

I would like to thank all entities for the financial support I received during my studies. I thank the CERN Doctoral Student Programme, the authorities of the Jagiellonian University and the Jagiellonian Interdisciplinary PhD Program. I acknowledge the support received from funds of Polish National Science Center under decisions DEC-2017/27/B/ST2/01391.

Finally, my love and endless gratitude are due to my relatives who have been waiting for my return from Geneva to Krakow for three years. To my parents who have been my first role models.

To my brothers and their families, who have been my dearest friends. And to my beloved wife Agnieszka, thanks to whom I always know that it's going to be fine.

CHAPTER 1
INTRODUCTION

1.1 Particle Accelerators

Since the second half of the 19th century *particle accelerators*, machines which propel charged particles to high velocities, while containing them in well-defined beam structures, have been essential to the progress of particle physics and have introduced numerous applications in industry and medicine.

In 1857, German physicist and glassblower Heinrich Geissler applied high voltage between two electrodes present at the ends of a glass tube which was partially evacuated of air. As a result, he observed that the tube was filled with a glow, an effect which was primarily used for entertainment and eventually evolved into commercial neon lighting. What Geissler did not know was that he had constructed one of the first particle accelerators, inside which free electrons and ions naturally present in air were attracted towards the inversely charged electrodes. Resulting collisions of charge carriers with gas atoms and the electrodes were causing this glow and increased the number of free electrons and ions, which acted in a similar manner amplifying the effect.

Geissler tubes were further improved by British physicist William Crookes, who has reduced the pressure inside the tube down to approximately 10^{-6} atm. As a consequence, free electrons knocked out of the cathode by positive ions could travel towards the anode with a very small probability of colliding with a gas atom. Continuously gaining energy over the whole distance, electrons were able to pass through the anode and glass wall behind it. Such an escape was indicated by a glow of the glass wall due to the energy released by electrons present in glass, returning to their original energy levels after being excited by a traversing electron. The so-called *cathode rays* were an object of studies conducted by J.J. Thomson. By applying a magnetic field behind the anode, he had observed that cathode rays are subject to a deflection, in just the way in which magnetic forces would act on a negatively charged body moving along the path of these rays. This experiment proved the existence of electrons and demonstrated an up-to-date technique of steering a particle beam with the help of a magnetic field.

Subsequent discoveries at the beginning of the 20th century shed more light on the composition of atoms, but also provoked new questions which required novel tools and approaches. In 1927, Ernest Rutherford, whose interpretation of the way alpha particles scatter on a thin metal foil led to the conclusion that an atom's positive charge and most of its mass is concentrated within a small nucleus, included the following words in his address to the Royal Society [1]:

"It has long been my ambition to have available for study a copious supply of atoms and

electrons which have an individual energy far transcending that of the alpha- and beta-particles from radioactive bodies. I am hopeful that I may yet have my wish fulfilled, but it is obvious that many experimental difficulties will have to be surmounted before this can be realised on a laboratory scale."

The initial response to Rutherford's call came in the form of electrostatic accelerators, with the two most notable examples being the *Van de Graaff generator* [2] and the *Cockcroft-Walton generator* [3]. The general principle of their operation is similar as in the case of Geissler or Crookes tubes. A charged particle is placed in a static potential between two electrodes and is accelerated while passing through the potential difference. A Van de Graaff generator uses a moving fabric belt to carry charge to the high voltage electrode. In the case of Cockcroft-Walton generators, a diode-capacitor voltage multiplier is used to produce a high voltage. Particles accelerated in such a way were used by Cockcroft and Walton to perform the first nuclear disintegration in history, which won them the Nobel Prize in 1951.

Regardless of their simplicity, electrostatic accelerators turned out to be not sufficient for increased expectations on the energy of accelerated particles, primarily due to the practical limits of the obtained voltages. Therefore, interest turned towards techniques involving dynamic fields. Such concepts had been proposed already in the 1930s, with *betatrons* [4] and *cyclotrons* [5] being important examples. In betatrons, particles are injected into a vacuum torus, where they are subject to acceleration due to the presence of an electric field. The field is generated via induction by the strengthening of the magnetic field within the torus, parallel to the torus axis. The circular trajectory is preserved as the perpendicular force arises from the magnetic field under *Widerøe's condition*:

$$\theta_0 = 2\pi r_0^2 H_0,$$

where θ_0 is the magnetic flux enclosed by the particle orbit, r_0 is the radius of the orbit and H_0 is the magnetic field density at the orbit. That means that the magnetic field at the particle's orbit must be equal to the half of the average field over its circular cross section. The main limitation to the maximal particle energy obtained inside a betatron is related to the limit of the strength of available magnetic fields and the physical size of the magnetic core.

An alternative concept that makes use of dynamic fields is the cyclotron. It relies on a static magnetic field, perpendicular to the flat cylindrical vacuum chamber, and a high-frequency alternating voltage applied between two hollow metal electrodes. The electrodes, called "dees" because of their "D"-like shape, are located at the opposite sides of the chamber. Charged particles, after being injected into the centre of the chamber, are alternatively attracted towards each of the electrodes,

while the static magnetic field ensures a circular trajectory. The frequency of the electric field is chosen in such a way that the particles make one turn during a single cycle of voltage. This is only possible when the frequency matches the cyclotron resonance frequency, given by:

$$f = \frac{qB}{2\pi m},$$

where B denotes the magnetic flux density and q, m are, respectively, the charge and relativistic mass of the charged particle. As the particle's velocity increases, so does the radius of the cylindrical trajectory, resulting in a spiral path outward from the centre of the chamber. The final energy is therefore limited by the strength of the magnetic field and the size of the chamber, but not only that. As the particles become relativistic, their mass increases, which changes the value of cyclotron resonance frequency and violates the working principle.

This issue was overcome with the invention of the *synchrotron* – another torus-shaped accelerator. The name comes from the fact that the magnetic field, responsible for bending the particle trajectory, is being increased with the increasing kinetic energy of the particle. In addition the acceleration and bending of the particle beam can be separated into a large number of stand-alone components, which enables the construction of a large-scale facility. Therefore, the limiting factor of the magnetic field strength could be relatively easily compensated for with increasing the size of the accelerator. The acceleration of particles is usually performed inside Radio-Frequency (RF) cavites, with a side-effect being that particle beams are divided into a series of distinct particle bunches. Within each bunch, the particles perform the so-called *synchrotron oscillations* in a longitudinal direction.

In parallel, the alternative concept of a linear accelerator was investigated, pioneered by the works of Ising and Wideroe [6, 7] from the end of the 1920s. According to Ising's proposal, particles were to travel through a series of chambers, witnessing only an accelerating polarity of an oscillating electric potential between each of them. Conceptually, this approach enables obtaining energies proportional to the length of the total structure. In addition, particles travelling in a straight line do not lose energy due to *synchrotron radiation*, which was a limiting factor to the maximal energy of electrons obtained in circular machines.

The evolution of the particle energy reached by accelerators through the 20th century is shown in Fig. 1.1. Up to date, the most powerful accelerators in terms of particle energy are synchrotrons, with notable examples being the Large Hadron Collider (LHC) at the CERN laboratory [8], the Schwerionensynchrotron (SIS18) at GSI Darmstadt [9], the Relativistic Heavy Ion Collider (RHIC) at Brookhaven National Laboratory [10] and phased out in 2011 the Tevatron at Fermilab [11].

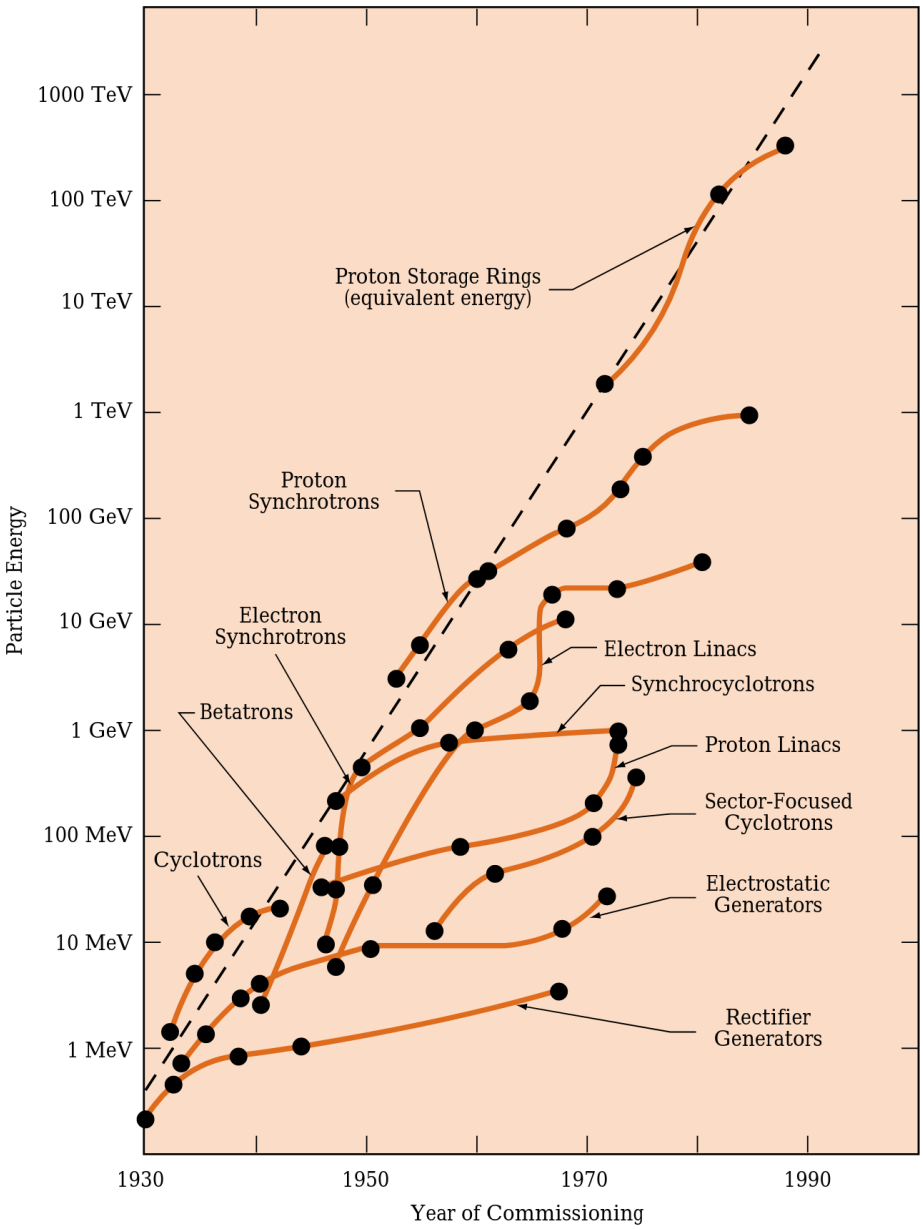

Figure 1.1: *Livingston plot* - evolution of the nominal beam energy in particle accelerators [12].

However, particle energy is not the only quantity relevant to physicists. Sometimes, high energy is the opposite of the actual goal. In particle decelerators, such as the Antiproton Decelerator [13] or ELENA [14] at CERN, antiparticles are slowed down to low energies to facilitate spectroscopy studies and other studies such as on antimatter gravitational interactions. This is done using RF systems in a similar manner as in synchrotrons, but with particles witnessing decelerating voltage, which leads to energy reduction. In addition, the energy spread is reduced by means of *electron* and

stochastic cooling [15, 16].

One of the most important beam parameters is the beam intensity, which in the case of relativistic particles is simply proportional to the overall number of particles in the beam. Intense hadron accelerators are used as a neutron or meson source through the collision of the beam with a fixed target. These include facilities such as the Swiss Spalation Neutron Source at the Paul Scherer Institute (SINQ), the ISIS neutron source, the Spalation Neutron Source at Oak Ridge National Laboratory (SNS ORNL) and European Spallation Source (ESS), currently under construction in Lund, Sweden. Parameters of the mentioned facilities are included in Table 1.1.

Table 1.1: Nominal parameters of certain present-day accelerators used for neutron and meson research

	Target	Beam Energy [MeV]	Beam Current [uA]	Pulse Rate [Hz]	Beam Power [kW]
SINQ [17]	Zr/Pb	570	2400	CW	1400
ISIS [18]	Ta, W, U	800	225	50	180
SNS [19]	Hg	1000	1600	60	1400
ESS [20]	W	2000	65000	14	5000

In particle colliders, complex accelerators designed in such a way that particle trajectories intersect, leading to particle collisions, the figure of merit is the luminosity, that is, the rate of interactions per second per unit cross section. More common and historically the first were electron-positron colliders, suitable for very precise investigations of electroweak and strong interactions. Notable examples of electron-positron colliders that operate today are SuperKEKB associated with the Belle II experiment [21] and BEPC II providing collisions to the Beijing Spectrometer III [22]. High energy hadron colliders have already been mentioned. The HERA electron-hadron collider [23] was operating between 1992 and 2007 at DESY, Hamburg. Currently, a new electron-ion collider is under construction at Brookhaven National Laboratory [24]. The parameters of selected particle colliders that are currently running are listed in Table 1.2.

The great cost and physical dimension of synchrotrons have prompted interest towards techniques which facilitate the creation of compact, even table-top accelerators. Various methods of obtaining a high accelerating gradient, that is, the energy gained by a particle per unit length, such

Table 1.2: Nominal parameters of certain present-day particle colliders

	Particles collided	Beam Energy [GeV per nucleon]	Beam Current [mA]	Peak Luminosity [$cm^{-2}s^{-1}$]
LHC [8, 25]	p^+ - p^+	p^+: 7000	582	10^{34}
	p^+ - Pb^{82+}	Pb^{82+}: 2759	58.2/6.12	$1.5 \cdot 10^{29}$
	Pb^{82+} - Pb^{82+}		6.12	10^{27}
RHIC [10]	p^+ - p^+	250.7	75	$9.5 \cdot 10^{30}$
	D - D	124.9	75	$9.5 \cdot 10^{30}$
	C^{6+} - C^{6+}	124.9	99	$4.6 \cdot 10^{29}$
	S^{16+} - S^{16+}	124.9	77	$3.9 \cdot 10^{28}$
	Cu^{29+} - Cu^{29+}	114.9	98	$1.8 \cdot 10^{28}$
	I^{53+} - I^{53+}	104.1	103	$5.4 \cdot 10^{27}$
	Au^{79+} - Au^{79+}	100.0	65	$9.2 \cdot 10^{26}$
SuperKEKB [26]	e^+ - e^-	4/7	3600/2600	$8 \cdot 10^{35}$
BEPC II [27]	e^+ - e^-	1.89	980	10^{33}

as *Plasma Wakefield Acceleration* [28], *Dielectric Wakefield Acceleration* [29] and *Dielectric Laser Acceleration* [30] are carefully studied. Pioneering achievements in this field include the proof-of-principle plasma wakefield accelerator experiment AWAKE at CERN and the demonstration of electron acceleration in a laser-driven dielectric microstructure at the SLAC National Accelerator Laboratory [31]

The emission of synchrotron radiation, spurious when the goal is to preserve a highly energetic lepton beam, is actually enhanced and well controlled in synchrotron light sources by using special insertion devices such as undulators and wigglers. Intense and well-collimated radiation can then be used for many types of research in materials science, chemistry, medicine and history of art. Among numerous *third* and *fourth generation* synchrotron light sources, that is, synchrotrons equipped with insertion devices, one may include the Extreme Brilliant Source at European Synchrotron Radiation Facility in Grenoble (ESFR-EBS), Diamond Light Source at Rutherford Appleton Laboratory and SOLARIS in Kraków. The figure of merit for light sources is the *brightness* of the synchrotron radiation, closely related to the value of transverse *emittance*, which combines the size and transverse momentum spread. The relevant parameters of the selected synchrotron light sources currently in operation are presented in Table 1.3.

Table 1.3: Nominal parameters of certain present-day synchrotron light sources

	Research Beamlines*	Beam Energy [GeV]	Beam Current [uA]	Horizontal emittance [nm rad]
ESRF-EBS [32]	44	6	200	0.13
PETRA III [33]	24	6	100	1.2
Diamond [34]	8	3	300	2.7
KEK PF [35]	22	2.5	300-450	36
PSI SLS [36]	16	2.4	400	9
Solaris [37]	6	1.5	500	6

*As for March 2022

1.2 Beam Characteristics

The beam of particles travelling along the accelerator can be described by a suite of parameters. Among them, one can include:

- **Beam momentum** and **energy** - one of the most fundamental characteristics of the beam which have a substantial impact on how accelerated particles interact with each other or with external elements, e.g. during collisions. As beam momentum, one refers to the average longitudinal momentum p_z of the particles. The beam energy refers to the average value of $E = \sqrt{p_z^2c^2 + m^2c^4}$. For highly relativistic beams one has $p_z c \approx E$ and both quantities are used interchangeably. In the context of accelerator physics, the energy determines the particle velocity and beam rigidity, a quantity that expresses how hard it is to bend the beam using a magnetic field as a function of the charge of the species and radius of the machine. As a result, in the case of synchrotrons, the beam energy implicitly determines the revolution period T_{rev} or T_0, the elapsed time for a particle to make a full turn around the machine on the energy-dependent trajectory. At low energies, the revolution frequency grows with the increase of the beam energy, as also the particle velocity increases. At some point, the particles become relativistic and approach the velocity of light. If not compensated by an increase in

magnet strength, the revolution frequency is reduced as a result of the increasing radius of the beam trajectory. The energy at which the revolution frequency reaches its maximum is called *transition energy*. Due to operational challenges linked to the transition, many accelerators are designed in such a way that injected particles are already above the transition energy.

- **Beam momentum spread** - within the beam, individual particles are not identical and each of them has slightly different characteristics. As the measurement of the momentum of each individual particle is technically not feasible, the momentum spread indicates how precisely physical phenomena can be studied using a given beam. Beam cooling techniques can be used to reduce the spread of momentum and equalise the characteristics of the particles.

  For individual particles, the momentum deviation Δp is closely related to the deviation of the revolution frequency Δf_{rev} as has been explained while discussing the beam energy. The slip factor η is defined as the ratio between the relative momentum deviation and the revolution frequency deviation:

  $$\frac{\Delta f_{rev}}{f_{rev}} = \eta \frac{\Delta p}{p}.$$

  The slip factor is positive if the beam energy is below transition and negative if it is above. Due to its linearity, the equation above also holds for the normalised standard deviation of the momentum and revolution frequency, if the slip factor is replaced with its absolute value.

- **Beam intensity, charge** and **current** - quantities that describe the number of charged particles present in a specified region of interest. The choice of the region of interest depends on the accelerator type. For linear machines, it is usually a single bunch or a train of bunches. In the case of circular machines, such as a synchrotron, the intensity might refer to a single bunch or to the total number of charges circulating in the machine.

  The beam intensity is directly connected with the rate at which desired physical processes are happening, or to the amount of radiation produced by the accelerated beam. On the other hand, the high intensity of the beam might become a technical challenge and lead to beam instability.

- **Beam position** - as *beam position* one usually refers to the average transverse, i.e. horizontal and vertical, location of the particles while passing through a given cross section of the accelerator structure. Determining the average position of the beam along the machine makes it possible to reconstruct the so-called *beam orbit*. Observation of the beam orbit is indispensable for troubleshooting and optimisation of the accelerating structure. In addition,

precise knowledge of the beam orbit near the interaction region is necessary for calculation of the luminosity.

- **Transverse profile** and **emittance** - in analogy with the momentum, the positions of individual particles differ from the mean transverse beam position. The *transverse profile* is the overall distribution of the positions of particles projected on a cross section of the accelerator structure. In many contexts, especially when the shape is close to a Gaussian, the transverse profile can be parameterized by two width values, namely vertical and horizontal standard deviation.

  The shape of the transverse profile is not constant along the accelerator. In modern synchrotrons the beam is sequentially focused and defocused by quadrupole magnets. This changes the transverse profile, but also the transverse momentum, usually called the *angle*, responsible for the transformation of the transverse profile. If one depicts the beam in either vertical or horizontal momentum-position phase space, the area occupied by the beam defines the so-called *emittance* [38, Chapter 3.2.4]. If the beam is subject only to conservative forces, the emittance is conserved by the virtue of Liouville's theorem [39].

- **Betatron tune and chromaticity** - the transverse particle oscillations induced by quadrupole magnets is called *betatron motion* [40]. Equivalently to the betatron frequency, one usually describes the rate defined by the number of transverse oscillations during one revolution period as the *betatron tune*. Control of the betatron tune is crucial for the stability of the beam and in general we have that the values of the vertical and horizontal tune Q_H, Q_V have to be such as to avoid the resonance condition

$$aQ_H + bQ_V = c,$$

  where a, b, c are integers. The *resonance order* is defined as the sum $|a| + |b|$. Due to magnetic imperfections the low order resonances lead to rapidly growing instabilities.

  The quadrupole focusing strength is different for particles with different momenta. The spread in beam momentum will therefore result in a tune spread. In the first order approximation, one has

$$\Delta Q = Q\xi\frac{\Delta p}{p},$$

  where $Q\xi$ is called *chromaticity*. The value of chromaticity can be adjusted with the use of sextupole correction magnets.

- **Longitudinal profile** - in machines which use RF systems for acceleration, individual particles will witness different RF voltages on every turn, depending on their relative longitudinal position with respect to the RF waveform. This leads to the so-called synchrotron motion, an oscillation of the particle revolution frequency and energy. Particle, in the form of *bunches*, oscillate around a reference, the so-called *synchronous particle*, for which the energy and revolution frequency is constant on every turn [41, Chapter 5.1.3]. Taking the synchronous particle as a reference, one can define the *synchrotron frequency* and *synchrotron amplitude* which, along with the initial sychrotron phase, fully parameterize these oscillations. The overall *longitudinal bunch profile* is the instantaneous distribution of the particles with respect to the synchronous particle.

  The longitudinal profile of the bunch is naturally connected to the momentum deviation. The area occupied by the beam in a longitudinal position-momentum phase space defines the so-called *longitudinal emittance* [38, Chapter 2.2.2].

1.3 Beam Diagnostics

The operation of any particle accelerator would not be possible without instrumentation designed to measure the properties of the beam. The overwhelming majority of diagnostic techniques is based on estimating beam properties from the electromagnetic field of particles. However, the measurement varies depending on the property which is to be measured and the type of the particle beam.

For the measurement of beam intensity and position, the concept of direct coupling to the electromagnetic field carried by the moving particles is widely applied. Depending on the design, the travelling particle may, for instance, induce image charges on an insulated metallic plate, which results in an alternating current signal seen on the plate. This is the case for LHC beam position monitors [42]. Alternatively, the particles pass through an inductive loop inducing a voltage via the beam's time-varying magnetic fields. This is the case for the LHC Fast Beam Current Transformer [43], used for bunch-by-bunch intensity measurements. Furthermore, one can extend the field outside the beam chamber by interrupting the conducting path in the chamber. This approach gives more freedom to the instrument designer, as the limitations imposed by the vacuum environment may be dropped, and a more refined apparatus can be used. LHC instruments that work on this principle include the Wall Current Monitor, which provides the length and longitudinal profile of the bunch [44]. Another technique, particularly interesting from the perspective of this thesis, is based on the coupling of the beam's electromagnetic field to a slotted waveguide, as is done in the LHC Schottky Monitor [45].

An alternative measurement principle is to couple to the electromagnetic field emitted by moving particles in the form of radiation. Although a charge moving with a uniform velocity through vacuum does not radiate, radiation arises naturally in many contexts within the field of accelerator physics. The previously mentioned synchrotron radiation is emitted due to the curvature of the beam trajectory, as inside the bending elements the particles are subject to an acceleration perpendicular to their velocity. Cherenkov radiation is a phenomenon observed when a charged particle travels through a medium with a phase velocity greater than the phase velocity of light in this medium. This effect, widely used for particle detection [46–48], has also been applied in beam loss monitoring systems [49]. Transition radiation occurs when a particle passes through the boundary between two different media. Such a situation can be provoked, for example, by introducing a thin intercepting foil on the beam path, a technique commonly used in beam emittance and profile diagnostics [50–52]. A similar type of radiation, Diffraction Radiation, is produced when a charged particle's field meets a discontinuity in the surrounding medium structure, such as, for example, when a particle enters a slit between two half-planes. The radiation emitted can be studied and provides information on the size or position of the beam [53, 54]. If the surrounding discontinuity takes the form of a thin grating of finite permittivity, the Smith-Purcell radiation arises, which can be applied to obtain longitudinal and transverse beam profiles [55]. Recently, the concept of Cherenkov Diffraction Radiation (ChDR) has been intensively studied in the context of beam diagnostics [56]. This type of radiation is emitted within the medium when a charged particle passes in close vicinity, with a velocity exceeding the phase velocity of light in this medium. The only difference with the well-known phenomenon of Cherenkov Radiation is the fact that the particle of interest travels outside instead of inside of the medium. For that reason, in older publications the term *Cherenkov Radiation* covers also this type of radiation.

Except for Cherenkov radiation and transition radiation, the so-far mentioned techniques of beam diagnostics have the advantage of being non-interfering with the beam itself. This is not the case for all diagnostic instruments, however a noninvasive method is not always required. For example, during the commissioning of a new accelerator, one can accept a measurement that is even completely destructive for the beam, if only it is a robust and reliable way of obtaining the desired beam characteristics. Moreover, in linear machines, since each bunch is observed only once, some number of initial bunches might be sacrificed to learn the properties of the following ones. Finally, in certain situations, the measurement is only slightly affecting the beam, up to the level which is acceptable for further operation.

Among the standard invasive diagnostic devices, one can include the Wire Scanner, an instrument used in the LHC and its injector chain for the measurement of the transverse beam profile [57].

Its operating principle is to move a thin wire through the passing beam. The interaction between the wire and the beam would result in the generation of secondary particles. These can be detected by a dedicated sensor with the amount being proportional to the beam intensity at the current position of the wire. The operational limit of such devices in high-energy accelerators is connected to the breakage of the wire due to beam heating and makes them suitable mostly for cross-calibration of other devices [58]. The intensity of secondary particle showers, this time created in unwanted collisions between particles and elements of the accelerator structure, is also measured to assess the number of particles unintentionally lost at a given location. The LHC beam loss monitoring system, crucial for beam operation safety, consists of about four thousand Beam Loss Monitors [59].

Another possibility is to measure the properties of the beam in a noninvasive way but only after affecting the beam in such a way that certain characteristics are highly exposed. As an example of such an approach, one may take the estimation of the *betatron tune*, the number of transverse beam oscillations per one longitudinal revolution, based on the measurement of the beam position after a transverse beam kick. Enhanced beam oscillations can be observed in the Discrete Fourier Transform of the beam position signal at a frequency corresponding to the tune value [40]. A similar technique is used to derive *chromaticity*, that is, the logarithmic derivative of the betatron tune with respect to the momentum deviation. An RF system-induced momentum modulation modifies the value of the betatron tune, and the chromaticity is determined based on the measured magnitude of the change [60].

1.4 Scope of the Thesis

The purpose of the work presented in this dissertation was to improve two existing beam diagnostic techniques. The thesis is divided into two parts that consider different approaches.

The first part is dedicated to the so-called *Schottky signals*, which are manifested in the beam intensity signal as fluctuations and can be analyzed after conversion to the frequency domain. The analysis of Schottky signals is a fundamental technique for deriving the properties of unbunched hadron beams, but the task is far more challenging in the case of beams accelerated with RF systems, i.e. having bunch structure [61], which leads to less accurate estimates [62]. Nevertheless, the LHC Schottky Monitor is the only instrument capable of measuring the LHC beam chromaticity in a noninvasive manner. For this reason, improvements in Schottky signal analysis techniques were required. The discussion on the analysis of Schottky signals begins with a brief introduction. The Schottky signal theory is then presented and discussed. This includes a formal derivation of the relation between the width of a Schottky spectrum and the value of beam chromaticity,

which has so far been missing in the literature. In the following section, two new methods of Schottky signal analysis are proposed. One of them is dedicated exclusively to the tune estimation, while the other brings possibilities for deriving various beam parameters, with the ultimate goal of deriving the chromaticity. After applying them to data collected by LHC Schottky Monitor, their performance is compared with results from alternative measurement methods. Discussion of Schottky signal analysis is concluded with a proposal on how to reduce the magnitude of spurious coherent components of the Schottky signal. The results presented in this part of the thesis have been published in Refs. [63, 64].

The second part of this dissertation discusses the application of Cherenkov diffraction radiation in beam diagnostics. The concept is relatively new and still requires extensive studies from both theoretical and practical points of view. Techniques of estimation of ChDR properties had been either computationally challenging or were limited to very simple geometries. In particular, a method for estimation of ChDR yield in the case of multilayered radiators was desired. In the course of the studies it was also revealed, that different theoretical results are not compatible with each other. The discussion starts with introduction to the topic. Then follows a presentation of used so far theoretical models of ChDR emission in simple geometries. In the next Section, systematic study of how relevant beam parameters are expressed in the properties of emitted radiation is presented. Then a new semi-analytical framework for ChDR studies is discussed. It allows for calculation of the expected radiation yield in the case of more complex multilayered radiators and fills the gap between simplified theoretical models and computer simulations. The new framework is used for studies on the impact of thin coatings deposited on the radiator surface, either for signal enhancement or to mitigate undesired effects, such as the creation of electron clouds. In the following, the feasibility of using ChDR-based diagnostic devices in the Large Hadron Collider is discussed. The second part is concluded with the results of the dedicated experiment performed in 2021 on the CLEAR accelerator at CERN, the aim of which was to understand the range of validity of currently used theoretical models. The results on ChDR presented here have been reported in Refs. [65–67].

CHAPTER 2
THE ANALYSIS OF SCHOTTKY SIGNAL

2.1 Introduction

The history of Schottky signal analysis dates to the work of Simon van der Meer at the Intersection Storage Ring at CERN in 1971, where it was used to evaluate the performance of the newly invented concept of stochastic cooling [68]. Since then it has served as a tool for betatron tune, emittance and chromaticity measurements at numerous accelerator facilities, including, among others, the Relativistic Heavy Ion Collider at Brookhaven National Laboratory [69]; Tevatron and Recycler at Fermilab [70] and the heavy-ion synchrotron SIS-18 at GSI Helmholtzzentrum für Schwerionenforschung [71]. At the CERN accelerator complex, Schottky diagnostics have successfully helped in the operation of Super Proton Synchrotron [72]; Antiproton Collector, Accumulator and Decelerator [73, 74]; Extra Low ENergy Antiproton ring [75] and Large Hadron Collider (LHC) [45].

The principle of the Schottky signal analysis lies in the observation that although macroscopically the particle beam intensity seems to be a smooth and stationary function of time, in fact it is subject to intrinsic fluctuations, originating from a finite number of particles having different characteristics. In the case of a bunched beam, the Schottky signal (also called Schottky noise) might be seen as a difference between the ideal stationary bunch intensity and the actual beam intensity, as presented in Fig. 2.1. It is important to note that effects of acquisition system imperfections are not included here. All the fluctuations in Fig. 2.1 come from the discrete character of the particle bunch; therefore, they are a true signal, and the word *noise* is used only to underline the instantaneous deviation from the nominal bunch profile. The shape of such noise is influenced by a wide range of beam parameters. It reflects, among others, the revolution and synchrotron frequencies, synchrotron amplitude distribution, betatron tune and transverse emittance. To retrieve these characteristics, it is convenient to look at the Schottky signal not in time but rather in the frequency domain.

The considerations begin with the case of only one bunch circulating in the accelerator. For an intensity measurement, it corresponds to a series of intensity pulses, equidistantly distributed over time with a period $T_{rev} = \frac{2\pi}{\omega_0}$. Such a signal can be represented by a *Dirac comb* function, defined as

$$\text{Ш}_{T_{rev}}(t) \ := \sum_{k=-\infty}^{\infty} \delta(t - kT_{rev}).$$

If one assumes a Gaussian bunch profile without any intra-bunch motion, the Fourier transform of the intensity signal consists of a series of infinitely short pulses of amplitude bounded by the Gaussian envelope, as presented in Fig. 2.2. This follows from the convolution theorem [76] and the

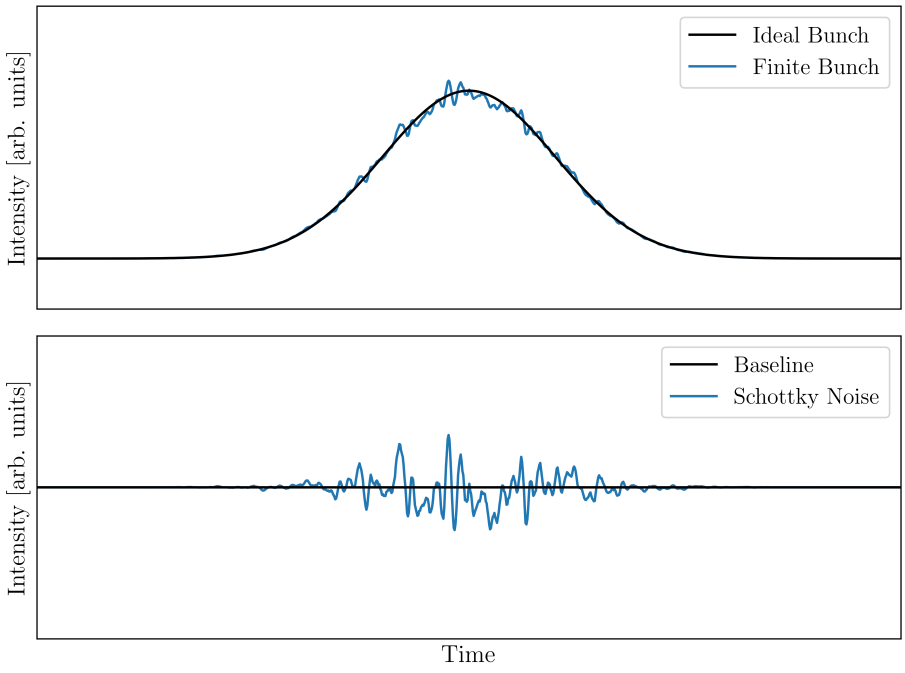

Figure 2.1: Comparison of an ideal continuous bunch profile with the realistic case of a finite ensemble of particles.

fact that the Fourier transform of a Dirac comb and a Gaussian is, respectively, a Dirac comb and a Gaussian.

The picture becomes more complicated after the introduction of intra-bunch motion, that is, when one actually considers the Schottky noise in the signal. In this situation, visualised in Fig. 2.3, the turn-by-turn bunch signal fluctuates due to the finite number of particles. This fact is reflected in the frequency domain; each pulse at the harmonic of the revolution frequency is surrounded by a series of satellites having relatively low magnitude. These satellites form the Schottky noise in the frequency domain, often called *Schottky spectrum*. Its structure is well suited for diagnostic purposes. In the following sections, it shall be precisely described how the beam characteristics affect the Schottky spectrum and how its properties can be retrieved from the analysis of the spectrum.

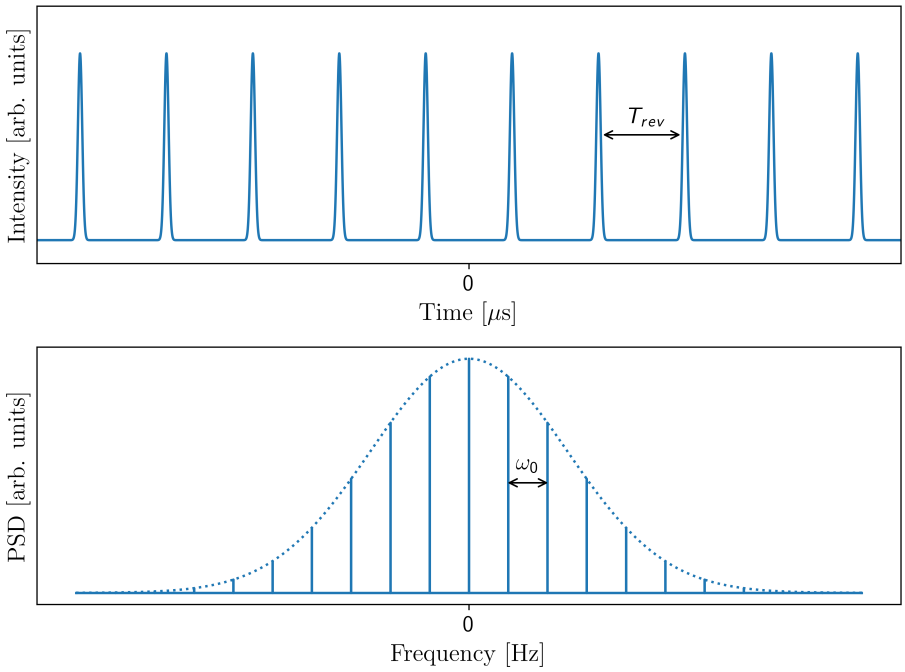

Figure 2.2: Time and frequency domain representation of a single ideal bunch intensity, without intra-bunch motion.

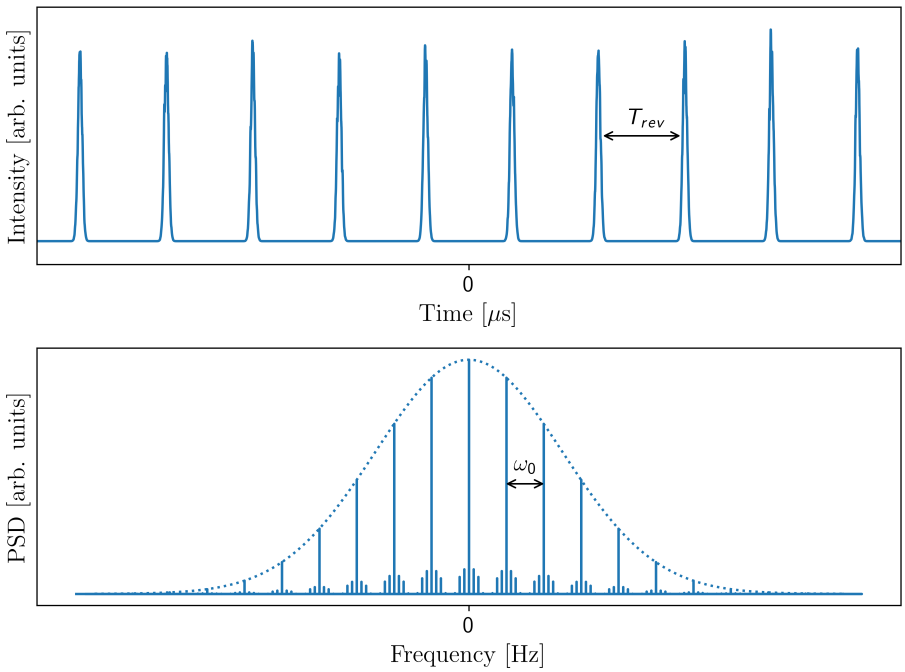

Figure 2.3: Time and frequency domain representation of a single realistic bunch intensity, including intra-bunch motion.

2.2 The Bunched Beam Schottky Signal Spectra

Two different types of Schottky spectra of a bunched beam can be distinguished, that is, the longitudinal and transverse Schottky spectra. The first one can be obtained as a Fourier transform of the beam intensity signal, while the latter originates from the beam dipole moment. The dipole moment can be measured as a difference in signal from two opposite intensity pickups. However, in reality, it is extremely difficult to fully reject the common mode from the signal difference. For that reason, longitudinal and transverse signals are commonly observed together. Separation between longitudinal and transverse components is, however, justified because the frequency regions of both types of signal are often well separated. It also allows to improve clarity and brevity of the description.

The theory presented in this subsection is limited to the case of only one bunch circulating along the machine. The presence of multiple bunches can complicate the picture to the point where the observed intensity or dipole moment signals can come simultaneously from distinct sources, potentially unevenly distributed along the machine. Such complex forms of the resulting spectrum can be, however, mitigated with the use of bunch gating systems, masking all bunches apart from one. The description of the form of the multi-bunch spectrum is given in Section 2.5.

The derivations presented herein do not consider any form of particle energy loss, for example, due to synchrotron radiation. In the case of hadron machines, this is a justified approach, as the energy loss is negligible when compared to the beam momentum. It, however, does not hold for lighter particles. In fact, for that reason, a diagnostic system based on Schottky signal analysis does not seem suitable for electron or positron accelerators. The impact of high-order correction magnets, such as octupole magnets, and the beam impedance on the Schottky spectrum is also not included in the derivations presented herein.

2.2.1 Longitudinal Spectrum

The derivation of the longitudinal Schottky spectrum should start from considering the case of a beam consisting of a single particle i. One denotes the intensity signal, taken as a function of time t, as $I_i(t)$. For a particle of charge q, circulating in a ring with constant revolution frequency ω_0, one obtains the following relation

$$I_i(t) = \omega_0 q \sum_{n=-\infty}^{\infty} \delta[\omega_0 t - 2\pi n] = \frac{\omega_0 q}{2\pi} \sum_{n=-\infty}^{\infty} e^{jn\omega_0 t}. \tag{2.1}$$

This means that, in frequency domain, the intensity signal consists of a series of delta pulses, located at harmonics of the revolution frequency.

In addition to the revolution motion, the particles perform synchrotron oscillations, which are the result of the RF acceleration and momentum spread. The time difference between a particle i and the reference synchronous particle, which does not perform any synchrotron oscillation, can be approximated by a simple harmonic motion [77]:

$$\tau_i(t) = \widehat{\tau}_i \sin\left(\Omega_{s_i} t + \varphi_{s_i}\right), \tag{2.2}$$

where $\widehat{\tau}_i$ is the temporal oscillation amplitude, φ_{s_i} is the initial phase and Ω_{s_i} is the synchrotron frequency. The value of synchrotron frequency is amplitude-dependent and follows from the theory of the mathematical pendulum:

$$\Omega_{s_i} = \frac{\pi}{2\mathcal{K}\left[\sin\left(\dfrac{h\omega_0\widehat{\tau}_i}{2}\right)\right]}\Omega_{s_0}, \tag{2.3}$$

where $h\omega_0\widehat{\tau} = \widehat{\Delta\phi_{RF}}$ is the RF phase amplitude of synchrotron oscillations, $\mathcal{K}\left([0,1]\right) \rightarrow [\pi/2, \infty]$ is the complete elliptic integral of the first kind [78, p. 590], and Ω_{s_0} denotes the nominal synchrotron frequency.

One can now revise Eq. (2.1) and write

$$I_i(t) = \omega_0 q \sum_{n=-\infty}^{\infty} \delta[\omega_0(t + \tau_i(t)) - 2\pi n] = \frac{\omega_0 q}{2\pi} \sum_{n=-\infty}^{\infty} e^{jn\omega_0(t+\widehat{\tau}_i \sin\left(\Omega_{s_i} t + \varphi_{s_i}\right))}. \tag{2.4}$$

By virtue of the Jacobi-Anger expansion [78, p. 361]:

$$e^{jz\sin\theta} = \sum_{p=-\infty}^{\infty} J_p(z)\, e^{jp\theta},$$

where $J_p(\cdot)$ denotes the Bessel function of the first kind and order p, Eq. (2.4) takes finally the following form:

$$I_i(t) = \frac{\omega_0 q}{2\pi} \sum_{n=-\infty}^{\infty} \sum_{p=-\infty}^{\infty} J_p\left(n\omega_0\widehat{\tau}_i\right) e^{j\left(n\omega_0 t + p\Omega_{s_i} t + p\varphi_{s_i}\right)}. \tag{2.5}$$

In most cases, one is interested only in a small spectral interval, centred around a certain harmonic n of the revolution frequency. For example, the LHC Schottky monitor operates at the

$n = 427725$ harmonic (approximately 4.8 GHz). One writes then

$$I_i(t) \propto \Re\left(\sum_{p=-\infty}^{\infty} J_p\left(n\omega_0\widehat{\tau}_i\right) e^{j\left(n\omega_0 t + p\Omega_{s_i} t + p\varphi_{s_i}\right)}\right), \tag{2.6}$$

where $\Re(\cdot)$ denotes the real part of a complex number. As illustrated in Fig. 2.4 for typical LHC parameters, a single particle spectrum around a certain harmonic n of the revolution frequency consists of a series of satellites located at integer multiples of the synchrotron frequency Ω_{s_i}, whose respective magnitudes are given by the Bessel function of the respective order.

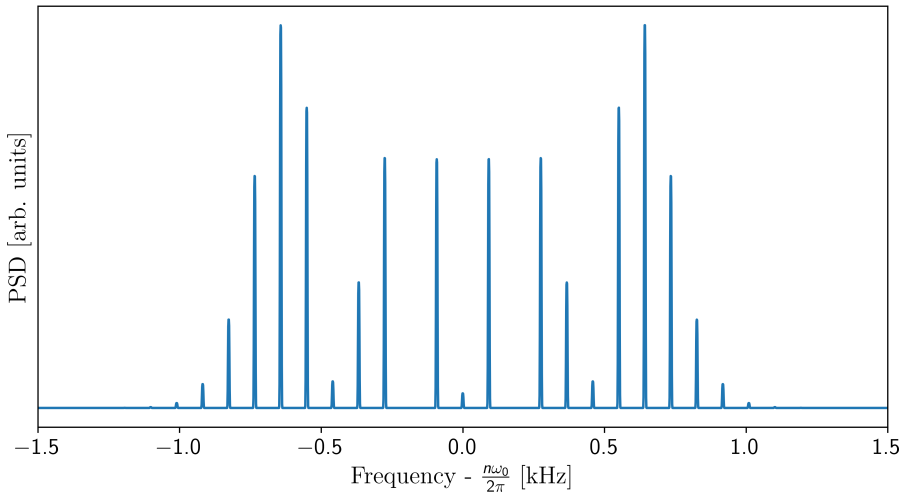

Figure 2.4: Single-particle longitudinal Schottky spectrum.

If one has many particles with different synchrotron amplitudes, the Schottky spectrum has to reflect their interference. One can express the total signal intensity as

$$I(t) = \sum_{i=1}^{N} I_i(t) \propto \Re\left(\sum_{i=1}^{N}\sum_{p=-\infty}^{\infty} J_p\left(n\omega_0\widehat{\tau}_i\right) e^{j\left(n\omega_0 t + p\Omega_{s_i} t + p\varphi_{s_i}\right)}\right). \tag{2.7}$$

Depending on the value of $n\omega_0\widehat{\tau}_i$, each particle contributes in its own way and in different frequency ranges, as the value of $J_p^2(n\omega_0\widehat{\tau}_i)$ converges monotonically to zero with p for $p > n\omega_0\widehat{\tau}_i$. Different values of Ω_{s_i} result in a broadening and, for high indices of p, even overlapping of the Bessel satellites.

Let us now assume that the synchrotron phases φ_{s_i} are independently and uniformly distributed among the particles. This assumption means that the bunch is not subject to any intra-bunch coherent motion. Due to the $p\varphi_{s_i}$ phase term in Eq. (2.7), which vanishes for $p = 0$, contributions to the central satellite add up coherently, thus making its power density proportional to the square of

the number of particles. For all other satellites, the instantaneous power density is non-deterministic, since it depends on the random synchrotron phases of all particles, and is proportional to the number of particles in the bunch. This statement can be proven by applying the Wiener-Khinchin theorem [79]. Let's consider the Power Spectral Density (PSD), $P(\omega)$, where $\omega \neq n\omega_0$, of the intensity signal $I(t) = \sum_i^N I_i(t)$. As $I(t)$ is a wide-sense stationary process, the Wiener-Khinchin theorem gives us

$$P(\omega) = \int_{-\infty}^{\infty} c(\tau)\, e^{-j\omega\tau} d\tau,$$

where $c(\tau) = \langle I(t) I^*(t-\tau) \rangle$ is the autocorrelation function of $I(t)$, $\langle \cdot \rangle$ denotes ensemble averaging and I^* denotes the complex conjugate of I. The previous equation can also be written in the following form:

$$\begin{aligned} P(\omega) &= \int_{-\infty}^{\infty} \left\langle \left[\sum_{i=1}^{N} I_i(t) \right] \times \left[\sum_{i=1}^{N} I_i^*(t-\tau) \right] \right\rangle e^{-j\omega\tau} d\tau = \\ &= \int_{-\infty}^{\infty} \left\langle \sum_{i=1}^{N} \sum_{\substack{j=1 \\ j\neq i}}^{N} I_i(t) I_j^*(t-\tau) + \sum_{i=1}^{N} I_i(t) I_i^*(t-\tau) \right\rangle e^{-j\omega\tau} d\tau. \end{aligned} \tag{2.8}$$

As $I(t)$ is a wide-sense stationary process, one does not need to specify time t. Since the synchrotron phases are uniformly and independently distributed, the first sum term of the expected value vanishes. In the second one, the synchrotron phases cancel out, so one can write:

$$\begin{aligned} P(\omega) &= \int_{-\infty}^{\infty} \sum_{i=1}^{N} I_i(t) I_i^*(t-\tau) e^{-j\omega\tau} d\tau = \\ &= \int_{-\infty}^{\infty} \sum_{i=1}^{N} \sum_{p=-\infty}^{\infty} J_p^2(n\omega_0 \widehat{\tau}_i)\, e^{j\left(n\omega_0\tau + p\Omega_{s_i}\tau\right)} e^{-j\omega\tau} d\tau = \\ &= \sum_{i=1}^{N} \sum_{p=-\infty}^{\infty} J_p^2(n\omega_0 \widehat{\tau}_i)\, \delta(\omega - n\omega_0 - p\Omega_{s_i}). \end{aligned}$$

If one denotes the PSD of $I_i(t)$ as $P_i(\omega)$, the above equation can be written as

$$P(\omega) = \sum_{i=1}^{N} P_i(\omega), \tag{2.9}$$

so the PSD is just the sum of single-particle contributions. The same is not true for $\omega = n\omega_0$. At such frequencies, the only nonzero contribution comes from $p = 0$ terms, so the synchrotron phase term is absent. For that reason, the first sum term in Eq. (2.8) does not vanish, and the PSD is

proportional to the number of particles squared. As a result, the central satellite dominates the spectrum, as shown in Fig. 2.5.

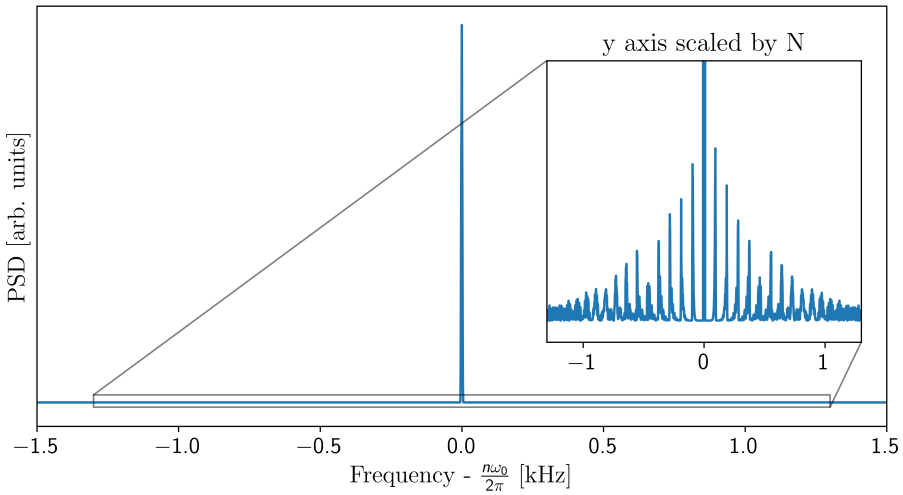

Figure 2.5: Longitudinal Schottky spectrum for bunched beam.

From Eq. (2.7) one can deduce that differences in the individual particle spectra are only due to the particle's synchrotron amplitude. Although the synchrotron frequency also seems to contribute, it is given by Eq. (2.3) as a function of the synchrotron amplitude. Finally, the synchrotron phase does not influence the single-particle PSD. One may conclude that the longitudinal Schottky spectra are explicitly dependent on the distribution of synchrotron amplitudes.

Assuming that one knows the distribution $g(\widehat{\tau})$ of synchrotron amplitudes among the particles, one may express $P(\omega)$, the power at a given frequency, as:

$$P(\omega) = \int_0^\infty g(\widehat{\tau}) P(\omega, \widehat{\tau}) d\widehat{\tau}, \tag{2.10}$$

where $P(\omega, \widehat{\tau})$ is the PSD at frequency ω of a particle with synchrotron amplitude $\widehat{\tau}$. Equation (2.10) can be seen as the continuous analogue of Eq. (2.9).

2.2.2 Transverse Spectrum

Contrary to the longitudinal Schottky spectrum, the transverse spectrum is obtained from the Fourier transform of a dipole moment signal, rather than from the intensity. The dipole moment signal due to a single-particle i is given in the following form:

$$D^i(t) \propto I_i(t) \cdot x_i(t),$$

where $I_i(t)$ is the intensity signal and $x_i(t)$ is the transverse displacement. It was previously demonstrated in Eq. (2.4) that

$$I_i(t) \propto \sum_{n=-\infty}^{\infty} e^{jn\omega_0(t+\widehat{\tau}_i \sin\left(\Omega_{s_i} t+\varphi_{s_i}\right))},$$

where ω_0 is the revolution frequency and $\widehat{\tau}_i, \Omega_{s_i}, \varphi_{s_i}$ are, respectively, the amplitude, the frequency, and the initial phase of a synchrotron motion. For the betatron amplitude $\widehat{x_i}$ the transverse displacement is given by

$$x_i(t) = \widehat{x_i} \cos\left[\phi_{\beta_i}(t)\right],$$

where ϕ_{β_i} is the phase of the betatron oscillations.

The betatron frequency of particle i is given by the product of betatron tune $Q_i(t)$ and the nominal revolution frequency ω_0[1]:

$$\omega_{\beta_i}(t) = Q_i(t)\,\omega_0$$

which, as a consequence of the synchrotron motion, is equal to:

$$\omega_{\beta_i}(t) = \left[Q + \widehat{Q_i} \cos\left(\Omega_{s_i} t + \varphi_{s_i}\right)\right] \omega_0, \tag{2.11}$$

where Q is the nominal tune and $\widehat{Q_i}$ is the amplitude of the tune oscillations. The convention adopted here is such that the amplitude of synchrotron motion $\widehat{\tau}_i$ is positive, whereas the amplitude of momentum oscillations $\widehat{p}_i$ and the amplitude of betatron tune oscillations $\widehat{Q_i}$ may be of any sign, depending on signs of the slip factor η and chromaticity $Q\xi$. The indefinite integral of Eq. (2.11) with respect to time gives the phase of the betatron motion:

$$\phi_{\beta_i}(t) = Q\omega_0 t + \frac{\widehat{Q_i}\omega_0}{\Omega_{s_i}} \sin\left(\Omega_{s_i} t + \varphi_{s_i}\right) + \varphi_{\beta_i}, \tag{2.12}$$

1. It is important to underline here that in the scope of this thesis the betatron tune is defined as the ratio between the betatron frequency $\omega_{\beta_i}(t)$ and the nominal revolution frequency ω_0, not the instantaneous revolution frequency $\omega_i(t)$. The alternative definition, common in the literature, results in a slightly different definition of chromaticity and expressions for transverse Schottky signals.

where φ_{β_i} is the initial phase of the betatron oscillation. Finally, the dipole moment reads as follows:

$$\begin{aligned} &D^i(t) \propto I_i(t) \cdot x_i(t) \propto \\ &\propto \sum_{n=-\infty}^{\infty} e^{jn\omega_0\left[t+\widehat{\tau}_i \sin\left(\Omega_{s_i} t+\varphi_{s_i}\right)\right]} \widehat{x_i} \cos\left[\phi_{\beta_i}(t)\right] = \\ &= \frac{\widehat{x_i}}{2} \sum_{n=-\infty}^{\infty} e^{jn\omega_0\left[t+\widehat{\tau}_i \sin\left(\Omega_{s_i} t+\varphi_{s_i}\right)\right] \pm j\phi_{\beta_i}(t)}, \end{aligned}$$

where $\pm$ denotes the summation over both signs. If one expands $\phi_{\beta_i}(t)$ according to Eq. (2.12), the expression can be arranged into three exponents

$$D^i(t) \propto \frac{\widehat{x_i}}{2} \sum_{n=-\infty}^{\infty} e^{j(n\pm Q)\omega_0 t} e^{j\left(n\widehat{\tau_i} \pm \frac{\widehat{Q_i}}{\Omega_{s_i}}\right)\omega_0 \sin\left(\Omega_{s_i} t+\varphi_{s_i}\right)} e^{j\varphi_{\beta_i}}.$$

Using the Jacobi-Angers expansion, the second exponent may be transformed and the summand takes the following form:

$$\sum_{p=-\infty}^{\infty} J_p\left[\left(n\widehat{\tau_i} \pm \frac{\widehat{Q_i}}{\Omega_{s_i}}\right)\omega_0\right] \; e^{j\left(t\left[(n\pm Q)\omega_0 + p\Omega_{s_i}\right] + \varphi_{\beta_i} + p\varphi_{s_i}\right)}.$$

Assuming that the betatron frequency spread is only due to chromaticity, one has:

$$\widehat{Q_i} = Q\xi \frac{\widehat{p}_i}{p_0},$$

where p_0 is the nominal particle momentum. One also has [80, Eq. (7)] that:

$$\widehat{\tau}_i = \frac{\eta}{\Omega_{s_i}} \frac{\widehat{p}_i}{p_0}, \tag{2.13}$$

where the slip factor η is negative for machines operating above transition energy (such as LHC). For brevity, one can now denote the argument of the Bessel function as

$$\chi^{\pm}_{\widehat{\tau}_i, n} = \left(n\widehat{\tau_i} \pm \frac{\widehat{Q_i}}{\Omega_{s_i}}\right)\omega_0 = (n\eta \pm Q\xi)\frac{\omega_0 \widehat{p}_i}{\Omega_{s_i} p_0}, \tag{2.14}$$

what results in a compact formula:

$$D^i(t) \propto \frac{\widehat{x_i}}{2} \Re\left(\sum_{n,p=-\infty}^{\infty} J_p\left(\chi^{\pm}_{\widehat{\tau}_i, n}\right) \; e^{j\left(t\left[(n\pm Q)\omega_0 + p\Omega_{s_i}\right] + \varphi_{\beta_i} + p\varphi_{s_i}\right)}\right).$$

The value of Q can be decomposed into its integer and fractional part: $Q = Q_I + Q_F$. If the integer part is not zero, the transverse sidebands corresponding to the n-th harmonic of the revolution frequency are, in fact, located around the $n - Q_I$ and $n + Q_I$ harmonics. To derive an expression convenient for studying the spectrum around a given harmonic of the revolution frequency, the sum above should be transformed with the following shift: for every summand the index n is replaced by $n \mp Q_I$ (the choice of sign is opposite to $\chi^{\pm}_{i,n}$). One can do so as every summand remains included in the infinite sum. The dipole moment signal then reads as follows:

$$D^i(t) \propto \frac{\widehat{x_i}}{2} \sum_{n,p=-\infty}^{\infty} J_p\left(\chi^{\pm}_{\widehat{\tau}_i, n\mp Q_I}\right)\ e^{j\left(t\left[(n\pm Q_F)\omega_0 + p\Omega_{s_i}\right] + \varphi_{\beta_i} + p\varphi_{s_i}\right)}, \tag{2.15}$$

where the summand indexed by n describes the vicinity of the n-th harmonic of the revolution frequency.

As shown in Fig. 2.6, the transverse Schottky spectrum of a single particle contains two sidebands, each consisting of a series of Bessel satellites, similar as in the case of a longitudinal spectrum. The distance between the following satellites is given by the synchrotron frequency Ω_{s_i} and the separation between the central satellites on the left and right sideband equals to $2Q_F\omega_0$. If the observed harmonic is much larger than the integer part of the tune, $n \gg Q_I$, both sidebands are symmetric if the chromaticity is close to zero. For bigger values of chromaticity, it can be observed that one of the sidebands is apparently wider than the other.

The derivation of the transverse Schottky spectrum of multiple particles is analogous to the steps taken in the case of the longitudinal spectrum from Eq. (2.7) to Eq. (2.9). The term $\widehat{x_i}$ can be replaced by an average amplitude $\widehat{x}$ assuming that the betatron amplitude is independent from the synchrotron amplitude. Furthermore, due to the presence of a random betatron phase in Eq. (2.15) the derivation is also valid for the central satellite of each sideband. One can express then the total transverse power spectral density P_T as the sum of individual components P_{T_i}:

$$P_T(\omega) = \sum_{i=1}^{N} P_{T_i}(\omega, \widehat{\tau}_i), \tag{2.16}$$

where

$$P_{T_i}(\omega, \widehat{\tau}_i) = P_T^+(\omega, \widehat{\tau}_i) + P_T^-(\omega, \widehat{\tau}_i)$$

and

$$P_T^{\pm}(\omega, \widehat{\tau}) = \sum_{p=-\infty}^{\infty} J_p^2\left(\chi^{\pm}_{\widehat{\tau}, n\mp Q_I}\right) \delta(\omega - (n \pm Q_F)\omega_0 - p\Omega_s(\widehat{\tau})). \tag{2.17}$$

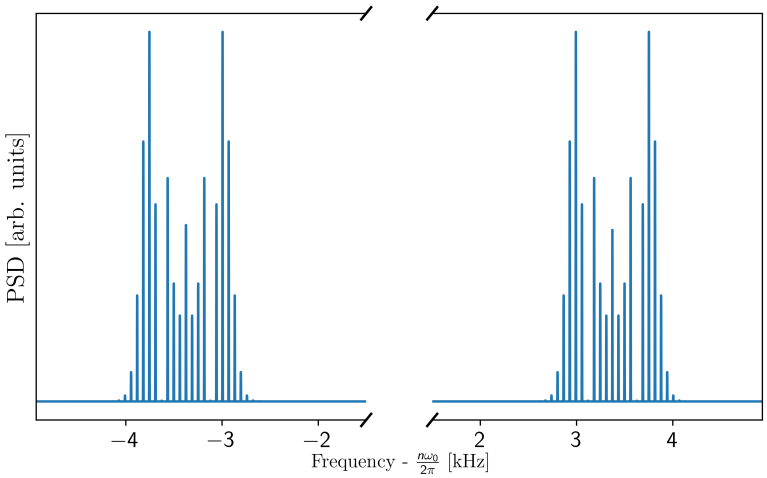

$Q\xi = 0$

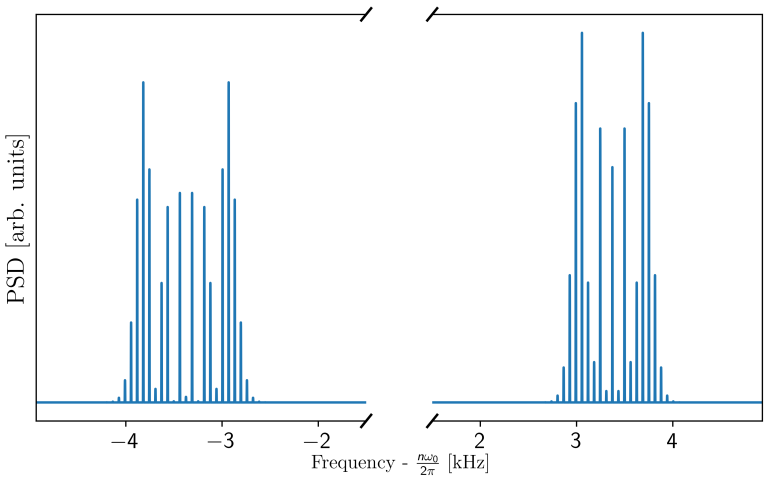

$Q\xi = 15$

Figure 2.6: Single-particle transverse Schottky spectrum.

Also in the transverse case, if one knows the distribution of synchrotron amplitudes $g(\widehat{\tau})$ among the particles, one can substitute Eq. (2.16) with an integral analogue

$$P_T(\omega) = \int_0^\infty g(\widehat{\tau}) P(\omega, \widehat{\tau}) d\widehat{\tau}. \tag{2.18}$$

As shown in Fig. 2.7, central satellites do not dominate the transverse spectrum as was the case for the longitudinal one shown in Fig. 2.5. The values of chromaticity, tune and synchrotron frequency are reflected in the spectrum in the same manner as in the single-particle case, with a complication being that every particle has its own synchrotron frequency and Bessel satellites smear into wider bands.

2.2.3 Chromaticity Formula

There exists in the literature [45, 70, 81–83] a well-known formula which relates the width of the transverse Schottky sidebands to the value of chromaticity $Q\xi$:

$$Q\xi = -\eta \left(n \frac{\Delta f_- - \Delta f_+}{\Delta f_- + \Delta f_+} - Q_I \right), \tag{2.19}$$

where by Δf_- and Δf_+ the width of, respectively, the left and right sideband is denoted. Depending on the adopted definition of tune (see the footnote before Eq. (2.11)), the formula with the $+Q_F$ term instead of $-Q_I$ is also given. However, since in a typical situation one has $n \gg Q$, this does not lead to significant discrepancies.

In the case of a coasted beam, an analogous formula can be derived from the works of Daniel Boussard [84] and Simon van der Meer [85]. For a bunched beam, the result was justified by the assumption that $J_p(x) \approx 0$ for $p > x$ [70], which is only approximately correct, especially for small x. To the best of the author's knowledge, it has never been shown that the result holds in general or what is the exact mathematical definition of the widths, Δf_- and Δf_+, of the sidebands. One could, for example, use the RMS width, or the standard deviation of a fitted Gaussian, or even the width measured at some power threshold. Furthermore, all of these can be calculated either in a linear or logarithmic (dB) scale. In fact, a few different approaches can be found in the available literature [45, 83, 86]. In the following, a formal derivation of Eq. (2.19) for the case of bunched beams will be discussed, with a clarification that the width should be defined as the RMS width of the transverse sideband in a linear scale. What is meant by the RMS width is the standard deviation of the PSD sideband, if treated as a histogram. This is defined by an integral over the frequency range containing the whole sideband, where the integrand is the Power Spectral Density multiplied by the squared distance to the sideband's centre. The RMS width of the transverse sideband can be

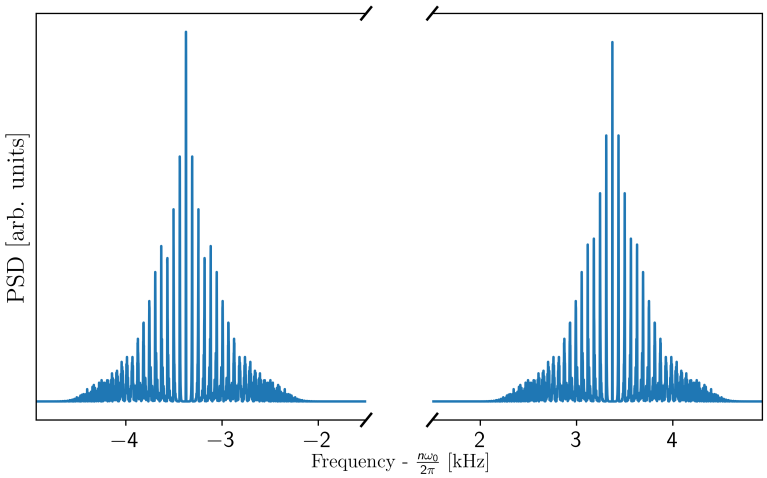

$Q\xi = 0$

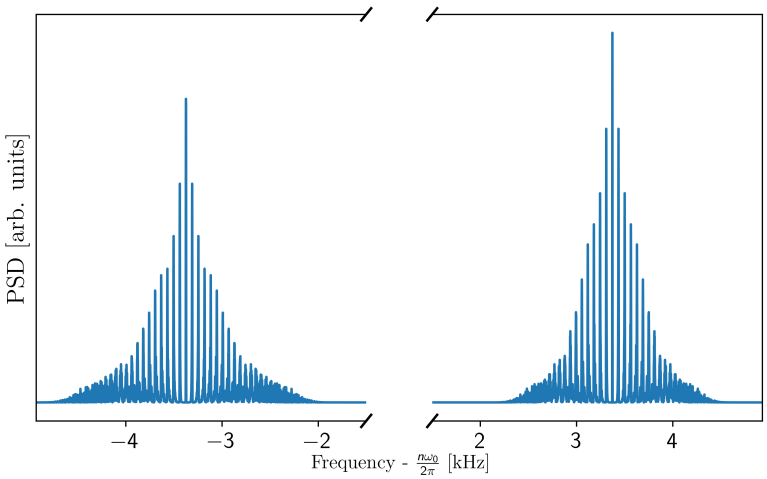

$Q\xi = 15$

Figure 2.7: Multiparticle transverse Schottky spectrum.

calculated using Eqs. (2.17) and (2.18). As the sideband is centred on the frequency $(n \pm Q_F)\,\omega_0$, one derives the RMS width by calculating the square root of the variance

$$\sigma_\pm^2 = \int P_T^\pm(\omega)\,[\omega - (n \pm Q_F)\,\omega_0]^2 \;\; d\omega = \iint_0^\infty g(\widehat{\tau}) P_T^\pm(\omega, \widehat{\tau})\,[\omega - (n \pm Q_F)\,\omega_0]^2 \;\; d\widehat{\tau}\; d\omega.$$

One can now substitute $P_T^\pm(\omega, \widehat{\tau})$, using Eq. (2.17), and obtain

$$\begin{aligned}
\sigma_\pm^2 &= \iint_0^\infty g(\widehat{\tau}) \sum_{p=-\infty}^{\infty} J_p^2\left(\chi^\pm_{\widehat{\tau}, n\mp Q_I}\right) \delta\left[\omega - (n \pm Q_F)\omega_0 - p\Omega_s(\widehat{\tau})\right] [\omega - (n \pm Q_F)\,\omega_0]^2 \;\; d\widehat{\tau}\; d\omega = \\
&= \int_0^\infty \int g(\widehat{\tau}) \sum_{p=-\infty}^{\infty} J_p^2\left(\chi^\pm_{\widehat{\tau}, n\mp Q_I}\right) \delta\left[\omega - (n \pm Q_F)\omega_0 - p\Omega_s(\widehat{\tau})\right] [\omega - (n \pm Q_F)\,\omega_0]^2 \;\; d\omega\; d\widehat{\tau} = \\
&= \int_0^\infty g(\widehat{\tau}) \sum_{p=-\infty}^{\infty} J_p^2\left(\chi^\pm_{\widehat{\tau}, n\mp Q_I}\right) [p\Omega_s(\widehat{\tau})]^2 \;\; d\widehat{\tau} = \int_0^\infty g(\widehat{\tau}) \left(\sum_{p=-\infty}^{\infty} J_p^2\left(\chi^\pm_{\widehat{\tau}, n\mp Q_I}\right) p^2\right) \Omega_s(\widehat{\tau})^2 \;\; d\widehat{\tau}.
\end{aligned}$$

In the above equation, the integration order was changed using a version of the Fubini-Tonelli theorem which holds for generalised functions [87, Chapter 4]. Now using the following property of Bessel function [88, Formula 2.3]:

$$\sum_{p=-\infty}^{\infty} J_p^2(x) p^2 = \frac{x^2}{2},$$

one gets

$$\sigma_\pm^2 = \int_0^\infty g(\widehat{\tau}) \frac{\left(\chi^\pm_{\widehat{\tau}, n\mp Q_I}\right)^2}{2} \Omega_s(\widehat{\tau})^2 d\widehat{\tau}.$$

Substituting $\chi^\pm_{\widehat{\tau}, n\mp Q_I}$, as given in Eq. (2.14), one obtains

$$\begin{aligned}
\sigma_\pm^2 &= \int_0^\infty g(\widehat{\tau}) \frac{\left([(n \mp Q_I)\eta \pm Q\xi]\, \dfrac{\omega_0 \widehat{p}(\widehat{\tau})}{\Omega_s(\widehat{\tau}) p_0}\right)^2}{2} \Omega_s(\widehat{\tau})^2 \;\; d\widehat{\tau} \\
&= [(n \mp Q_I)\eta \pm Q\xi]^2 \int_0^\infty g(\widehat{\tau}) \left(\frac{\omega_0 \widehat{p}(\widehat{\tau})}{2\Omega_s(\widehat{\tau}) p_0}\right)^2 \Omega_s(\widehat{\tau})^2 \;\; d\widehat{\tau} \\
&= [(n \mp Q_I)\eta \pm Q\xi]^2 \cdot C,
\end{aligned}$$

where $C = \int_0^\infty g(\widehat{\tau}) \left(\dfrac{\omega_0 \widehat{p}(\widehat{\tau})}{2\Omega_s(\widehat{\tau}) p_0}\right)^2 \Omega_s(\widehat{\tau})^2 d\widehat{\tau}$ is a positive constant. The notation $\widehat{p}(\widehat{\tau})$ and $\Omega_s(\widehat{\tau})$ is a consequence of Eq. (2.3) and Eq. (2.13).

At this point, it is necessary to note that although $\sigma_\pm := \sqrt{\sigma_\pm^2}$ is by definition positive, the value of $[(n \mp Q_I)\eta \pm Q\xi]$ can be of any sign. One can distinguish two cases:

1. $[(n - Q_I)\eta + Q\xi]$ and $[(n + Q_I)\eta - Q\xi]$ are both positive or both negative,

2. $[(n - Q_I)\eta + Q\xi]$ and $[(n + Q_I)\eta - Q\xi]$ have opposite signs.

For high enough values of n only the first option remains possible.[2] Under this assumption it is straight-forward to check that if one takes $\Delta f_- = \sigma_-$ and $\Delta f_+ = \sigma_+$, then constant C cancels out in Eq. (2.19) and one gets:

$$\begin{aligned}
&-\eta\left(n\frac{\Delta f_- - \Delta f_+}{\Delta f_- + \Delta f_+} - Q_I\right) = \\
=&-\eta\left(n\frac{[(n+Q_I)\eta - Q\xi] - [(n-Q_I)\eta + Q\xi]}{[(n+Q_I)\eta - Q\xi] + [(n-Q_I)\eta + Q\xi]} - Q_I\right) = \\
=&-\eta\left(n\frac{2Q_I\eta - 2Q\xi}{2n\eta} - Q_I\right) = -\eta\left(Q_I - \frac{Q\xi}{\eta} - Q_I\right) = Q\xi.
\end{aligned}$$

If, however, the considered harmonic of the revolution frequency is low, one might find that $[(n \mp Q_I)\eta \mp Q\xi]$ are of opposite signs and Eq. (2.19) should be replaced with

$$Q\xi = -\eta\left(n\frac{\Delta f_- + \Delta f_+}{\Delta f_- - \Delta f_+} - Q_I\right). \tag{2.20}$$

Unfortunately, as it is very likely that in such a case the sign of $[(n \mp Q_I)|\eta| \pm Q\xi]$ strictly depends on the value of $Q\xi$, which is to be determined, the correction introduced by Eq. (2.20) is of very limited practical use.

Equation (2.19) has been therefore rigorously proven for a sufficiently high value of the revolution frequency harmonic n and it has been shown that it holds if $\Delta f_- = \sigma_-$ and $\Delta f_+ = \sigma_+$, with $\sigma_\pm$ calculated using linear scale PSD values.

2. For example, in the case of the LHC Schottky Monitor $n = 427725$, $Q_I = 59$ or 64 and $|\eta| \approx 3.182 \cdot 10^{-4}$, what results in $(n \pm Q_I)|\eta| \approx 136$, to be compared with $Q\xi$ values ranging usually from -20 to 20.

2.3 Diagnostic Techniques Based on Schottky Spectra

The fact that the shape of the Schottky spectrum is determined by the underlying characteristics of the beam can be explored for diagnostic purposes. An extensive overview of the currently used techniques can be found in Ref. [61]. These include the determination of the revolution frequency, betatron tune, emittance and chromaticity, both in the case of coasted and bunched beams. In this section, two new approaches for Schottky-based beam diagnostics are proposed. Apart from being more robust to typical Schottky spectrum imperfections, they allow for a measurement of the longitudinal bunch profile, a characteristic previously not derived from the Schottky spectrum. The idea outlined here is held as general as possible, while the specific implementations are discussed in the following section.

Experimentally, the Power Spectral Density (PSD) is estimated as the time-averaged squared magnitude of the signal's discrete Fourier transform (DFT). The precision of such an estimate depends on multiple factors, the most important being the sampling frequency, sampling time and the adopted windowing function. While considering the time averaging, there is a trade-off between stability of the estimate and sensitivity to the changes in the signal. In the following, it will be assumed, unless explicitly stated, that DFT gives a precise estimate of PSD and this duality will be neglected by using the notation $P(\omega)$ for PSD and $P(\omega_i)$ for the DFT estimate with a certain frequency binning $\omega_1, \ldots, \omega_m$.

2.3.1 Spectra Fitting

The formula that relates the longitudinal Schottky spectrum with the distribution of synchrotron amplitudes, Eq. (2.10), when limited to a discrete set of frequencies, has the following form:

$$P(\omega_i) = \int_0^\infty g(\widehat{\tau}) P(\omega_i, \widehat{\tau}) d\widehat{\tau}. \tag{2.21}$$

Furthermore, if one discretizes $g(\widehat{\tau})$ to a finite set of values $\widehat{\tau_j}$[3], Eq. (2.21) reads

$$P(\omega_i) = \sum_j \widetilde{g}(\widehat{\tau_j}) P(\omega_i, \widehat{\tau_j}),$$

3. Every continuous distribution may be approximated with an arbitrary precision by a discrete distribution.

where $\widetilde{g}(\widehat{\tau}_j)$ is the probability density function of the discrete approximation of $g(\widehat{\tau})$. The above equation can be written in matrix form as:

$$\underbrace{\begin{bmatrix} P(\omega_1,\widehat{\tau}_1) & \cdots & P(\omega_1,\widehat{\tau}_n) \\ P(\omega_2,\widehat{\tau}_1) & \cdots & P(\omega_2,\widehat{\tau}_n) \\ \vdots & \ddots & \vdots \\ P(\omega_m,\widehat{\tau}_1) & \cdots & P(\omega_m,\widehat{\tau}_n) \end{bmatrix}}_{\mathcal{M}} \cdot \underbrace{\begin{bmatrix} \widetilde{g}(\widehat{\tau}_1) \\ \widetilde{g}(\widehat{\tau}_2) \\ \vdots \\ \widetilde{g}(\widehat{\tau}_n) \end{bmatrix}}_{\mathcal{A}} = \underbrace{\begin{bmatrix} P(\omega_1) \\ P(\omega_2) \\ \vdots \\ P(\omega_m) \end{bmatrix}}_{\mathcal{S}}. \tag{2.22}$$

The columns of the matrix $\mathcal{M}$ correspond to the spectra of a single particle which has synchrotron amplitude $\widehat{\tau}_i$. The vector $\mathcal{A}$ represents the discrete approximation of the synchrotron amplitude density and vector $\mathcal{S}$ is the DFT estimate of the Schottky PSD, which can be compared with the experimentally obtained Schottky spectrum. As stated previously, considered frequencies ω_i do not include frequency bins corresponding to the $p = 0$ satellite, as these add up coherently and Eq. (2.21) does not hold. One should also note that matrix $\mathcal{M}$ depends on the nominal synchrotron frequency, so the notation $\mathcal{M}(\Omega_{s_0})$ is used.

The Equation (2.22) has a very convenient form for studying Schottky spectra. It facilitates simulating spectra for different beam conditions and bunch shapes, without the need to perform time-consuming Monte Carlo simulations. All one needs to do is to calculate n single particle spectra with $\widehat{\tau}$ ranging from $\widehat{\tau}_1$ to $\widehat{\tau}_n$ and choose a synchrotron amplitude distribution.

In the case of the transverse Schottky sidebands, one only needs to include two additional parameters, betatron tune and chromaticity, so that the expanded matrix equation reads:

$$\underbrace{\begin{bmatrix} P_T^{\pm}(\omega_1,\widehat{\tau}_1,\Omega_{s_0},Q,Q\xi) & \cdots & P_T^{\pm}(\omega_1,\widehat{\tau}_n,\Omega_{s_0},Q,Q\xi) \\ P_T^{\pm}(\omega_2,\widehat{\tau}_1,\Omega_{s_0},Q,Q\xi) & \cdots & P_T^{\pm}(\omega_2,\widehat{\tau}_n,\Omega_{s_0},Q,Q\xi) \\ \vdots & \ddots & \vdots \\ P_T^{\pm}(\omega_m,\widehat{\tau}_1,\Omega_{s_0},Q,Q\xi) & \cdots & P_T^{\pm}(\omega_m,\widehat{\tau}_n,\Omega_{s_0},Q,Q\xi) \end{bmatrix}}_{\mathcal{M}(\Omega_{s_0},Q,Q\xi))} \cdot \underbrace{\begin{bmatrix} \widetilde{g}(\widehat{\tau}_1) \\ \widetilde{g}(\widehat{\tau}_2) \\ \vdots \\ \widetilde{g}(\widehat{\tau}_n) \end{bmatrix}}_{\mathcal{A}} = \underbrace{\begin{bmatrix} P_T^{\pm}(\omega_1) \\ P_T^{\pm}(\omega_2) \\ \vdots \\ P_T^{\pm}(\omega_m) \end{bmatrix}}_{\mathcal{S}}. \tag{2.23}$$

The left-hand sides of Eq. (2.22) and Eq. (2.23) can be interpreted as models which, given the correct set of parameters, give vector $\mathcal{S}$ matching the experimentally measured spectrum. Inverting the problem, and given an experimental spectrum, one may try to fit these parameters in such a way that the resulting model predicts a spectrum $\mathcal{S}$ that coincides with the measured one. Furthermore,

it is possible to arbitrarily exclude any frequency of the spectrum from the analysis by simply removing the corresponding bins from the $\mathcal{S}$ and rows from the $\mathcal{M}$ matrix.

To determine the correct values of the longitudinal beam characteristics, that is Ω_{s_0} and $\mathcal{A}$, one can look for values that minimise the following cost function:

$$C\left(\Omega_{s_0}, \mathcal{A}\right) = \left|\log\left[\mathcal{M}\left(\Omega_{s_0}\right) \cdot \mathcal{A}\right] - \log\left[\mathcal{S}_{exp}\right]\right|^2, \tag{2.24}$$

The log functions are taken point-wise and $|\cdot|$ is the standard Euclidean norm. The logarithm of the measured and simulated spectrum is taken in order to be more sensitive to the low-magnitude spectral periphery and more robust to noise, as it was observed that the noise level in experimental spectra is proportional to the power spectral density at a given frequency.

Although the distribution of synchrotron amplitudes might seem like a rather rarely used characteristic, in the case of no intra-bunch coherent motion, it is strictly related with the longitudinal bunch profile. An invertible functional that connects these two is given by

$$\mathcal{B}(\tau) = \int_{|\tau|}^{\infty} \frac{g_{\widehat{\tau}}(\widehat{\tau})}{\pi\sqrt{\widehat{\tau}^2 - \tau^2}} d\widehat{\tau}. \tag{2.25}$$

The derivation of the above formula is presented in Appendix A.

In the case of the transverse spectrum, to determine the correct values of $\Omega_{s_0}, Q, Q\xi$ and $\mathcal{A}$ one looks for values that minimise a cost function analogous to Eq. (2.24):

$$C\left(\Omega_{s_0}, Q, Q\xi, \mathcal{A}\right) = \left|\log\left[\mathcal{M}\left(\Omega_{s_0}, Q, Q\xi\right) \cdot \mathcal{A}\right] - \log\left[\mathcal{S}_{exp}\right]\right|^2. \tag{2.26}$$

Finding a solution to non-linear problems is not always possible analytically. For that reason, the parameters that minimise Eqs. (2.24) and (2.26) should be searched using one of the minimising routines, such as *Differential Evolution* [89] or *L-BFGS-B* [90] algorithms.

It is obvious that the experimental spectrum is susceptible to noise and finite-time averaging effects. Without putting any constraints on the shape of $\mathcal{A}$, it may therefore happen that the pair $(\Omega_{s_0}, \mathcal{A})$ that minimises Eq. (2.24) is different from the true nominal synchrotron frequency and synchrotron amplitude density. An example of such a situation is illustrated in Fig. 2.8, which presents the synchrotron amplitude distribution obtained by Differential Evolution minimisation of Eq. (2.24) with $\mathcal{S}_{exp}$ being a sample LHC Schottky spectrum. The resulting rather exotic shape of the estimated amplitude distribution and associated bunch shape is in stark contrast to the direct measurement of the bunch profile acquired independently with a Wall Current Monitor (WCM).

One of the possible solutions to overcome this issue is based on the assumption that synchrotron

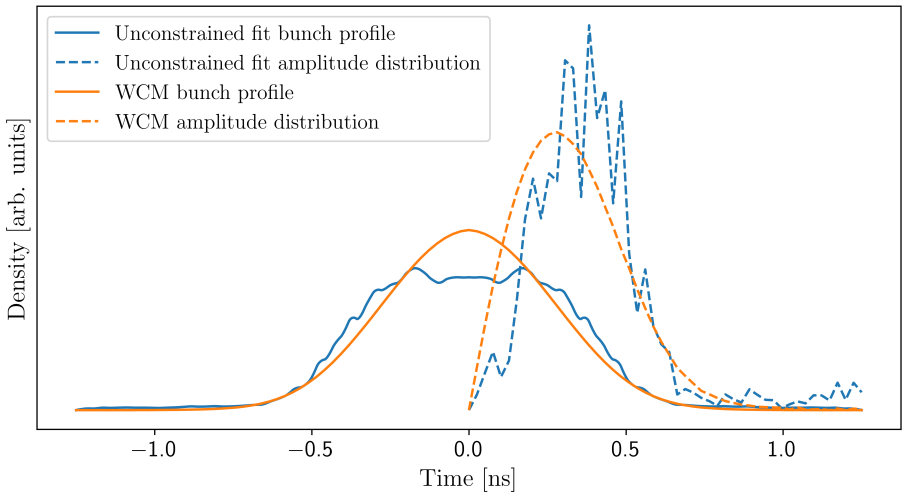

Figure 2.8: LHC WCM bunch profile and results of unconstrained bunch profile fitting.

amplitude densities follow a Rice distribution [91], which is the distribution of distances from the origin for samples taken from a circular 2D normal distribution. It is determined by two parameters, standard deviation $\sigma_{\mathcal{N}_{2D}}$ and the modulus of mean $\nu_{\mathcal{N}_{2D}}$ of the mentioned 2D-normal distribution[4]. The correlation between the Rice distribution and the distribution of synchrotron amplitudes is plausible at the time of injection, since the synchrotron amplitude is proportional to the distance from the origin in the longitudinal phase space. During the later phases of beam circulation, this assumption can be based on observations of bunch shapes measured by the LHC WCM at different beam phases, and their corresponding synchrotron amplitude densities, calculated based on Eq. (2.25), which confirms this hypothesis. Typical amplitude distributions of LHC ion beams, together with the corresponding Rice distribution fits, are presented in Fig. 2.9. This assumption may be seen as a regularisation, that is, introducing an additional constraint which helps to solve an ill-posed problem by preventing solutions from wrongly compensating the errors. Furthermore, the number of parameters fitted would now be dramatically reduced, from n parameter entries in vector $\mathcal{A}$ ($n = 50$ in the example shown in Fig. 2.8), to only 2 parameters: $\nu_{\mathcal{N}_{2D}}$ and $\sigma_{\mathcal{N}_{2D}}$.

2.3.2 Direct Betatron Tune Calculation

According to the theory recalled in subsection 2.2.2, each of the transverse sidebands should be symmetric. The axis of symmetry coincides with the p-zero Bessel satellite, for which the frequency is equal to $(n \pm Q_F)\omega_0$. Therefore, the detection of this satellite enables us to determine the tune

4. Note that $\sigma_{\mathcal{N}_{2D}}$ and $\nu_{\mathcal{N}_{2D}}$ are generally not equal to the standard deviation and mean of the Rice distribution.

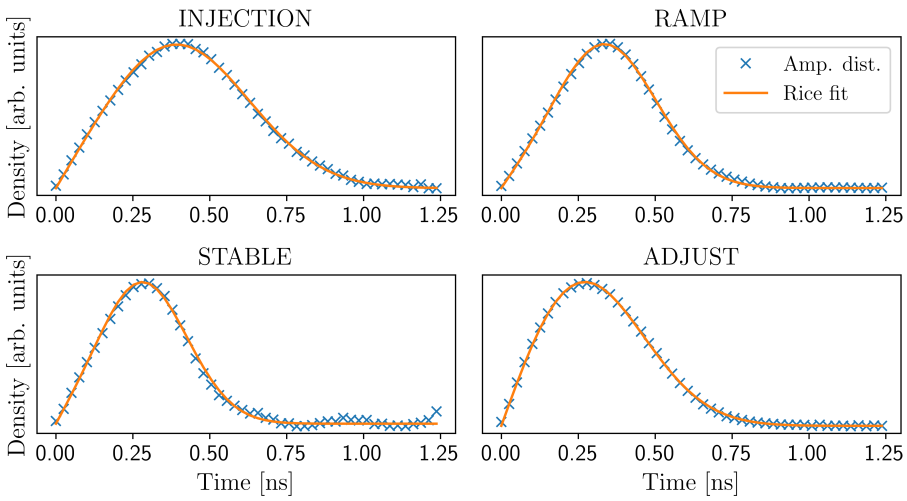

Figure 2.9: Synchrotron amplitude distributions during different beam conditions.

value.

Analysing previously proposed methods for Schottky-based tune measurements [45, 81, 92], they can be grouped into two types. The first is based on peak detection, followed by the estimation of which peak is most likely the p-zero satellite. One considered feature is the height; however, there is no guarantee that the central satellite has the highest power. Alternatively, the overall shape of the transverse sideband is considered, and by means such as curve fitting or weight averaging, the centre of the sideband is determined, even if it does not correspond to a local maximum. The biggest drawback of this approach is the poor robustness to non-symmetric shapes of the sidebands.

A new method of tune calculation, called *Mirrored Difference* (MD) method, can be proposed. It exploits the fact that even in cases where the overall shape of the transverse hump is distorted, one still observes a correlation between the power of the corresponding left and right Bessel p-satellites. Let the cost function be defined as

$$C_{MD}(m) = \sum_{i=1}^{i=N} |P_T(\omega_{m-i}) - P_T(\omega_{m+i})|, \tag{2.27}$$

where $P_T(\omega_n)$ is the power of the n-th point in the spectrum and N is the range parameter, which should correspond to the expected sideband width. Scanned values of i are limited to those corresponding to one of the transverse sidebands, but the generalisation to include both sidebands is straightforward. The value of m which minimises the above cost function indicates the frequency bin of $(n \pm Q_F)\omega_0$. In addition, a supplementary check can be performed by confirming that the detected frequency bin is indeed a local maximum. This can be done simply by comparing the value of $P_T(\omega_n)$

with the average power in the sideband. That should be enough, as it immediately excludes the valleys in between satellites, leaving only the local maxima as possible points of symmetry. Finally, interpolation techniques can be used to increase the point density in the spectrum and even more decrease C_{MD}. It should be noted that the presence of irregularities or artefacts outside the central region of the sideband affects nearly all summands in Eq. (2.27) in a comparable way. As a result, an additional artificial peak cannot "drag" the calculated tune towards itself, unless its power is so large that the corresponding frequency minimises the cost function despite the induced asymmetry.

The robustness of the *Mirror Difference* method compared to the curve fitting procedure can be observed in Fig. 2.10. Although the dominant central satellite is relatively easily noticeable, the artificial peaks present in the left part of the spectrum influence the curve fitting routines and deteriorate the tune estimate. Meanwhile, the MD algorithm does not find peaks corresponding to spurious satellites and adds their contribution to the value of the cost function for nearly all scanned frequencies. That way, the frequency which minimises the location does not change with respect to the situation when artefacts are not present.

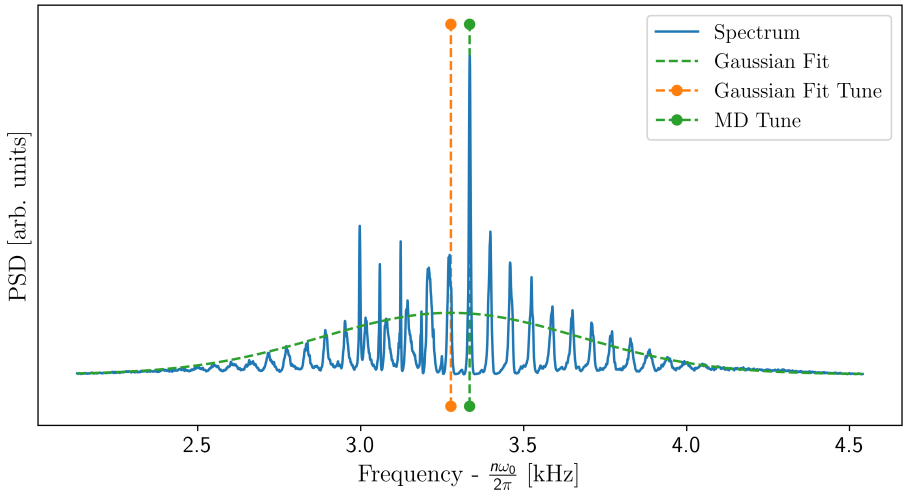

Figure 2.10: Example of Gaussian fitting and *Mirror Difference* tune estimate.

2.4 Estimation of LHC Beam Characteristics

Methods of beam diagnostics based on the Schottky spectrum, which were presented in the previous sections, have been tested offline using real data acquired with the LHC Schottky monitor at the end of LHC Run 2 (Autumn 2018), during the ion (Pb^{82+}) campaign. As the evaluation of a diagnostic technique requires knowledge of the diagnosed parameter, it was necessary to use the Schottky spectra acquired in parallel with the independent measurements of the characteristic of interest. The first analysis, concerning only the estimation of longitudinal characteristics, was done by comparing the longitudinal bunch profiles obtained by analysing the horizontal and vertical LHC Schottky spectra with the measurements of the LHC Wall Current Monitor. The second, more complex analysis had the primary goal of checking the effectiveness of transverse characteristics estimation, but also included studies on how different Schottky-based methods can interact with each other and with external sources of information. As the only alternative method of chromaticity measurement in the LHC is based on the RF modulation of the beam and is therefore invasive, the choice of the analysed Schottky spectrum had to be limited to the spectra acquired directly *before* the RF modulation began. In addition, with the use of RF modulation, chromaticity is measured almost exclusively at low beam energy and intensity.

As a whole, the LHC Schottky system consists of four modules, one for each beam and each transverse (horizontal or vertical) plane. Each module is made up of two slot-coupled waveguides operating at 4.8 GHz, located at the opposite sides of the beam pipe. Coupled signals are combined with a delta-hybrid in order to reduce the longitudinal component of the Schottky signal. Complete elimination is not possible due to finite positioning precision and beam displacement. The system is equipped with a fast gate switch, which enables the observation of an arbitrarily chosen subset of circulating bunches. By default, the monitor is gated only on one bunch. During the back-end processing, the signal is sequentially down-mixed, in 3 stages, to 11.2 kHz and digitised by a 24-bit digitizer at the rate of 4 $f_0 \approx 4 \cdot 11245.5$ Hz. Additional information and extensive details on the architecture of the LHC Schottky Monitor system can be found in Ref. [45]. In the post-processing phase, since the goal is a real-time measurement with a 1 second rate, the FFT is calculated based on the most recent ≈1.46 second chunk of data. It gives 32768 frequency bins and a spectral resolution of approximately 0.69 Hz. Such a resolution is high enough to observe the inner structure of the Bessel satellites, which is crucial for the analysis. Random fluctuations of the spectrum are reduced by time averaging the spectra using an exponential moving average ($\alpha = 0.02$). The final effect of the pre-processing of data can be observed in Fig. 2.11. It consists of three sidebands, the central represents the longitudinal intensity signal, while the left and right ones correspond to the

transverse dipole moment contribution. The most prominent component is the central satellite of the longitudinal sideband, whose significant power reflects the fact that the power of each particle adds up coherently at this frequency. The asymmetry between the two transverse sidebands reveals a non-zero value of chromaticity.

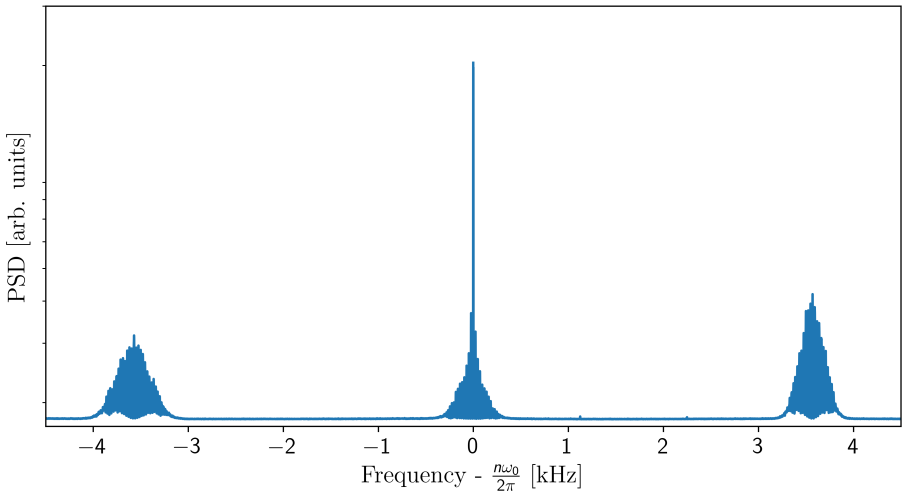

Figure 2.11: LHC Schottky spectrum.

2.4.1 Longitudinal Characteristics

The validity of the longitudinal characteristics estimation method described in subsection 2.3.1 has been verified based on the analysis of Schottky spectra collected during the night between 7 and 8 November 2018 (LHC fill 7421) with horizontal and vertical Beam 2 LHC pick-ups at the nominal beam energy. Obtained results were compared with longitudinal bunch profiles acquired with the LHC Wall Current Monitor. The range of frequencies included in Eq. (2.22) has been limited to 2854 values that satisfy the condition

$$|f - nf_0| \in [20, 1000 \text{ Hz}]. \tag{2.28}$$

Figure 2.12 shows that this condition excludes the central satellite, what is necessary as in this frequency region Eq. (2.9) is not valid.

The frequency range in Eq. (2.28) had to be chosen in such a way that it included a significant part of the longitudinal Schottky spectrum. The width of the longitudinal sideband depends on multiple parameters, such as the harmonic of the revolution frequency, bunch length and the synchrotron frequency. In the case of beams observed with the LHC Schottky Monitor, only the last

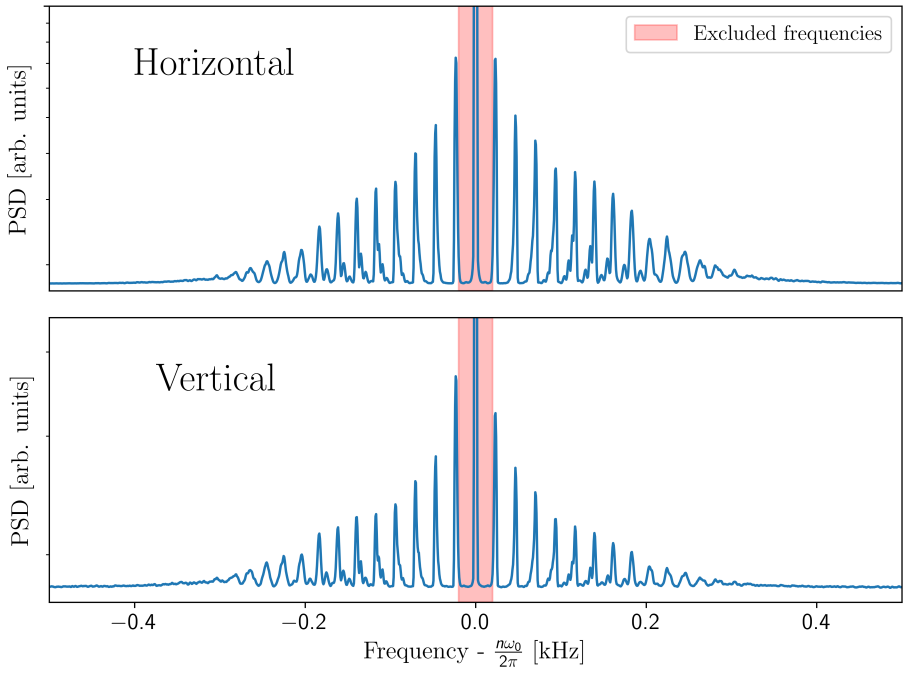

Figure 2.12: LHC Schottky spectrum used for longitudinal characteristics determination.

one changes significantly during the beam cycle, and for that reason the spectrum at the injection energy would require a wider frequency range.

The number of considered synchrotron motion amplitudes $\widehat{\tau}_i$, that is the number of columns of $\mathcal{M}(\Omega_{s_0})$ in Eq. (2.22), was set to $n = 50$, as a trade-off between the computational load and the discretization error. It turned out to give satisfactory results, but the impact of this choice was not rigorously investigated. Following the observation of typical LHC synchrotron amplitude distributions, the Rice form of the distribution was assumed. The parameters that gave the best spectrum fit were determined using a Differential Evolution algorithm implemented in a SciPy library [93]. With the exception of *popsize* $= 60$ and *mutation* $= (0.5, 1.2)$ the default algorithm settings were used. The matrices $\mathcal{M}(\Omega_{s_0})$ were precalculated in order to reduce the computation time needed for the evaluation of the cost function.

The cost function given by Eq. (2.24) was modified in order to address certain practical issues connected with the spectra analysis. As the magnitude of the observed PSD depends on the beam intensity, a scale parameter c_1 has been introduced. Moreover, low power components of the spectrum might be masked by the noise so that only the top part of the spectrum would be visible. In order to emulate this effect an additional parameter c_2 is used. Together with three previously discussed parameters: nominal synchrotron frequency Ω_{s_0}, $\nu_{\mathcal{N}_{2D}}$ and $\sigma_{\mathcal{N}_{2D}}$ of the Rice distribution,

the new cost function had five arguments and the following form:

$$C\left(\Omega_{s_0}, \mathcal{A}, c_1, c_2\right) = \left|\log\left[\max\left\{c_1 \mathcal{M}\left(\Omega_{s_0}\right) \cdot \mathcal{A} - c_2, \mathcal{S}_{min}\right\}\right] - \log\left[\mathcal{S}_{exp}\right]\right|^2, \tag{2.29}$$

where $\mathcal{S}_{min}$ is the minimal value of $\mathcal{S}_{exp}$. It was observed that in the case of analysed spectra the determined value of the noise parameter c_2 was negligible.

To increase the convergence rate, the parameters were bounded within ranges broad enough to include all possible physical solutions according to the machine configuration. The bounds for Ω_{s_0}, $\nu_{\mathcal{N}_{2D}}$ and $\sigma_{\mathcal{N}_{2D}}$ are specified in Table 2.1. The scale parameter c_1 was assumed to be such that the values of $c_1 \mathcal{M}\left(\Omega_{s_0}\right) \cdot \mathcal{A}$ and $\mathcal{S}_{exp}$ are comparable. As distinct columns of $\mathcal{M}\left(\Omega_{s_0}\right)$ have approximately equal sums and $\mathcal{A}$ sums up to one, the scale parameter was expected to be approximately equal to $\text{sum}\left\{\mathcal{S}_{exp}\right\} / \text{sum}\left\{\mathcal{M}_{\cdot,i}\left(\Omega_{s_0}\right)\right\}$, where $\text{sum}\left\{\mathcal{M}_{\cdot,i}\left(\Omega_{s_0}\right)\right\}$ is the sum of an arbitrary single column. The bounds were therefore set in such a way that a one-order-of-magnitude range around the expected value of c_1 was scanned. The noise parameter c_2 should be a fraction of $\max\left\{\mathcal{S}_{exp}\right\}$. Nevertheless the whole range $\left[0, \max\left\{\mathcal{S}_{exp}\right\}\right]$ was scanned.

Table 2.1: Parameter bounds used for longitudinal Schottky spectrum analysis

$\sigma_{\mathcal{N}_{2D}}$	$\nu_{\mathcal{N}_{2D}}$	$f_{s_0} = \Omega_{s_0}/2\pi$
0 - 0.5 ns	0 - $5\sigma_{\mathcal{N}_{2D}}$	20-25 Hz

The first assessment of the spectra-fitting method could be performed by looking at the precision of the fit itself. In Fig. 2.13 an example comparison is shown between the experimental spectrum (in blue), and the spectrum obtained with a fitting procedure (in orange). The calculated spectrum follows very well the overall experimental spectrum, including the fine details of the internal structure of the Bessel satellites.

Finally, knowing the distribution of the synchrotron amplitudes one can use Eq. (2.25) and calculate the longitudinal bunch profile, which can be compared with an independent measurement. Such a comparison is shown in Fig. 2.14 where a longitudinal bunch profile acquired with the WCM is compared with bunch profiles calculated based on the analysis of twenty Schottky spectra acquired from both planes within 50 s before and after the WCM measurement.

The results of the analysis have shown the potential of the spectra fitting procedure for beam diagnostics. It turned out to be capable of estimating the longitudinal bunch profile and other less frequently studied characteristics, such as synchrotron amplitude and frequency distributions. Although this accomplishment might seem redundant due to the availability of the LHC Wall Current Monitor, one can mention at least two counterarguments. Firstly, calculating the synchrotron

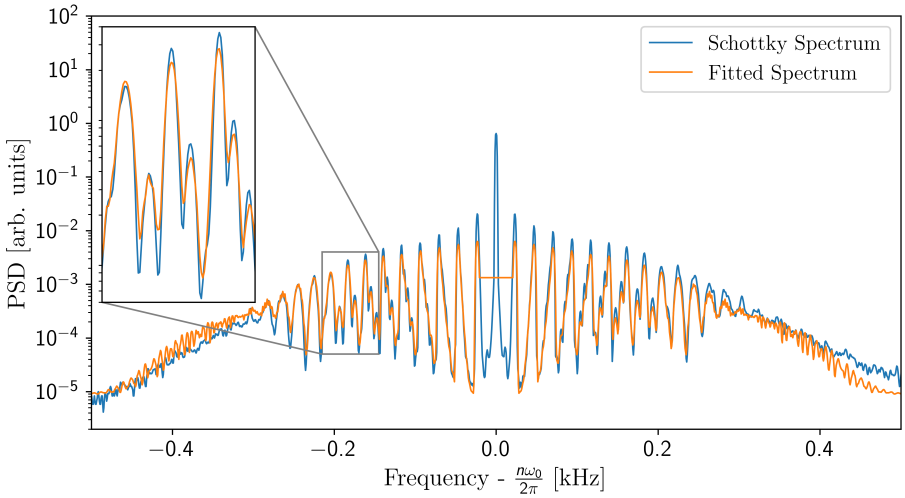

Figure 2.13: Fitted and experimental LHC Schottky spectrum.

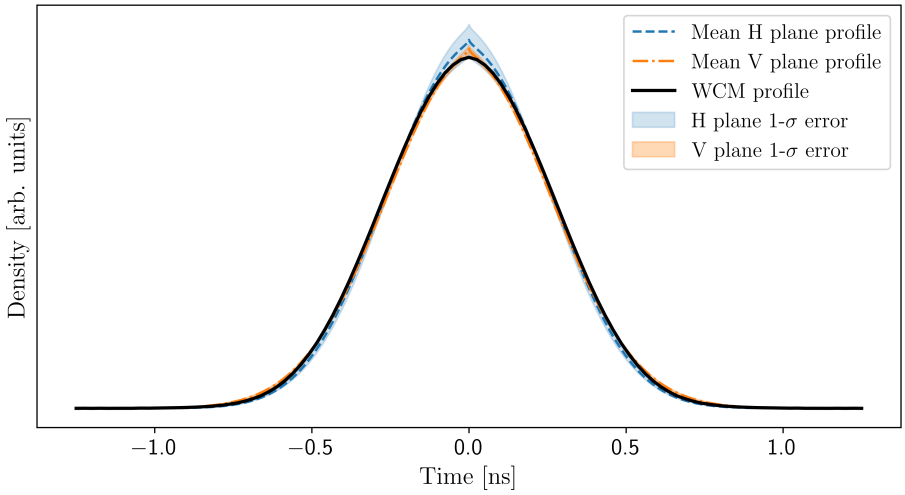

Figure 2.14: Schottky-based and WCM longitudinal bunch profiles.

amplitude distribution is the first step towards transverse Schottky spectrum fitting, which would determine the value of chromaticity. For this quantity, there is no alternative noninvasive instrument available in the LHC. Secondly, the comparison of the longitudinal profiles obtained independently from the WCM and based on the Schottky spectrum might serve as a quality assessment for the Schottky spectra. If the profiles would not match, then also the other quantities derived from the Schottky spectrum should be treated as potentially erroneous.

2.4.2 Transverse Characteristics

The study on the derivation of transverse beam characteristics from the LHC Schottky spectrum was based on the analysis of the data acquired in November 2018 during three distinct LHC Pb^{82+} fills: 7435, 7443 and 7486. In all cases the diagnosed beam is at injection energy, as only at such an energy the reference chromaticity measurements obtained with the RF modulation technique were available. Both beams are represented in the dataset: for fill 7435 beam 1 data is analysed, while for fills 7443 and 7486 the focus is set on beam 2. As in the case of the previous longitudinal study, the signal from both horizontal and vertical planes is used.

Instead of focusing entirely on the spectrum fitting approach, or on Schottky spectra analysis in general, it is worth looking at the problem of estimation of transverse characteristics from a broader perspective. From Eq. (2.23) it follows that the transverse Schottky spectrum is determined by four characteristics: synchrotron amplitude distribution, nominal synchrotron amplitude, betatron tune and chromaticity. One might try to directly determine them all by fitting at once the entire Schottky spectrum, but this is not the only possibility. The nominal synchrotron frequency and distribution of synchrotron amplitudes can also be determined by fitting solely the longitudinal spectrum; they can also be derived externally, by means different from Schottky spectrum analysis. As follows from Eq. (2.25), under the assumption of no intra-bunch coherent motion, the distribution of synchrotron amplitudes can be calculated from the longitudinal bunch profile, acquired for example with the Wall Current Monitor. The nominal synchrotron frequency can also be obtained from other diagnostics or from calculations based on the parameters of the RF system [94, 95]. Betatron tune and chromaticity could in principle be obtained from the Schottky spectrum without using a fitting procedure, as discussed in subsection 2.2.3 and subsection 2.3.2. One can see that there exists a redundancy in the number of procedures available for the estimation of a given characteristic. For spectra fitting, this redundancy can be used either as a cross-check or as a way to improve the fitting quality by providing external constant parameters and reducing the number of parameters to be fit. It is important to note that while performing a fitting procedure, one cannot exclude any parameter which has an impact on the spectrum. These include the distribution of the synchrotron amplitudes and arguments of the $\mathcal{M}$ matrices of Eq. (2.22) and Eq. (2.23). They all need to either be determined through the cost function minimisation or provided as a constant parameter. A summary of available methods is presented in Fig. 2.15. Characteristics denoted with a "+" sign can be derived independently, while those with a number, present in "fitting boxes", have to be handled with all others in a box.

As the methods shown in Fig. 2.15 may be mixed in several ways, it is worth to test at least

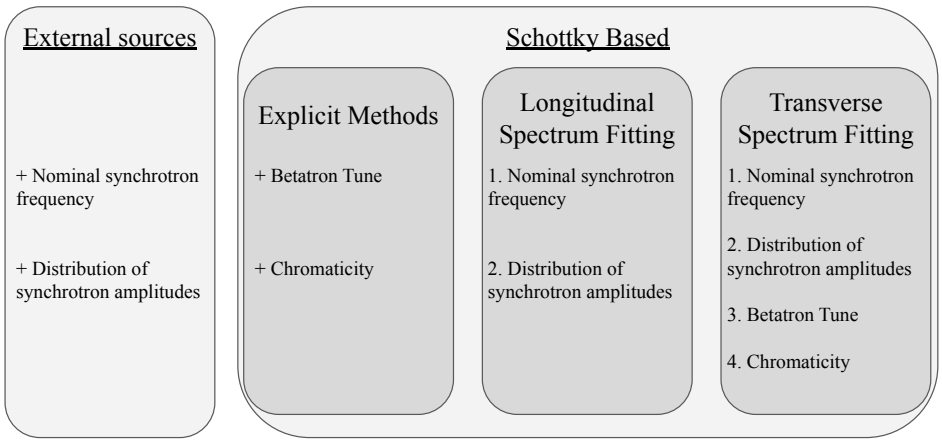

Figure 2.15: Set of diagnostic methods which can be used in Schottky spectrum analysis.

a few combinations which are most representative for typical use cases. The selected scenarios are listed below.

Scenario 1

In the first considered scenario, both the betatron tune and the chromaticity are calculated based on the methods presented in subsection 2.2.3 and subsection 2.3.2. Such a scenario is schematically presented in Fig. 2.16. It requires, however, a signal of very good quality, as one is not able to exclude any part of the spectrum. In addition, the unavoidable presence of noise, and especially of spurious spectral peaks, can have a very strong impact on the RMS widths of the transverse sidebands, thus causing errors in the calculated chromaticity.

Scenario 2

In most cases, at least in the case of LHC, chromaticity cannot be accurately calculated using Eq. (2.19). In such cases, one has to fit the transverse sidebands, or a subset of them, according to the procedures discussed in subsection 2.3.1. In order to constraint the solution space to a plausible region, it is sometimes desirable to perform the analysis sequentially and to fit as few parameters at each stage as possible. An example of such a strategy is presented in Fig. 2.17. It is assumed that the nominal synchrotron frequency is known, either through the precise knowledge of RF parameters or from external diagnostics. The betatron tune value is estimated directly from the Schottky spectrum, according to the procedure described in subsection 2.3.2. This method has proven to be very robust and can be applied in most cases. Knowing the nominal synchrotron frequency, one can determine the distribution of synchrotron amplitudes by fitting the longitudinal portion of the

Schottky spectrum. Finally, only chromaticity is left to be determined through transverse fitting, or, in this case, scanning a predefined grid of possible values of chromaticity.

Scenario 3

In certain circumstances, for example, in the presence of coherent intra-bunch motion which not only distorts the longitudinal spectrum but also greatly complicates the relation between the bunch profile and the distribution of synchrotron amplitudes, it may occur that one simply cannot fit the longitudinal part of the Schottky spectrum. Furthermore, it might be that no useful information is available from external devices. In such cases, one can only rely on the information contained in the transverse sidebands of the Schottky spectrum, as denoted in Fig. 2.18. The betatron tune is calculated according to the procedure described in subsection 2.3.2. The nominal synchrotron frequency, distribution of synchrotron amplitudes and the chromaticity are obtained simultaneously by fitting the transverse spectrum.

Scenario 4

The last considered scenario, see Fig. 2.19, can be seen as an enhanced version of the third scenario. Again, all parameters, apart from the betatron tune, are fitted within a single fitting routine. This time, however, one fits simultaneously both the longitudinal and transverse portions of the Schottky spectrum. In the case of a reliable longitudinal spectral region, this scenario has a clear advantage over the third scenario, as it provides more constraints on the fitted parameters. It also represents the most straightforward approach for the simultaneous estimation of all parameters given the entire set of available data.

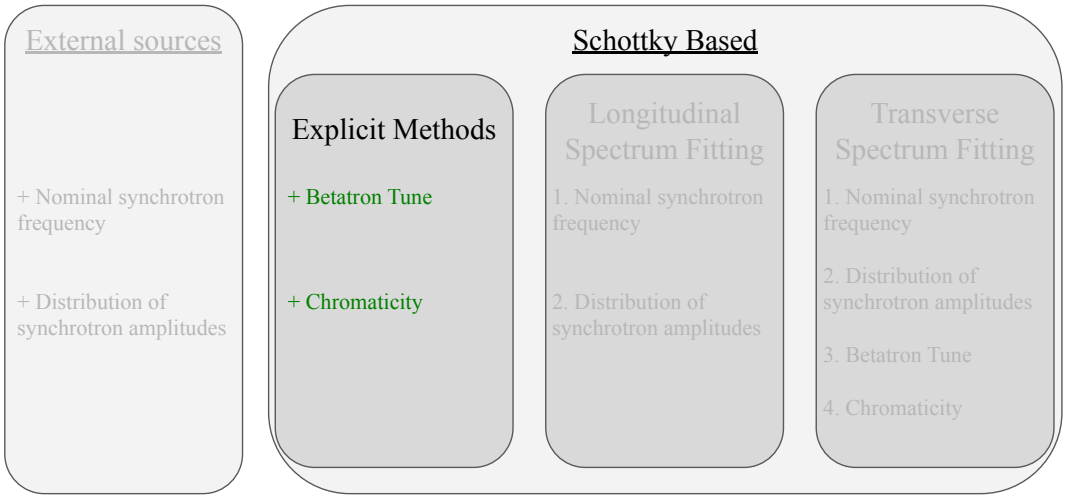

Figure 2.16: Transverse Schottky analysis diagram of Scenario 1.

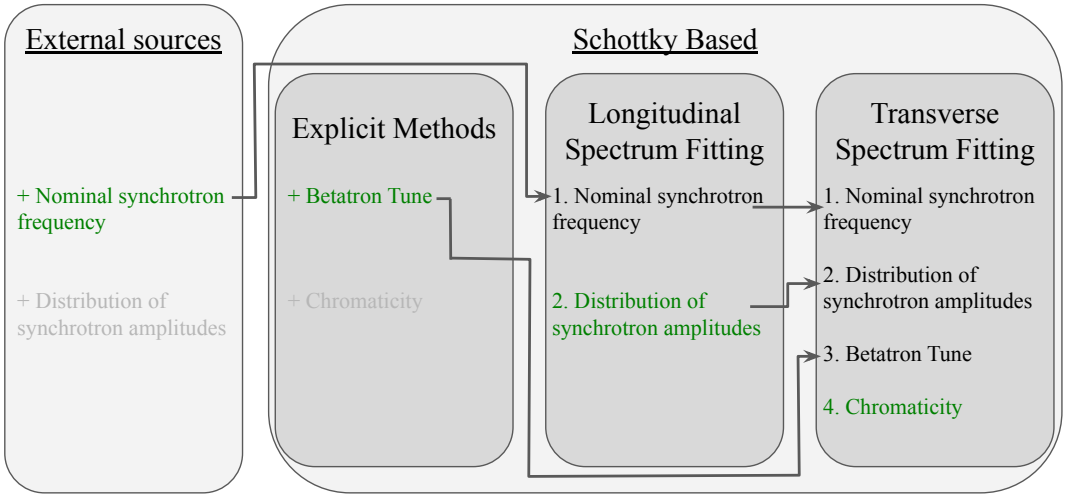

Figure 2.17: Transverse Schottky analysis diagram of Scenario 2.

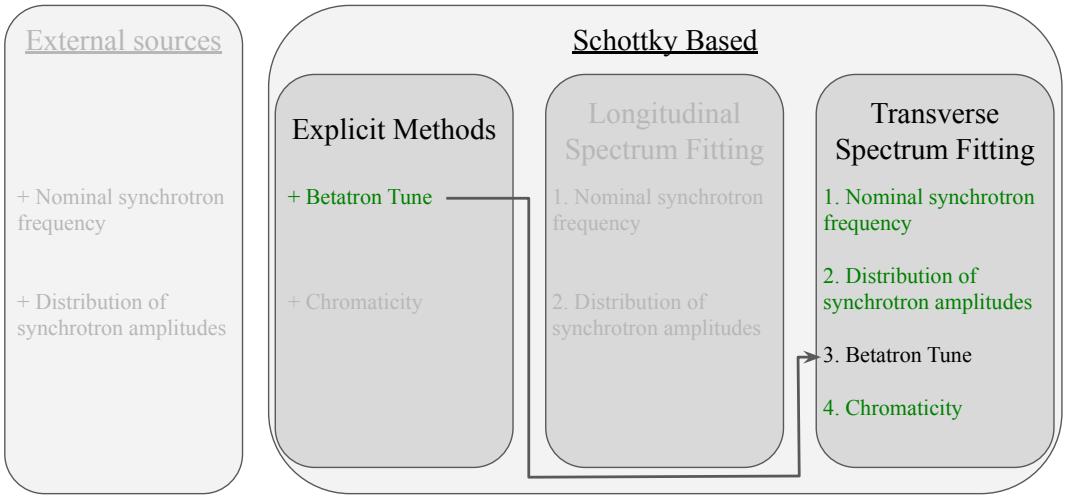

Figure 2.18: Transverse Schottky analysis diagram of Scenario 3.

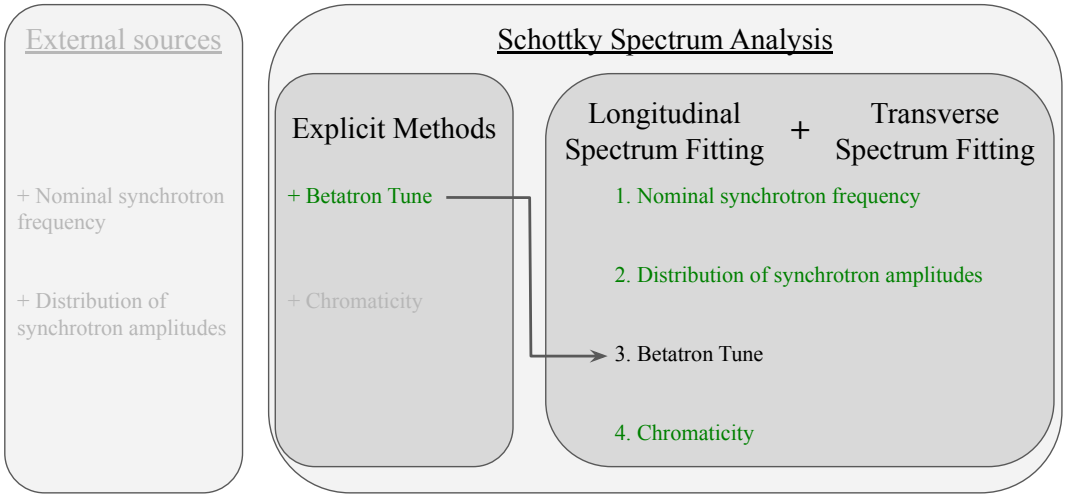

Figure 2.19: Transverse Schottky analysis diagram of Scenario 4.

As mentioned previously, the fitting procedures do not require taking the whole Schottky spec-

trum into consideration. A subset of frequencies at which the fit was performed is shown in Fig. 2.20. The analysed dataset includes 12 frequency bands denoted with the letters A-F (horizontal spectrum) and G-L (vertical spectrum). In addition, as visible in this example, frequency ranges can be chosen in such a way that possible artefacts overlapping the sidebands are conveniently excluded.

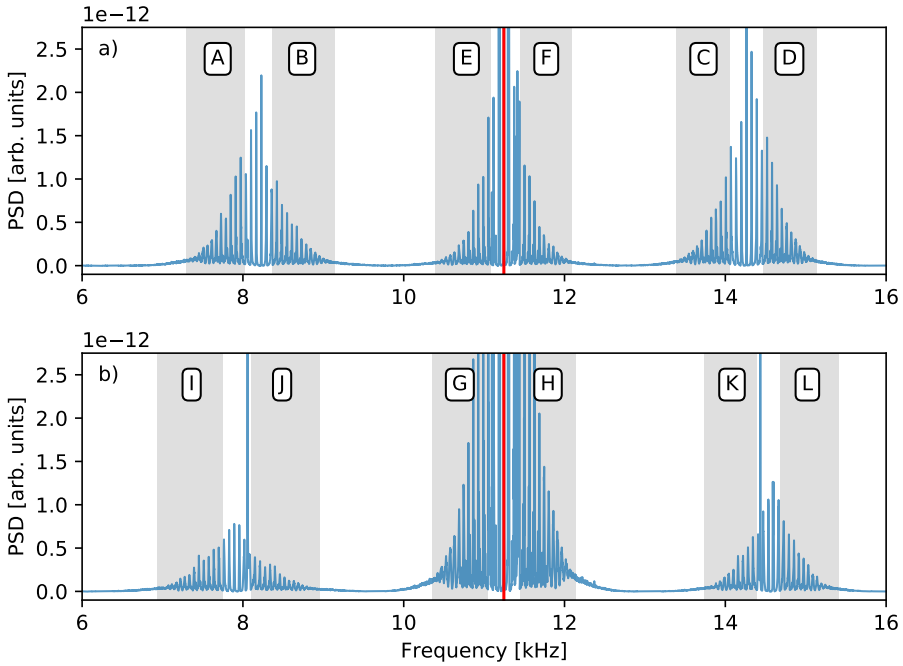

Figure 2.20: Frequency ranges used in the transverse Schottky fitting procedures.

During the analysis described in this subsection, the technical details of the spectra fitting procedure were a bit different in comparison to the fitting performed previously for the longitudinal spectrum. This time, instead of the Differential Evolution algorithm, the L-BFGS-B routine was used for the minimisation of Eq. (2.26). Moreover, PSD within each frequency region is processed in such a way that additional scale and noise parameters, present in Eq. (2.29), are not needed. Firstly, the baseline is removed from the experimental spectra, so that the minimal power within each band is equal to zero[5]. Then, the simulated spectra are scaled in each region in such a way that the total cumulative power is equal to the power of the experimental spectrum.

For each distinct scenario that involves fitting, the fitting results are presented separately for every region marked in Fig. 2.20. To reduce the number of plots, only the fits corresponding to fill 7443 are presented. As seen in Figs. 2.21 to 2.23 the spectra are well reproduced down to the

5. Actually, in order to avoid the singularity in the logarithmic function, a small value of $\epsilon = 10^{-20}$ is taken instead of zero.

level of substructures of the Bessel satellites. Inconsistencies in the power level might, however, suggest not sufficient averaging time of the Schottky spectra.

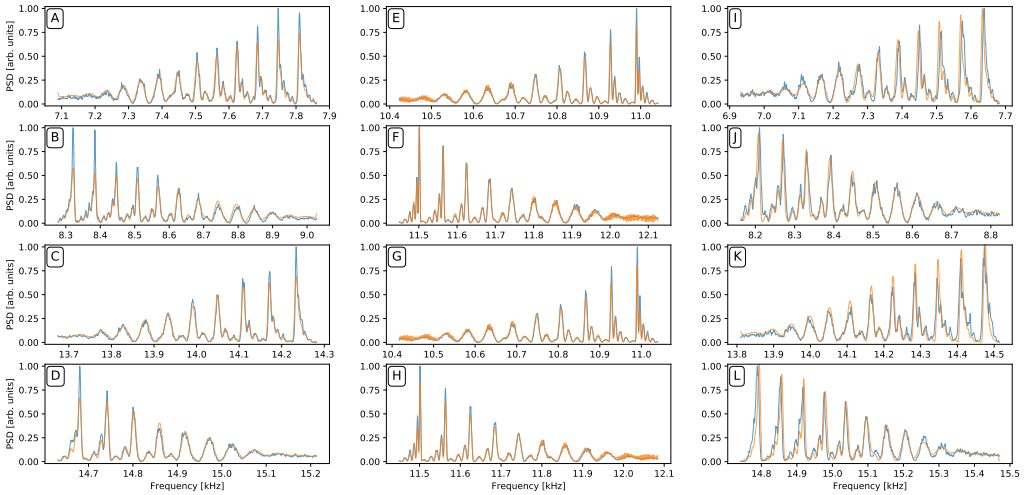

Figure 2.21: Acquired Schottky spectra compared with the result of the Scenario 2 fit.

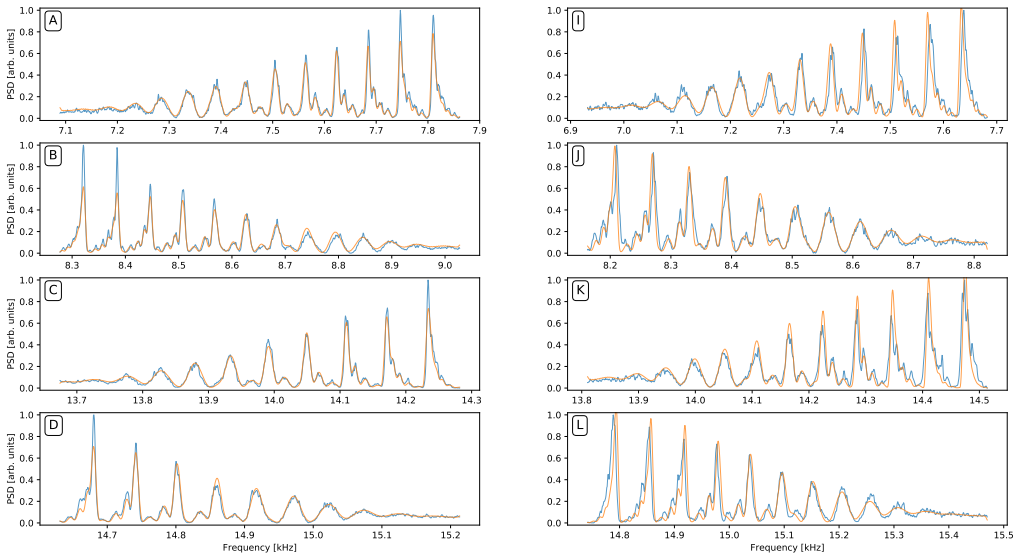

Figure 2.22: Acquired Schottky spectra compared with the result of the Scenario 3 fit.

For all scenarios and fills considered, the results of the chromaticity estimation are presented below. Each estimate is performed separately for each plane. For comparison, the chromaticity

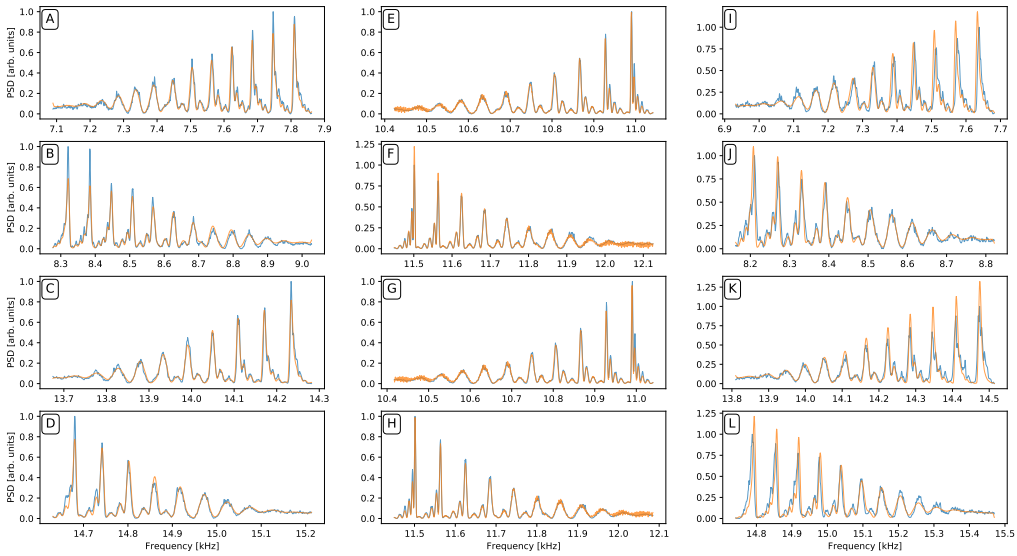

Figure 2.23: Acquired Schottky spectra compared with the result of the Scenario 4 fit.

calculated with the RF modulation technique is given. The analysed spectra were acquired before the start of the RF modulation to avoid the strong spectral distortions caused by the modulation. For that reason, only a fairly close-in-time comparison is possible, as seen from the x-axis of Figs. 2.24 to 2.26. However, it is important to note that during each time window presented in these plots there was no change in the current of the sextupole magnets, indicating that the values of chromaticity remained constant.

Analysing these plots, one may conclude that the results obtained with Scenarios 2-4 are self-consistent and strongly correlated with RF-modulation measurements. Chromaticity values calculated using Scenario 1 are less robust, as can be observed especially from the results of the fill 7486 horizontal and the fill 7435 vertical. Such a lack of robustness can be understood, for example, if one takes a look at Fig. 2.20 where the strong coherent peaks present in the vertical spectrum have to be included in the calculations, hence causing Eq. (2.19) to fail. The same problem was verified for the case of the fill 7486 horizontal. For Scenarios 2-4, as previously highlighted, one can exclude such distorted spectral regions and obtain better and plausible results.

The question remains of whether the accuracy of the chromaticity estimates is sufficient. The difference between the chromaticity value estimates provided by the proposed approaches and the RF modulation technique is sometimes greater than one unit. It is however important to note that the spread of the presented RF modulation results is not negligible and might cover several units.

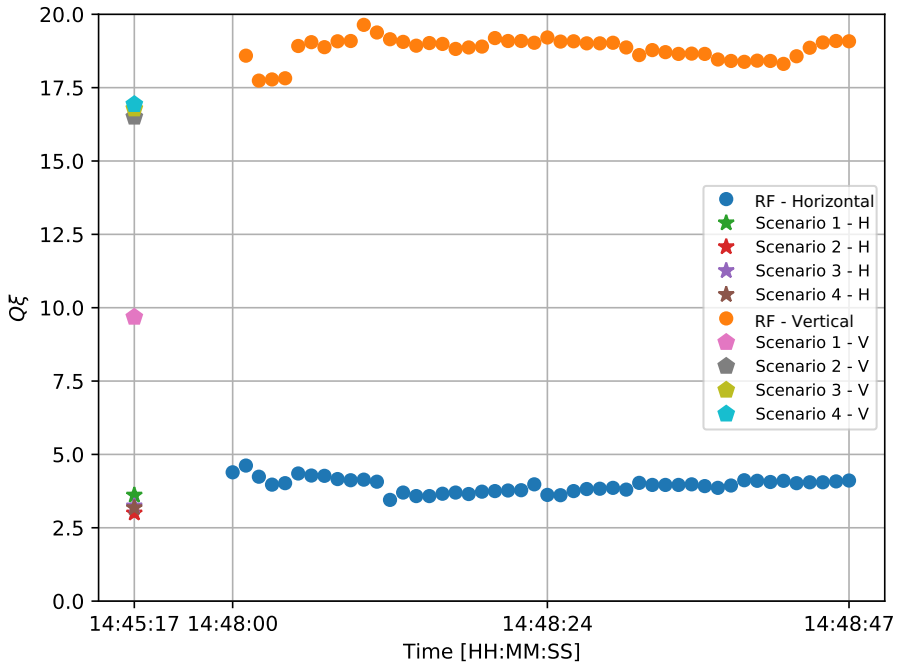

Figure 2.24: RF and Schottky-based chromaticity measurements during LHC fill 7435.

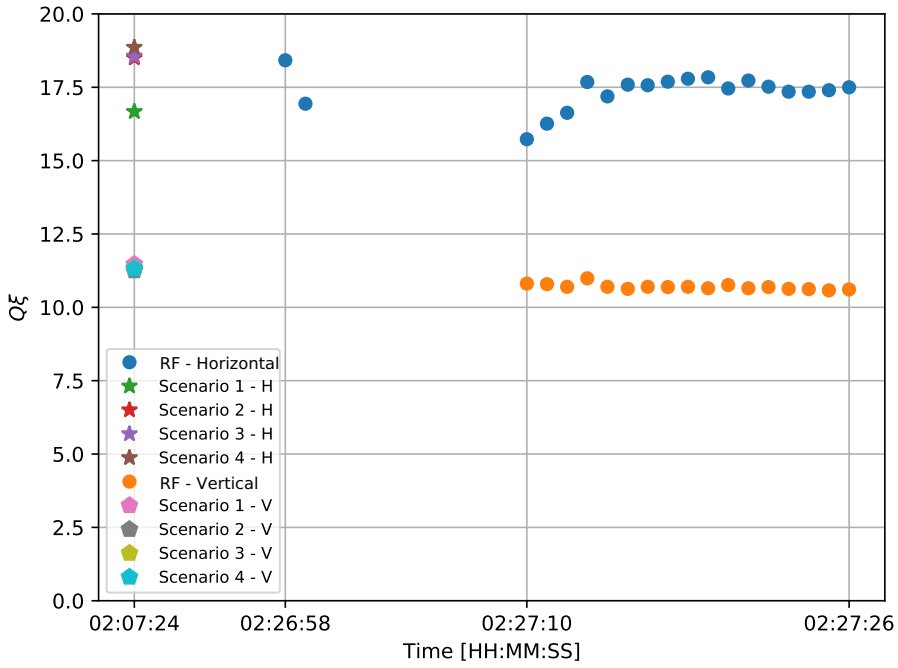

Figure 2.25: RF and Schottky-based chromaticity measurements during LHC fill 7443.

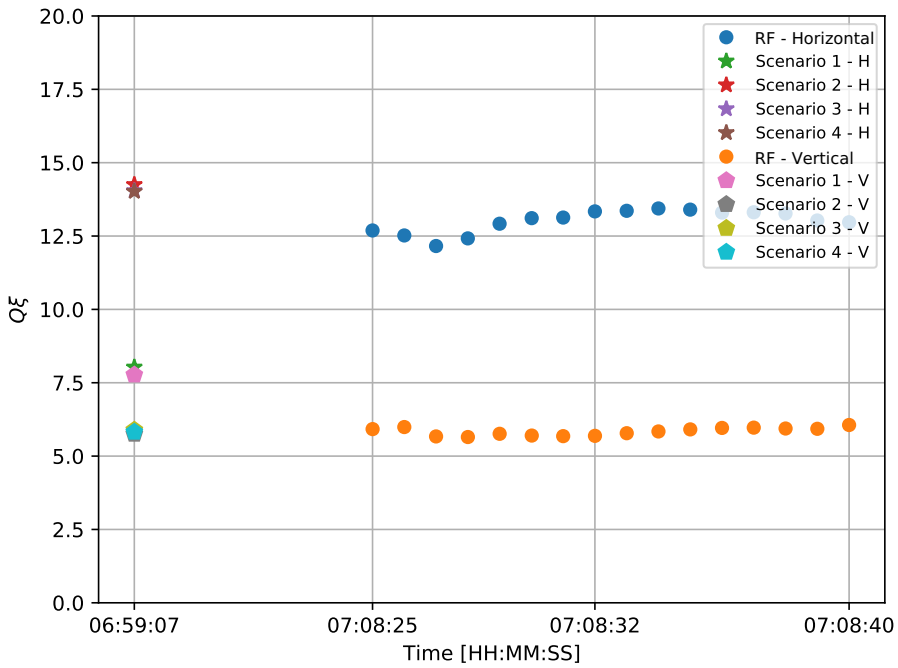

Figure 2.26: RF and Schottky-based chromaticity measurements during LHC fill 7486.

Taking this into account, the non-invasive methods presented here are shown to provide chromaticity estimates that are at least comparable to the ones obtained from the RF modulation technique.

To understand the limitations of the Schottky-based chromaticity estimation methods presented herein, one might try to assess the sensitivity of the spectrum itself with respect to chromaticity. Such an exercise is preliminarily illustrated in Fig. 2.27. It depicts four simulated spectra where the bunch profile and synchrotron frequency are constant and taken as the ones estimated for fill 7435, but the value of chromaticity varies. It is worth noting how subtle the changes in the spectrum are for different values of chromaticity and how challenging this distinction can be when dealing with real-life Schottky spectra.

One may also note, from Figs. 2.24 to 2.26, that the chromaticity estimates seem to be more precise for lower values of chromaticity. In Fig. 2.28 this observation is investigated in a more systematic manner. The distance between two simulated typical LHC spectra, different only in terms of their chromaticity, is expressed as a value of the cost function 2.26. One can see that the value of the cost function for the chromaticities, respectively, $Q\xi = 5$ and $Q\xi = 7$ is the same as the one for the spectra with the chromaticities $Q\xi = 15$ and $Q\xi = 18$. This observation, verified to hold for various types of LHC-like profiles, is not necessarily true for shorter bunches.

In all proposed scenarios, the value of betatron tune is calculated with the MD method, described

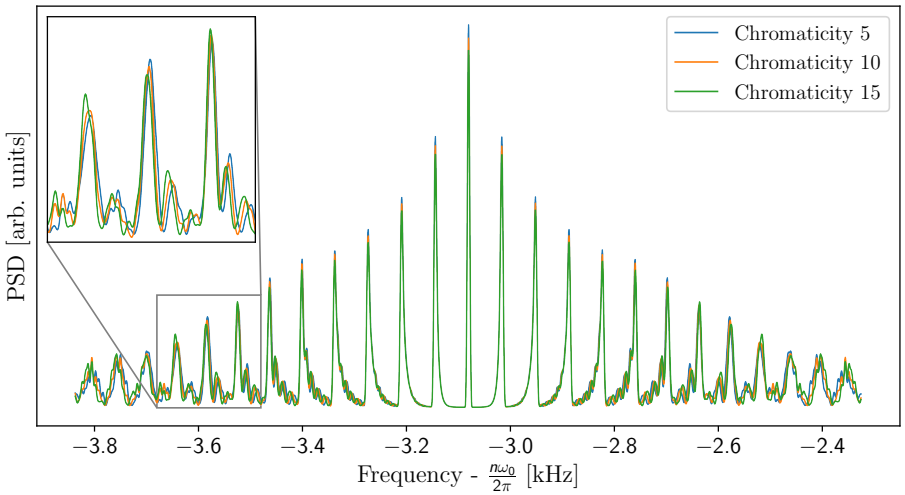

Figure 2.27: Simulated left transverse Schottky sideband for different values of chromaticity.

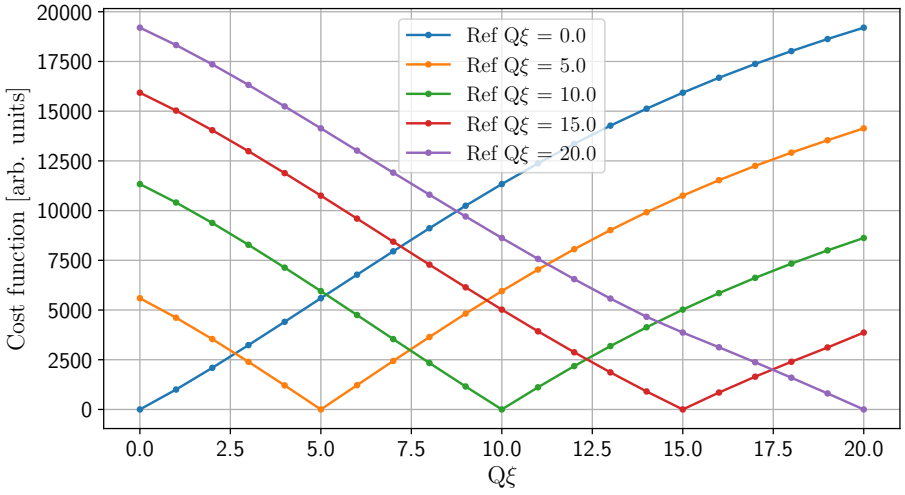

Figure 2.28: Difference between spectra of a typical LHC bunch as a function of chromaticity.

in subsection 2.3.2. The high precision of the method is confirmed by the fact that all fitted spectra are correctly reproducing the experimental ones. Any deviation would result in an evident misalignment. As a final sanity check, distributions of synchrotron amplitudes obtained by following Scenarios 2-4 might be compared. Such an example is shown in Fig. 2.29, confirming the self-consistency of the presented approaches.

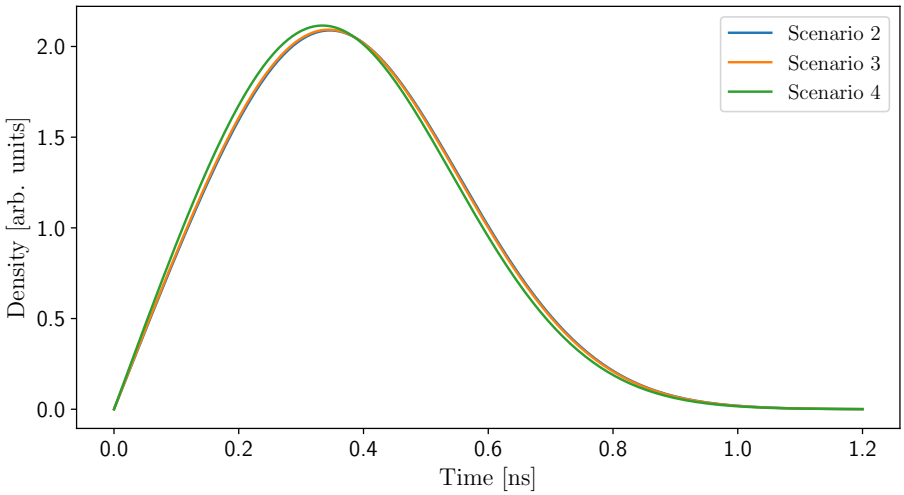

Figure 2.29: Estimated distribution of synchrotron amplitudes during LHC fill 7443.

2.4.3 Time Performance of Schottky Spectrum Fitting Procedures

Although Schottky fitting methods for the determination of longitudinal and transverse beam characteristics were proved to give reliable and accurate results, the question of their time efficiency remains. Contrary to the previous techniques of the Schottky signal analysis, the determination of correct beam parameters with a spectrum fitting procedure is based on the minimisation of a certain cost function using a time-consuming optimisation routine. This problem was investigated by two undergraduate students as a CERN Summer Students project, co-supervised by the author of this thesis. The purpose of this subsection is to report the conclusions of their work, fully described in Ref. [96, 97].

As explained at the beginning of Section 2.4, the current processing chain of the Schottky signal provides one new spectrum every second. For that reason, one second was set as an ultimate goal for the duration of the single-spectrum analysis. Nevertheless, even slower performance, in the order of a few tens of seconds, would not be considered disqualifying, since the quantity of highest interest, namely chromaticity, is not subject to rapid changes.

The time benchmarks were performed on a dedicated virtual machine equipped with 8 cores and

16 GB RAM. The algorithm was implemented with the Python programming language with the use of the Numba [98] library that translates Python routines into machine code using the LLVM compiler library [99]. Four different minimisation routines were compared: L-BFGS-B, Differential Evolution, TNC [100] and Powell method [101]. At a preliminary stage of comparison, the TNC and Powell method turned out to be less effective and disregarded in the detailed analysis.

The time efficiency of the L-BFGS-B and Differential Evolution algorithms was comprehensively tested on a set of real and artificially created Schottky spectra. For a single artificial noiseless spectrum, the average time needed by L-BFGS-B to converge was 83 seconds. This result significantly outperformed Differential Evolution runtime of 220 seconds. The situation changed when both routines were used for a sequential analysis of more than 300 real LHC Schottky spectra. This time run-time could have been improved by using the result of the previous fit as the starting guess for the next spectrum. Applying such a strategy, L-BFGS-B average runtime went down to 17.2 seconds, while Differential Evolution improved down to 7.9 seconds.

It is worth noting that the number of available cores limited the performance of Differential Evolution routines, but not L-BFGS-B. The L-BFGS-B method can be parallelised with the maximal number of used cores being equal to the number of fitted parameters plus one, contrary to the Differential Evolution algorithm which can work in parallel using an arbitrary number of cores. Given this restrictions it is promising that with a larger number of available cores, the ultimate goal of the runtime below one second could be achieved.

2.5 Improving Signal Quality by Bunch Gating

The purpose of this section is to revisit the theory of the Schottky signal with the aim of investigating the shape of the multi-bunch Schottky spectrum. It turns out that despite the apparent complexity of such a signal, it might be more suitable for analysis because of lower dynamic range requirements.

As previously mentioned, each LHC Schottky Monitor pickup consists of two slot-coupled symmetrically arranged at two opposite sides of the beam. As by design the difference signal is acquired, a large common mode intensity signal should, in principle, be highly reduced. Still, due to the system imperfection and common mode magnitude, the longitudinal Schottky sideband is present in the spectrum together with the dominant coherent central satellite. This imposes significant dynamic range requirements on the system, which could already have been observed in Fig. 2.12. As the ratio between the power of coherent and incoherent satellites scales with the total number of particles N, the problem is much more severe in the case of proton bunches, for which $N \approx 1.15 \cdot 10^{11}$, than lead ion bunches having $N \approx 7 \cdot 10^{7}$. In the case of proton runs, it is often the case that the dynamic range of the digitiser is not sufficient and the incoherent part of the spectrum is heavily distorted with noise, what is illustrated with Fig. 2.30. The irregular shape of the transverse sideband and extremely obscure internal Bessel satellite structure make the analysis of the spectrum practically impossible.

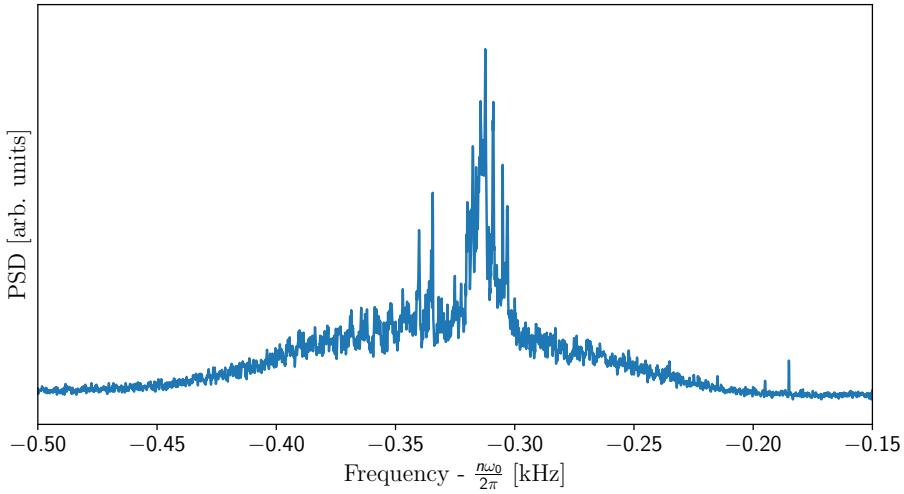

Figure 2.30: Typical spectrum obtained with LHC Schottky Monitor during proton run.

The LHC Schottky Monitor is equipped with a fast gate switch, which enables the observation of Schottky signals coming from a specific subset of all present bunches and changing this subset on the fly. In everyday operation, however, the gating system is set in a way to constantly observe

just one of the bunches. This simplifies the analysis, as due to impedance and inter-bunch effects, the nominal tunes of individual bunches can differ, as presented in Fig. 2.31 for the case of the baseline HL-LHC bunch filling pattern. The total predicted spread is in the order of $10^{-3} f_0$, what corresponds to 11 Hz, approximately half of the distance between the two following Bessel satellites of the Schottky spectrum at nominal LHC beam energy. Although the difference does not affect the longitudinal part of the Schottky spectrum, deriving any information from the transverse part would require additional post-processing or a cautious choice of gated bunches.

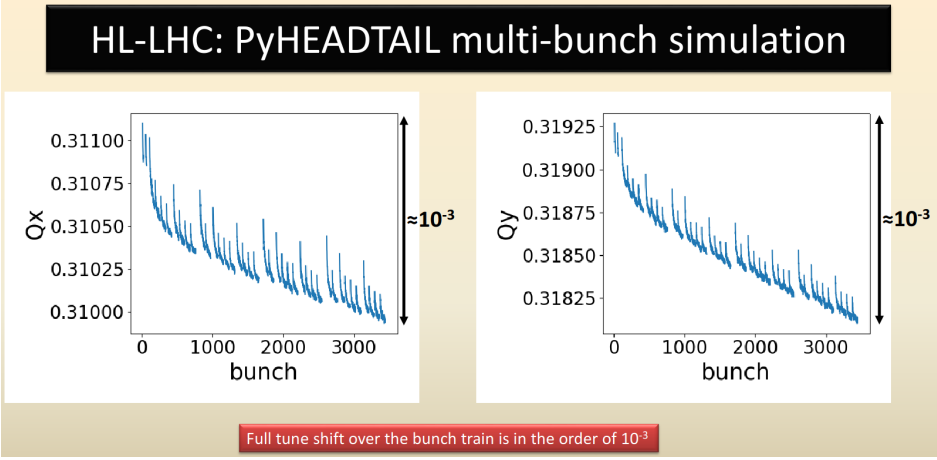

Figure 2.31: Spread of bunch betatron tune in HL-LHC baseline filling scheme [102].

In the following, a concept how the gating system might be used to reduce the magnitude of strong coherent central satellites will be proposed. Taking a closer look at the formula which describes the magnitude of the central longitudinal satellite in the case of a single bunch, given by Eq. (2.5), one reads

$$I^{(1)}(t) \propto \sum_{i=1}^{N^{(1)}} J_0\left(n\omega_0 \widehat{\tau}_i^{(1)}\right) e^{jn\omega_0 t},$$

where the superscript in $I^{(1)}(t)$ and $N^{(1)}$ is the number of particles in the bunch.

Now, assuming that the gating system accepts a signal coming from two distinct bunches, the second bunch intensity signal is given by

$$I^{(2)}(t) \propto \sum_{i=1}^{N^{(2)}} J_0\left(n\omega_0 \widehat{\tau}_i^{(2)}\right) e^{jn\omega_0 (t+\Delta t)},$$

where Δt is a time offset between the passage of the bunches through the pickup. The total intensity

signal $I^{Total}(t)$ around the central satellite of the n-th Schottky harmonic will there be given by

$$I^{Total}(t) = I^{(1)}(t) + I^{(2)}(t) \propto \sum_{i=1}^{N^{(1)}} J_0\left(n\omega_0 \widehat{\tau}_i^{(1)}\right) e^{jn\omega_0 t} + \sum_{i=1}^{N^{(2)}} J_0\left(n\omega_0 \widehat{\tau}_i^{(2)}\right) e^{jn\omega_0 (t+\Delta t)}.$$

If one assumes now that the second bunch is the exact copy of the first one, both in terms of their intensity and synchrotron amplitude distributions, the above equation simplifies to

$$I^{Total}(t) = I^{(1)}(t) + I^{(2)}(t) \propto \left(\sum_{i=1}^{N} J_0\left(n\omega_0 \widehat{\tau}_i\right) e^{jn\omega_0 t}\right) \cdot \left(1 + e^{jn\omega_0 \Delta t}\right). \tag{2.30}$$

To proceed, it is necessary to investigate the possible values of the time offset Δt. In principle, it can be easily evaluated by dividing the angular distance between the bunches by their revolution frequency. As a consequence of the RF acceleration, particle bunches are not randomly spaced along the circumference of the machine, but must be located in one of the RF-buckets, whose number and size depend on the value of RF frequency. To be precise, if $\omega_{RF} = h\omega_0$, one gets exactly h equally distributed RF buckets. If the first bunch is set to be in the bucket 0 and the second in the bucket k, one has

$$\Delta t = \frac{k \cdot 2\pi}{h} \cdot \frac{1}{\omega_0}.$$

Plugging it into Eq. (2.30) one obtains:

$$I^{Total}(t) \propto \left(\sum_{i=1}^{N} J_0\left(n\omega_0 \widehat{\tau}_i\right) e^{jn\omega_0 t}\right) \cdot \left(1 + e^{2jnk\pi/h}\right). \tag{2.31}$$

It follows that the intensity signals of two bunches add up constructively or destructively, depending on the product of the relative bucket number k and Schottky harmonic n. The same does not hold for any satellite other than the central one. This is due to the $e^{jp\varphi_{s_i}}$ term in Eq. (2.5), which introduces randomness to the phases of the intensity of individual particles. The summation in Eq. (2.31) is fully destructive if $e^{2jnk\pi/h} = -1$, or equivalently:

$$\frac{2nk\pi}{h} = 2m\pi + \pi,$$

where m is an integer. One may rewrite this condition in a form

$$2nk = 2hm + h \quad \Longleftrightarrow \quad 2nk - h = 2hm,$$

or equivalently

$$2h \mid (2nk - h),$$

which means that $2h$ divides $(2nk - h)$. An instant conclusion is that h needs to be even; otherwise $(2nk - h)$ would be an odd number, which cannot have an even divisor $2h$. Then one can take $g := \frac{h}{2}$ and write

$$h \mid (nk - g).$$

The above form is a definition of the mathematical relation of congruence, denoted in the following way:

$$nk \equiv g \pmod{h}. \tag{2.32}$$

The theory of congruences is treated in detail in Ref. [103]. In the following, only a few elementary properties shall be used, the first of which describes how both sides of a congruence can be divided:

$$a \cdot d \equiv b \cdot d \pmod{c} \iff a \equiv b \left(\mathrm{mod} \frac{c}{GCD(c,d)}\right),$$

where $GCD(c,d)$ is the greatest common divisor of numbers c and d. Using this property, one can deduce that Eq. (2.32) implies

$$\frac{nk}{GCD(n,g)} \equiv \frac{g}{GCD(n,g)} \quad \left(\mathrm{mod}\ \frac{h}{GCD(n,g)}\right), \tag{2.33}$$

because $GCD(h, GCD(n,g)) = GCD(n,g)$. Linear congruence of the form

$$ax \equiv b \pmod{c}$$

has an integer solution x if and only if

$$GCD(c,a) \mid b.$$

It follows that one can find an integer k fulfilling Eq. (2.33) if and only if

$$GCD(\frac{n}{GCD(n,g)}, \frac{h}{GCD(n,g)}) \mid \frac{g}{GCD(n,g)} \iff GCD(n,h) \mid g, \tag{2.34}$$

which, given the fact that $g := \frac{h}{2}$, means that n cannot be an integer multiple of h. The potential solution will not be unique, as if k is the smallest positive solution of Eq. (2.33), then for every

integer m a number

$$k' = k + m \cdot \frac{h}{GCD(n, g)} \tag{2.35}$$

is a solution as well. As the value of k is limited by the number of RF buckets h, one can conclude that m can take values between 0 and $GCD(n, g) - 1$, and one has exactly $GCD(n, g)$ distinct solutions within this range. The initial, smallest positive solution of Eq. (2.33) can be easily found by the trial-and-error method.

In the case of the LHC Schottky Monitor, one has[6] $h = 3564$ and $n = 427725$. As

$$GCD(n, g) = GCD(427725, 1782) = 9,$$

equation 2.33 takes a form

$$47525k \equiv 198 \pmod{396}$$

and has nine distinct solutions for $k \in ([0, 3564)$:

$$k = 198,\ 594,\ 990,\ 1386,\ 1782,\ 2178,\ 2574,\ 2970,\ 3366.$$

It means that gating the LHC Schottky Monitor on two identical bunches which are 198 buckets apart, would result in the complete suppression of the central longitudinal satellite.

For practical applications, it is desirable that two summed signals have similar properties, especially with respect to their transverse characteristics. As was seen in Fig. 2.31, such a similarity is most likely obtained between bunches which are spatially close. For that reason, a change of the LHC Schottky Monitor working frequency could be considered. As Eq. (2.35) suggests, the smallest distances can be obtained if $GCD(n, 1782)$ is large. For $n = 427761$, harmonic distant from the nominal one by approximately 405 kHz, one has $GCD(427761, 1782) = 81$ and the smallest positive solution of Eq. (2.33) is given by $k = 22$.

In reality, distinct bunches do not have exactly equal intensities, nor their profiles are identical. For that reason, the total intensity signal at the central harmonic, given by Eq. (2.30), will not perfectly cancel. Nevertheless, for two bunches spatially separated as described above, having, respectively, $N^{(1)}$ and N^2 particles, the central satellite component of the cumulative intensity signal would have a power proportional to $(N^{(1)} - N^{(2)})^2$, which for comparable bunches is significantly less than $(N^1)^2$ and $(N^2)^2$, the proportionality terms in the case of the single bunch gating. Meanwhile, the power of the incoherent part of the spectrum is proportional to the total number of particles,

6. Actually, the LHC RF system operates at frequency $\omega_{RF} = 35640\ \omega_0$, but only one per ten buckets is populated

regardless of the gating scheme.

The presented idea of cancelling the central longitudinal satellite by summing the Schottky signal of multiple bunches is not new, as it has been previously discussed in Ref. [104]. The effect has been, however, addressed here from a slightly different perspective. In the cited article, the Schottky system was acquiring the signal coming from all the bunches, evenly distributed along the accelerator ring. In such a configuration, the central longitudinal satellite is present only at these harmonics of the revolution frequency, which are also the harmonics of the RF frequency. This can be verified by adding additional terms in the second parentheses of Eq. (2.31). One can also note that these harmonics are exactly the ones that have been excluded in the presented derivation by the condition within (2.34). Here, a criterion is given on how to select only two bunches in order to suppress the coherent component at a given harmonic of the revolution frequency. In the case of LHC it is a vital development, as the magnitude of the longitudinal central satellite is a major obstacle to proton beam Schottky signal analysis. Moreover, the same theory can also be applied to any Schottky monitor capable of arbitrary bunch gating.

2.6 Summary

The first part of this dissertation was devoted to a non-invasive technique of beam diagnostics based on the analysis of the Schottky spectrum. The chapter has begun with a presentation of the bunched Schottky signal theory and detailed derivations of the final formulae for the longitudinal and transverse Schottky signals, formulae Eq. (2.6) and Eq. (2.15). Apart from serving as a starting point for further considerations, the aim of this part was to systematise and refresh the theory, commonly presented only in the form of partial results or using obsolete terminology.

Subsequently, the well-known formula relating the chromaticity to the RMS widths of the transverse Schottky sidebands was formally proven in the case of a bunched beam. This derivation has been missing so far in the literature and constitutes one of the most important theoretical results included in this thesis. To date, the formula has been used for the chromaticity estimation at the LHC, although its applicability turned out to be limited only to signals of very high quality.

In the next part of the chapter, a new technique for the analysis of Schottky signals was proposed. It was shown that in the absence of intra-bunch coherent motion, the distribution of synchrotron amplitudes among all the particles in a bunch and the corresponding longitudinal Schottky spectrum are related through a system of linear equations. The coefficients of these equations depend only on the nominal synchrotron frequency, betatron tune and chromaticity. All these beam characteristics can be determined with the help of optimisation algorithms such that this linear model fits the measured Schottky spectrum. In addition, a new algorithm for Schottky-based tune estimation was developed.

The thesis reports on the experimental verification of newly developed techniques. All proposed diagnostic approaches have been tested using LHC Run 2 data and benchmarked against the readouts of alternative, but not necessarily non-invasive instruments. This verification indicated the accuracy and high precision of the postulated techniques.

The last part of the chapter addressed the practical problem of the central longitudinal satellite domination of the Schottky spectrum. As a result, in the case of the proton beam, the incoherent spectrum, which contains the most of the information on the beam characteristics, cannot be easily separated from the noise. A solution to this issue was proposed, based on the fact that contributions to the Schottky signal from two distinct bunches can add up destructively at the central satellite. Following principles of number theory, the conditions for destructive interference were provided.

Preliminary studies on the method's time efficiency have been reported within this chapter. The design of an online implementation of the methods described herein is currently underway with the purpose of providing the LHC operators with either continuous or on-demand measurements.

CHAPTER 3
CHERENKOV DIFFRACTION RADIATION

3.1 Introduction

The radiation produced by charged particles moving in a dielectric medium at relativistic velocities had been systematically studied since 1934 in a series of experiments performed by Cherenkov and Vavilov [105]. It was observed, as sketched in Fig. 3.1, that a particle emits radiation if the condition $n\beta > 1$ is fulfilled, where n is the refractive index of a given medium and $\beta = \frac{v_p}{c}$ is the ratio of the particle's velocity and the speed of light in vacuum. The emitted light waves form a conical front, with a generatrix at an angle $\theta = \arccos\frac{1}{n\beta}$ with the trajectory of the particle. Analysing these observations, Frank and Tamm formulated a theoretical explanation of this phenomenon based on classical electrodynamics [106]. According to their results, the spectrum of the radiated energy is continuous and can be given in a simple form, often referred to as the Frank and Tamm (F-T) formula. Due to its properties, especially the dependence of the emission angle on the particle's velocity, Cherenkov radiation turned out to be a very convenient tool for particle detection. Until today, Ring-imaging Cherenkov (RICH) [46] and Detection of Internally Reflected Cherenkov light (DIRC) [47] systems are standard components of particle physics experiments. As a recognition of their achievement, Cherenkov, Tamm and Frank were awarded the Nobel prize in 1958.

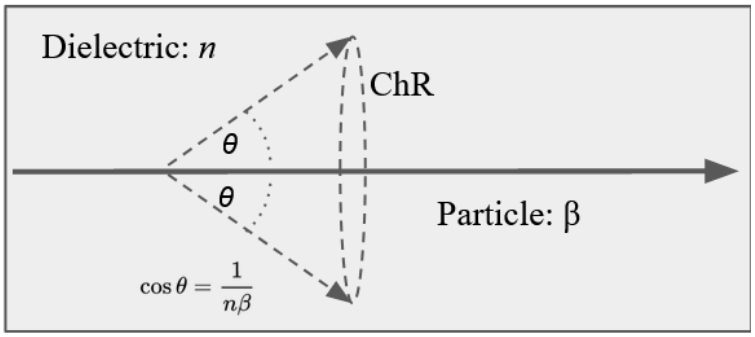

Figure 3.1: Sketch of Cherenkov Radiation emission.

A decade after the discovery of Cherenkov radiation, Ginzburg and Frank studied theoretically the radiation emitted by a particle moving not inside the medium, but along the axis of an infinitely long evacuated tunnel, surrounded by a dielectric medium [107]. During the following decades, Linhart [108] and Ulrich [109] described a similar effect associated with a particle moving parallel to the surface of a dielectric half-space. These two are the initial examples of *Cherenkov Diffraction Radiation* (ChDR), depicted in Fig. 3.2, which describes the radiation of a charged particle passing

in the close vicinity of a dielectric medium. This type of radiation shares many similarities with the standard Cherenkov radiation, such as the angle of the radiation's propagation can be calculated using the same formula. On the other hand, the *Impact parameter*, distance between the particle's trajectory and the surface of the dielectric medium, denoted in Fig. 3.2 by the letter h, has a fundamental impact on the spectral distribution of the radiated energy. The term *radiator* is frequently used to denote the dielectric medium in which the radiation is emitted, and so it will be used in the scope of this thesis.

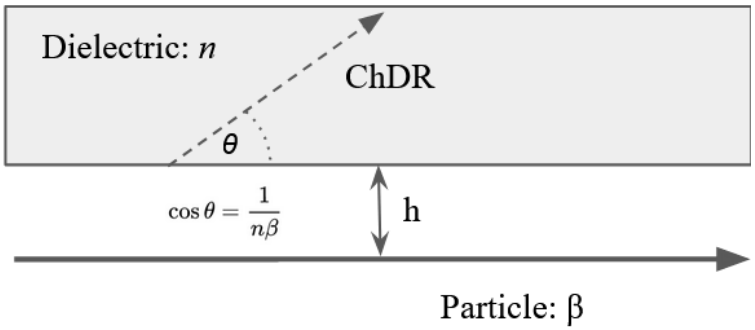

Figure 3.2: Sketch of Cherenkov Diffraction Radiation.

Recently, the possibilities that ChDR brings to non-invasive beam monitoring have been extensively investigated [56]. The properties of ChDR are well aligned with the requirements of diagnostics. The interaction with the radiator has a negligible impact on high-energy beams. Contrary to synchrotron radiation and diffraction radiation, ChDR is emitted at a large and well-defined angle, which facilitates the signal acquisition and reduces radiation hardness requirements. Finally, the design of a ChDR detection system is relatively simple and would be a promising candidate for diagnostic systems embedded in novel accelerator structures, such as dielectric laser accelerators or plasma wakefield accelerators.

Up until now, ChDR has not yet been used in any operational diagnostic system. Preliminary studies at CERN's CLEAR facility include designs of beam position monitors [110] and bunch length monitors [111] based on coherent radiation from short bunches. The beam position is measured based on comparing the intensity of radiation induced in two, preferably identical radiators, placed on opposite sides of the beam. Deriving the position from the incoherent radiation would follow the same principle, but the problem of low radiation intensity would need to be addressed by the means of either extending the length of the radiator or summing up the signal coming from many consecutive bunches.

It has been shown that the bunch length can be derived from the coherent part of the spectrum, or more precisely from the spectral region in which the coherence is already slightly reduced. Mea-

suring the relative radiation intensity at distinct frequency bands, located in the coherent-incoherent transition region allows one to estimate the longitudinal bunch profile. Depending on the general shape of the bunch profile, which must be known *apriori*, the number of observed frequency bands corresponds to the number of parameters of the bunch profile. As an example, the determination of a Gaussian-known bunch profile, parameterized with a single parameter, requires measurement at two distinct frequencies, as presented in [111].

In addition, several accelerator facilities around the world have confirmed the feasibility of observing ChDR. Incoherent ChDR has been observed for the first time in the Cornell electron-positron storage ring, emitted by a 5.3 GeV positron and a 2.1 GeV electron beam [112, 113]. During this study another advantage of ChDR was demonstrated; the signal coming from two counter-propagating beams could be easily separated due to the opposite propagation angles. Another synchrotron at which incoherent ChDR was observed is the Diamond Light Source [114]. Studies on the coherent ChDR were also conducted in the CLARA [115] and t-ACTS [116] facilities.

3.2 Theory of Cherenkov Diffraction Radiation

Any application of Cherenkov diffraction radiation requires prior knowledge of the expected characteristics of the emitted radiation. Since the exact solutions of the electromagnetic problem are often not known, and detailed computer simulations require extensive time and resources, preliminary properties of the radiation are derived from simplified models, which take special assumptions on the radiator shape.

The first group of models can be labelled *Stationary Models*. Their name comes from the assumption of longitudinal infiniteness and uniformity of the radiator. The problem is called *stationary*, as it is invariant on the temporal and longitudinal translations. Although such models will clearly be not suitable in the cases when wavelength of the studied radiation is comparable to the radiator size, for real case applications they might serve as a good approximation for the visible, ultraviolet and X-ray radiation. A series of studies [117–121] uses predictions of these models for the initial radiation yield, which is then modified based on the specific geometry of the radiator following the optical principles.

Alternatively, one might put limitations on the longitudinal size of the radiator already at the stage of calculation of the initial radiation yield. This limitation features another group of approaches, namely *Non-Stationary Models*. They include additional edge effects, such as diffraction radiation and transition radiation [122]. In the case of short radiators these effects naturally dominate the total radiation yield, but surprisingly non-stationary ChDR predictions differ from the stationary results even for arbitrarily long radiators.

In the scope of this section the main results of the few commonly used Stationary and Non-Stationary models will be described. Then, a discussion on differences between single particle and particle bunch radiation will be presented, including characterisation of the so-called *coherent* and *incoherent* frequency regimes.

3.2.1 Stationary Models

As a fundamental stationary model one can take Frank and Tamm's theoretical explanation of the Cherenkov radiation phenomenon. A point charge q was considered, moving with a uniform velocity v through the unbounded medium with a frequency dependent permittivity $\epsilon(\omega) = n^2(\omega)$ and permeability $\mu(\omega)$. Derived formula for radiation's spectral distribution states:

$$\frac{d^2E}{dx\,d\omega} = \frac{q^2}{4\pi}\mu(\omega)\omega\left(1 - \frac{1}{\beta^2 n^2(\omega)}\right), \tag{3.1}$$

which means that the radiation yield is proportional to the considered frequency if one assumes a nondispersive medium such that $n > \beta^{-1} = \frac{c}{v}$. Although this case is not an example of Cherenkov Diffraction Radiation, it will serve as a reference to the further obtained results.

During the defense of the doctoral dissertation of P. Cherenkov, L. Mandelstam posed the problem of a charge moving along the axis of an infinitely long vacuum cylinder, surrounded by an infinitely thick layer of dielectric medium (Fig. 3.3). This situation was firstly analysed by Ginzburg and Frank, followed by numerous variations of the problem studied, e.g. in Ref. [123, 124].

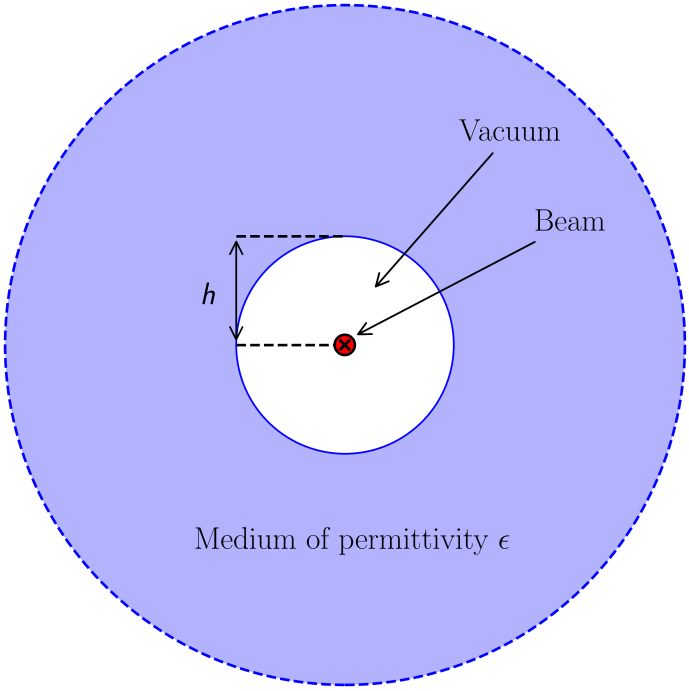

Figure 3.3: Sketch of a simple cylindrical ChDR geometry.

In this case, in addition to the velocity of the particle and the dielectric characteristics, the radius h of the vacuum tunnel has a profound impact. According to the result obtained by Olsen in Ref. [124], the shape of the spectral distribution of the radiated energy is given by

$$\frac{d^2E}{dx\,d\omega} = \frac{q^2}{4\pi}\Re\left(\mu(\omega)\omega\left(1 - \frac{c^2}{v^2n^2(\omega)}\right)j\alpha(\omega)\right), \tag{3.2}$$

where

$$\alpha(\omega) = \frac{Bk_1K_1(k_1h)K_0(k_2h) - k_2K_0(k_1h)K_1(k_2h)}{Bk_1I_1(k_1h)K_0(k_2h) + k_2I_0(k_1h)K_1(k_2h)}$$

and

$$B = \frac{k_2^2 \epsilon_0}{k_1^2 \epsilon}, \quad k_1 = \frac{\omega}{v\gamma}, \quad k_2 = \frac{\omega}{v}\sqrt{1 - \epsilon(\omega)\mu(\omega)\beta^2}.$$

In the equations above, I_i and K_i denote the modified Bessel functions of the first and second kind and order i, while γ denotes the relativistic Lorentz factor. For brevity, in the scope of this thesis, the cylindrical geometry described with Eq. (3.2) will be referred to as *Olsen model*.

Another important example of a stationary model is a case of a charge travelling with a uniform velocity in parallel to the surface of a dielectric half-space. The distance between the particle trajectory and the surface of the radiator is constant and equal to h, as presented in Fig. 3.4

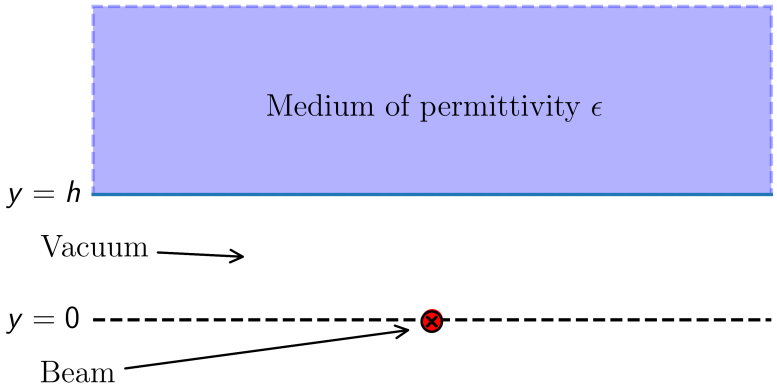

Figure 3.4: Sketch of a simple flat ChDR geometry.

The total energy radiated inside the dielectric, together with its angular distribution and polarisation, was investigated in detail by many authors [108, 109, 125]. In the simplest case, when $\mu(\omega) \equiv \mu_0$, the spectral distribution of the energy radiated along the unit distance takes the following form, obtained in Ref. [109] by Ulrich:

$$\begin{aligned}\frac{d^2E}{dx\,d\omega} =& \frac{q^2}{4\pi}\mu_0\omega\frac{\epsilon\beta^2 - 1}{\epsilon - 1}\times \\ &\times \int_{-\frac{\pi}{2}}^{\frac{\pi}{2}} d\phi \left(\frac{(\epsilon+1)(\epsilon\beta^2-1)\sin^2\phi + \epsilon(1-\beta^2)}{(\epsilon+1)(\epsilon\beta^2-1)\cos^2\phi - \epsilon^2\beta^2} \cdot \cos^2\phi \cdot e^{-2h\frac{\omega}{v}\sqrt{(\epsilon\beta^2-1)\sin^2\phi + 1 - \beta^2}} \right).\end{aligned} \tag{3.3}$$

For brevity, in the scope of this thesis, the described flat geometry and Eq. (3.3) will be referred to as *Ulrich model*.

Equations (3.2) and (3.3) are complicated and rather difficult to analyse. For this reason, an illustrative spectral distribution of the energy radiated by a 200 MeV electron is depicted in Fig. 3.5. The particle is moving in 1 cm distance from the radiator for which we have $\epsilon = 2.1, \mu = \mu_0$. Such values correspond to the microwave properties of Politetrafluoroetylen (PTFE, teflon), but here for simplicity we assume that permittivity and permeability are constant for all frequencies. As a reference, a distribution of Cherenkov radiation emitted by a particle moving directly inside the medium is given.

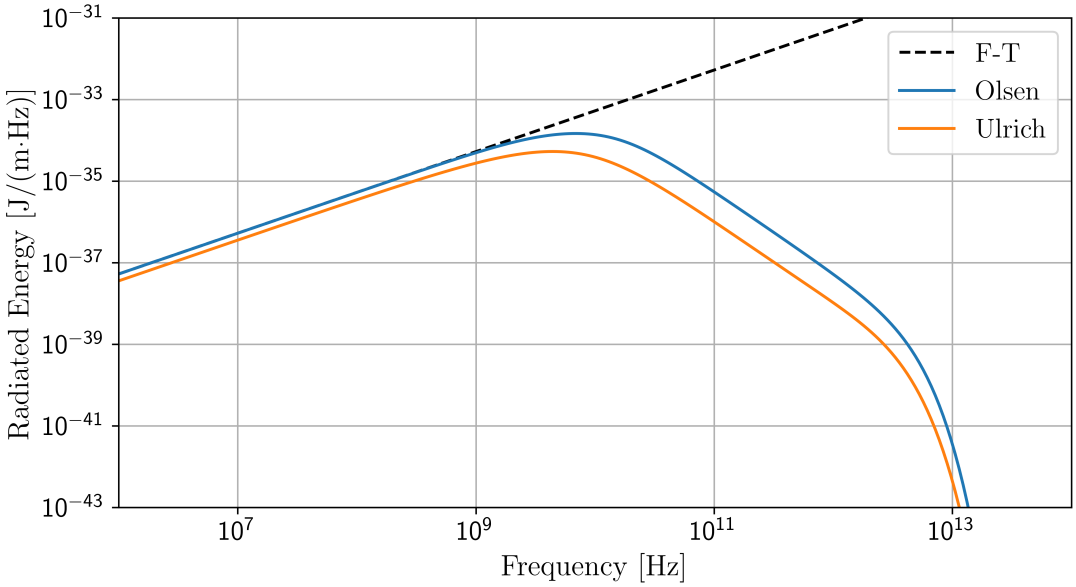

Figure 3.5: Spectral distribution of ChDR as predicted by stationary models.

As can be seen, within the spectral distributions of stationary ChDR we can distinguish three frequency regimes. In the low-frequency limit, the distribution resembles the distribution of Cherenkov radiation as predicted by Eq. (3.1), the F-T formula. Then, for intermediate frequencies, the density of radiated energy decreases proportionally to the square of frequency. Finally, in the last frequency regime the density falls abruptly. In Section 3.3 the border frequencies of each regime will be investigated in detail. Broadly speaking, the spectral distribution of energy radiated in flat and circular geometry differs only quantitatively while remains in qualitative agreement.

3.2.2 Non-Stationary Models

A notable example of a non-stationary model is the Polarisation Current Approach (PCA) [122], which unifies Cherenkov diffraction radiation together with diffraction radiation, transition radiation and Smith-Purcell radiation as instances of a general *Polarisation Radiation* [126]. According to this

approach, the radiation yield in each of these cases can be calculated based on the determination of *polarization current*, induced on a surface of the dielectric medium by a charged particle passing close to it. The current is the actual physical origin of the radiation, and if inserted into the Maxwell equations, the magnetic field of the radiation emitted within the dielectric volume V_T is given by

$$\boldsymbol{H}^{pol}(\boldsymbol{r},\omega) = \nabla \times \frac{1}{c}\int_{V_T} \boldsymbol{j}^{(0)pol}(\boldsymbol{r}',\omega)\frac{e^{j\sqrt{\epsilon}\frac{\omega}{c}|\boldsymbol{r}-\boldsymbol{r'}|}}{|\boldsymbol{r}-\boldsymbol{r'}|}d^3\boldsymbol{r'}, \tag{3.4}$$

where $\boldsymbol{j}^{(0)pol}(\boldsymbol{r}',\omega) = \sigma(\omega)E_0(\boldsymbol{r}',\omega)$ denotes the density of the polarisation current, which is induced by the Coulomb field of the passing charged particle, $\sigma(\omega) = (\epsilon - 1)\frac{\omega}{4\pi j}$ is the conductivity of the medium and $E_0(\boldsymbol{r}',\omega)$ is the direct Coulomb field of the charged particle.

A typical geometry considered in the PCA is presented in Fig. 3.6. It assumes V_T to be an infinitely thick and wide, but finitely long, flat radiator, and a point charge q travelling parallel to the surface of the radiator with velocity $v = \beta c$.

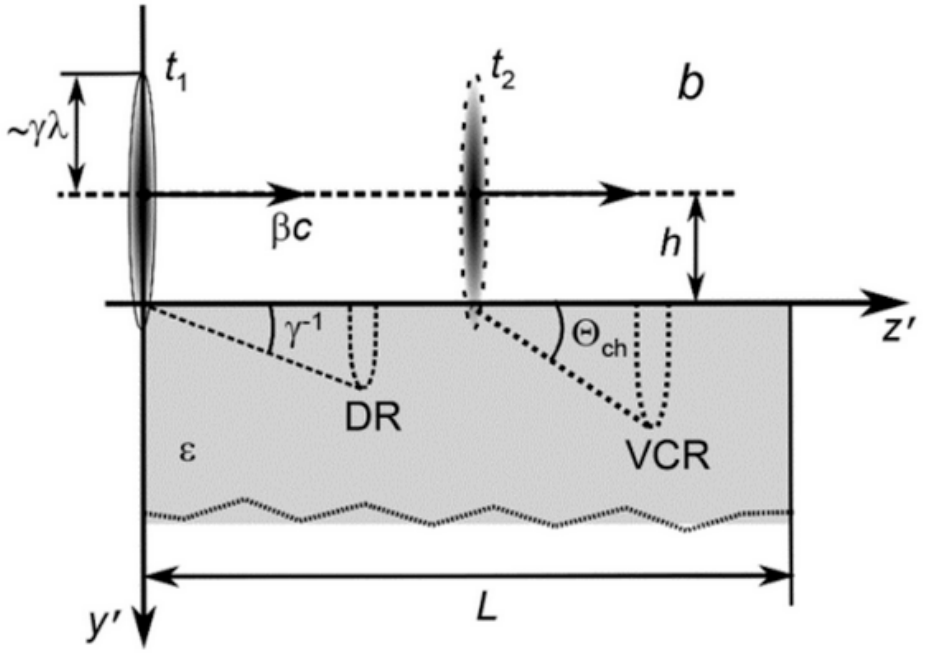

Figure 3.6: Sketch of a geometry described by the PCA model [127].

According to the result obtained in Ref. [128], Eq. (3.4) takes the following form in the wave

zone:

$$\boldsymbol{H}^{pol}(\boldsymbol{r},\omega) = \\ -\frac{q\beta\gamma}{4\pi c}\frac{e^{j\sqrt{\epsilon}\frac{\omega}{c}r}}{r}\frac{\sqrt{\epsilon}(\epsilon-1)}{\sqrt{1+\epsilon(\beta\gamma n_x)^2}}\frac{\xi\exp\left(-h\frac{\omega}{\beta\gamma c}\sqrt{1+\epsilon(\beta\gamma n_x)^2}\right)}{\left(\sqrt{1+\epsilon(\beta\gamma n_x)^2}+j\beta\gamma\sqrt{\epsilon}n_y\right)}\frac{\left[\exp\left(jL\frac{\omega}{c\beta}\left(1-\sqrt{\epsilon}n_z\beta\right)\right)-1\right]}{\left(1-\sqrt{\epsilon}n_z\beta\right)},$$

where $\boldsymbol{n}$ is a unit vector in the direction of $\boldsymbol{r}$ and

$$\xi = \begin{pmatrix} \gamma^{-1}n_y - jn_z\sqrt{1+\epsilon(\beta\gamma n_x)^2} \\ n_x\left(\sqrt{\epsilon}\beta\gamma n_z - \gamma^{-1}\right) \\ n_x\left(j\sqrt{1+\epsilon(\beta\gamma n_x)^2} - \sqrt{\epsilon}\beta\gamma n_y\right) \end{pmatrix}.$$

The angular and spectral densities of the energy radiated inside the dielectric medium can then be calculated as

$$\frac{d^2E}{d\omega d\Omega} = \frac{cr^2}{|\sqrt{\epsilon}|^2}\left|\boldsymbol{H}^{pol}(\boldsymbol{r},\omega)\right|^2. \tag{3.5}$$

For the same parameters as in the case of the stationary models, one can calculate the spectrum of energy radiated in the form of ChDR by integrating Eq. (3.5) over the whole angular range. The results of such calculations are presented in Fig. 3.7 for the same parameters as in the case of stationary model, Fig. 3.5. A very long 10^3 m radiator was used in the calculations to minimise the contribution of Diffraction Radiation, but the emitted energy was then scaled down to a particle path of 1 metre.

Similarly as in the case of stationary models, the spectral distribution of the energy radiated according to PCA can be divided into three regions, each expressing a different dependence of the radiation yield on the frequency.

At this point, it is worth underlining a few important facts related to Eq. (3.5). Primarily, it describes the field within the dielectric, before it transmits out of it and, therefore, does not include yet any effects of refraction or transmittance. However, this is sufficient for an approximate estimation of the level of radiated energy. Numerous detailed, PCA-based radiator shape-specific results are given in Ref. [122]. In addition, Eq. (3.5) describes not only ChDR, but actually a mixture of ChDR and DR. Fortunately, as can be seen in Fig. 3.8, for $L \gg \lambda$ the ChDR component dominates, as it scales with the length of the radiator. In addition, both components are well separated in the azimuthal angle range and can be easily distinguished. If the radiator is not sufficiently long, both components interfere or the DR component completely dominates the distribution.

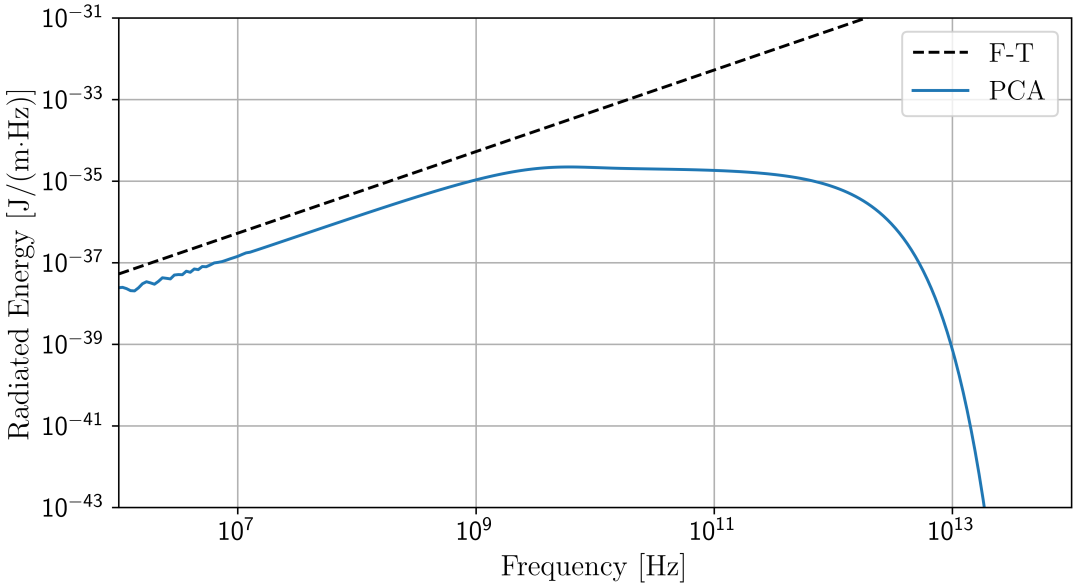

Figure 3.7: Spectral distribution of ChDR as predicted by PCA.

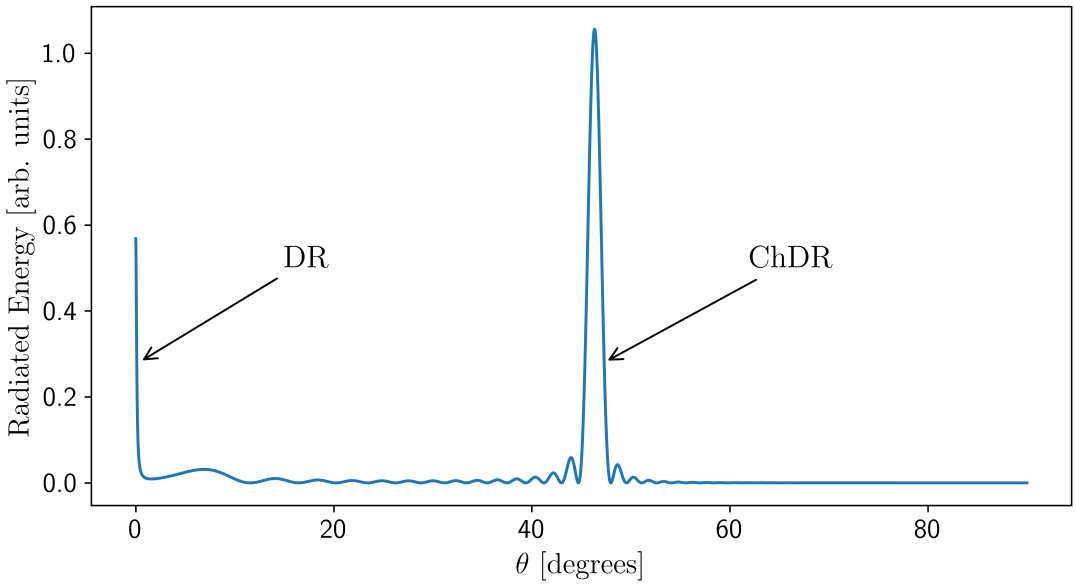

Figure 3.8: Azimuthal distributions of 10 GHz ChDR and DR as described by PCA in the case of 1 m long PTFE radiator.

3.2.3 ChDR of a Particle Bunch

Equations (3.2), (3.3) and (3.5) describe the spectral distribution of the energy radiated by a single charge. The situation is more complex when one considers the radiation generated by the

whole particle bunch. Individual particle contributions might add up constructively or destructively, depending on the considered radiation wavelength and distance between the particles. In this subsection, the theory of coherent and incoherent radiation is recalled, following the approach presented in Ref. [129].

The time domain electric field of a single particle i observed in position r will be denoted as $\boldsymbol{E}_i(\boldsymbol{r}, t)$. Assuming that the field generated by each particle is equal, differing only by the time shift Δt_i, representing the particle's longitudinal location within the bunch, the total electric field can be written as a superposition of individual fields:

$$\boldsymbol{E}(\boldsymbol{r}, t) = \sum_{i=1}^{N} \boldsymbol{E}_i(\boldsymbol{r}, t) = \sum_{i=1}^{N} \boldsymbol{E}_1(\boldsymbol{r}, t - \Delta t_i). \tag{3.6}$$

The assumption that all the particles radiate in the same way up to the time delay is valid in the case of ChDR if the transverse size of the bunch is small in comparison to the longitudinal size and the impact parameter. Under such conditions, one can assume that the bunch is one-dimensional, i.e. the transverse width is equal to zero. Discussion on effects of non-zero transverse size can be found in e.g. Ref. [130].

Equation (3.6) transformed into frequency domain takes the following form:

$$\begin{aligned}
&\boldsymbol{E}(\boldsymbol{r}, \omega) = \int_{-\infty}^{\infty} \boldsymbol{E}(\boldsymbol{r}, t) e^{j\omega t} dt = \int_{-\infty}^{\infty} \sum_{i=1}^{N} \boldsymbol{E}_1(\boldsymbol{r}, t - \Delta t_i) e^{j\omega t} dt = \sum_{i=1}^{N} \int_{-\infty}^{\infty} \boldsymbol{E}_1(\boldsymbol{r}, t - \Delta t_i) e^{j\omega t} dt = \\
&= \sum_{i=1}^{N} \int_{-\infty}^{\infty} \boldsymbol{E}_1(\boldsymbol{r}, t) e^{j\omega(t + \Delta t_i)} dt = \sum_{i=1}^{N} \int_{-\infty}^{\infty} \boldsymbol{E}_1(\boldsymbol{r}, t) e^{j\omega t} e^{j\omega \Delta t_i} dt = \int_{-\infty}^{\infty} \boldsymbol{E}_1(\boldsymbol{r}, t) e^{j\omega t} dt \cdot \sum_{i=1}^{N} e^{j\omega \Delta t_i} = \\
&= \boldsymbol{E}_1(\boldsymbol{r}, \omega) \cdot \sum_{i=1}^{N} e^{j\omega \Delta t_i}.
\end{aligned}$$

As shown in Appendix A of Ref. [129], the spectrum of the energy radiated by the bunch into the far-field zone is given as

$$\frac{dE}{d\omega} = \left\langle 2\epsilon_0 c |\boldsymbol{E}(\boldsymbol{r}, \omega)|^2 \right\rangle,$$

where $\langle \cdot \rangle$ denotes the bunch ensemble average and ϵ_0 denotes the permittivity of the vacuum. As a result, one has

$$\frac{dE}{d\omega} = \left\langle 2\epsilon_0 c \left| \boldsymbol{E}_1(\boldsymbol{r}, \omega) \cdot \sum_{i=1}^{N} e^{j\omega \Delta t_i} \right|^2 \right\rangle = 2\epsilon_0 c \, |\boldsymbol{E}_1(\boldsymbol{r}, \omega)|^2 \left\langle \left| \sum_{i=1}^{N} e^{j\omega \Delta t_i} \right|^2 \right\rangle = \frac{dE_1}{d\omega} \left\langle \left| \sum_{i=1}^{N} e^{j\omega \Delta t_i} \right|^2 \right\rangle,$$

where $\frac{dE_1}{d\omega}$ denotes the spectral density of energy radiated by a single particle, given, e.g., by Eqs. (3.2), (3.3) and (3.5). The term $\left\langle \left| \sum_{i=1}^{N} e^{j\omega\Delta t_i} \right|^2 \right\rangle$ can be written as

$$\left\langle \left| \sum_{i=1}^{N} e^{j\omega\Delta t_i} \right|^2 \right\rangle = \left\langle \left(\sum_{i=1}^{N} e^{j\omega\Delta t_i} \right) \left(\sum_{i=1}^{N} e^{-j\omega\Delta t_i} \right) \right\rangle =$$

$$= \left\langle \sum_{i=1}^{N} e^{j\omega(\Delta t_i - \Delta t_i)} + \sum_{\substack{i,k=1 \\ i\neq k}}^{N} e^{j\omega\Delta t_i} \left(e^{j\omega\Delta t_k} \right)^* \right\rangle = N + N(N-1) \left\langle e^{j\omega\Delta t_i} \right\rangle^2,$$

where the last equality follows from the independence of individual time delays Δt_i. The $\left\langle e^{j\omega\Delta t_i} \right\rangle^2$ term is often called *bunch form factor*, as it depends on the distribution of the particles within the bunch, and denoted $F(\omega)$. If the normalised longitudinal bunch profile is given by $\mathcal{B}(t)$, the form factor can be calculated as

$$F(\omega) = \left(\int_{-\infty}^{\infty} e^{j\omega\Delta t} \mathcal{B}(\Delta t) d\Delta t \right)^2, \tag{3.7}$$

which means that the form factor is given by the Fourier transform of the longitudinal bunch profile.

The above discussion can be concluded with a compact formula, linking the spectral distribution of the energy radiated by the whole bunch with the spectrum of a single particle radiation:

$$\left\langle \frac{dE}{d\omega} \right\rangle = \frac{dE_1}{d\omega} \left[N + N\left(N-1\right) F\left(\omega\right) \right]. \tag{3.8}$$

Equation (3.8) is very important for further consideration, and it is worth analysing in detail. It can be seen that the right side of the equation consists of two terms. The first is proportional to N and does not depend on the form factor. This is the so-called *incoherent* term, corresponding to the independent and uncorrelated radiation of individual particles. The second term is proportional to roughly $N^2 \cdot F(\omega)$. This component describes the energy radiated by the bunch acting as a single entity. This takes place at frequencies for which radiation emitted by all particles match in phase, and is determined by the value of the form factor $F(\omega)$. This can be illustrated with an example of a Gaussian bunch profile and the spectral distribution of ChDR as predicted by the Olsen model, Eq. (3.2). A convenient property of the Gaussian bunch is that its form factor also has a Gaussian shape, with a standard deviation given by

$$\sigma_\omega = \frac{1}{\sigma_\tau},$$

where σ_τ is the standard deviation of the Gaussian longitudinal bunch profile.

The expected spectral distribution of the stationary flat-radiator ChDR generated by a Gaussian bunch is depicted in Fig. 3.9. The distance between the radiator and the bunch, as well as the dielectric permittivity, are taken as in the case of Fig. 3.5. The length and intensity of the bunch are typical for the CLEAR facility [131]; $\sigma_\tau = 1$ ps and $N = 6.24{\times}10^8$. It can be seen that in the first, low frequency part of the plot, the spectrum follows the same pattern as in the original single particle distribution, but with absolute values scaled by N^2. This *coherent* region covers frequencies up to approximately $\dfrac{1}{\sigma_\tau}$, where the radiated energy falls abruptly. For higher frequencies, the expected radiated energy is proportional to the single-particle spectrum with a scaling factor of N. To some extent, this description remains valid for bunch profiles other than Gaussian, but in these cases the form factor is usually less regular and the spectrum of the radiated energy is not so smooth.

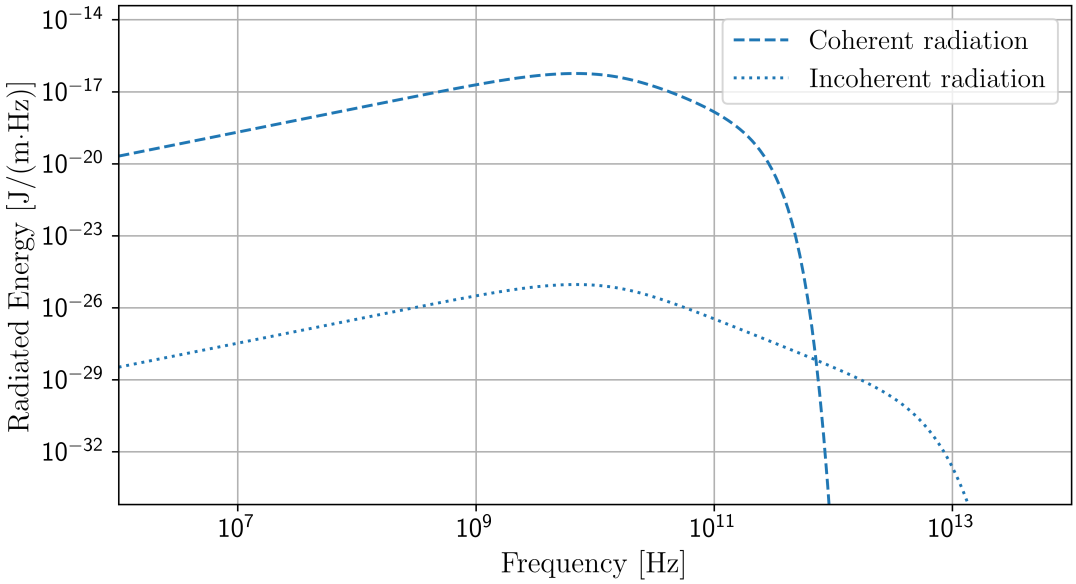

Figure 3.9: Spectral distribution of coherent and incoherent ChDR for 1 ps electron bunch.

Another important aspect of Eq. (3.8) is that it does not describe the actual radiated energy, but the expected, or equivalently, average, radiated energy. Averaged term $\left|\sum_{i=1}^{N} e^{j\omega\Delta t_i}\right|^2$ can in principle take any value between 0 and N^2. For low values of ω, one has $\omega\Delta t_i \ll 1$, so

$$\left|\sum_{i=1}^{N} e^{j\omega\Delta t_i}\right|^2 \approx \left|\sum_{i=1}^{N} 1\right|^2 = N^2.$$

On the other hand, if $\omega\Delta t_i \gg 1$, then $e^{j\omega\Delta t_i}$ might be considered as a random point on a unit circle. The total sum $\sum_{i=1}^{N} e^{j\omega\Delta t_i}$ corresponds to the N-step random walk on a complex plain. This

problem is well known in the literature [132]. Both the mean value and the standard deviation of $\left|\sum_{i=1}^{N} e^{j\omega\Delta t_i}\right|^2$ for $\omega\Delta t_i \gg 1$ and large N are equal to N. As a consequence, the incoherent radiation features a high relative variability, and possibilities of deriving information from a single burst of radiation are limited.

3.3 The ChDR Dependence on Key Parameters

In this section, the dependence of ChDR on key parameters will be discussed. This might serve as a further analysis of Eqs. (3.2), (3.3) and (3.5), but also as a first step toward using ChDR as a tool for beam diagnostics. For the presented analysis reference beam conditions of the CERN's CLEAR facility are assumed. Unless otherwise stated, all results are given for a single electron passing in 1 cm distance along a flat PTFE, $\epsilon = 2.1$, target. The velocity of the electron corresponds to the Lorentz factor $\gamma = 392$, which is equivalent to the energy of approximately 200 MeV.

Predicted properties of ChDR are different depending on whether one follows the stationary or non-stationary model. The focus is on flat radiators, with stationary results obtained with Ulrich model, Eq. (3.3), and non-stationary based on PCA, Eq. (3.5). In the latter case, a long 1 km radiator is assumed to exclude the contribution of diffraction radiation. Similarly as in the previous section, the obtained energy yield is scaled down to correspond to 1 m long radiator.

3.3.1 Impact Parameter

The most important parameter for the ChDR yield is the impact parameter, the distance between a particle and the radiator surface. Spectral distributions of the energy emitted by a particle at three different impact parameters are presented in Figs. 3.10 and 3.11 for stationary and nonstationary ChDR, respectively. As a reference, the Frank and Tamm curve for Cherenkov radiation is also provided.

In stationary and non-stationary cases, in the low frequency limit the amount of emitted radiation is proportional to the frequency, in a similar manner as for the Cherenkov radiation. This relation holds roughly up to the frequency at which the wavelength of the considered radiation is comparable to the impact parameter. At higher frequencies, the behaviour of the distribution curves differs for stationary and non-stationary models. In the stationary case, the emitted energy starts to fall at a rate proportional to the inverse square of the frequency. In the non-stationary case, after reaching its maximum, the amount of radiated energy stays constant at a wide plateau. Finally, in the high frequency limit both models predict an exponential decay of the radiated energy.

At fixed radiation frequency, for instance $f = 100$ GHz, one might observe the energy radiated within the thin spectral band around f as a function of the impact parameter h. This relation is presented in Fig. 3.12 for the stationary and non-stationary case. As can be seen, the emitted radiation stays at the constant level for low impact parameters. Then, at intermediate distances, the amount of energy emitted drops proportionally to $1/h^3$ in the stationary case and $1/h$ in the non-stationary case. At large impact parameters the decrease of radiation intensity is exponential.

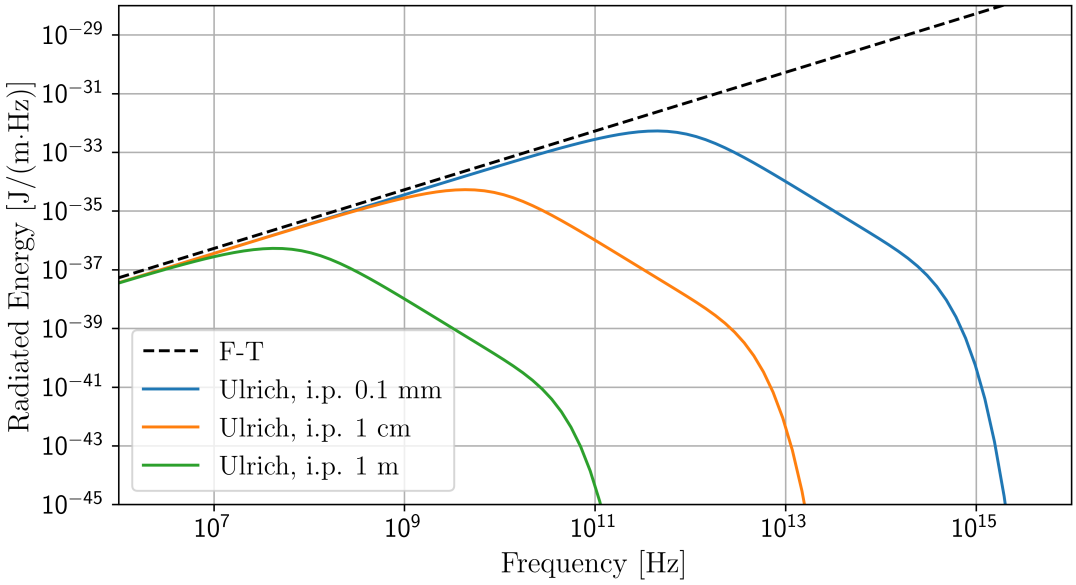

Figure 3.10: Effect of impact parameter on stationary ChDR.

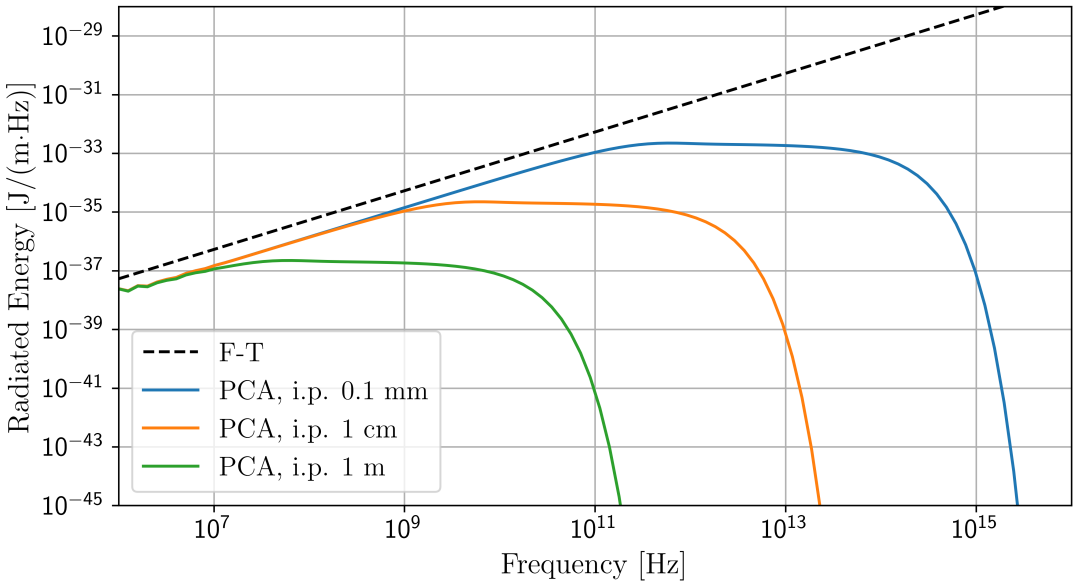

Figure 3.11: Effect of impact parameter on non-stationary ChDR.

3.3.2 Beam Energy

The beam energy affects the ChDR yield in an indirect way, as only the velocity of the particles plays a role here. For that reason, comparing electron and proton beams of the same energy, electrons would emit more radiation as a result of their lower mass.

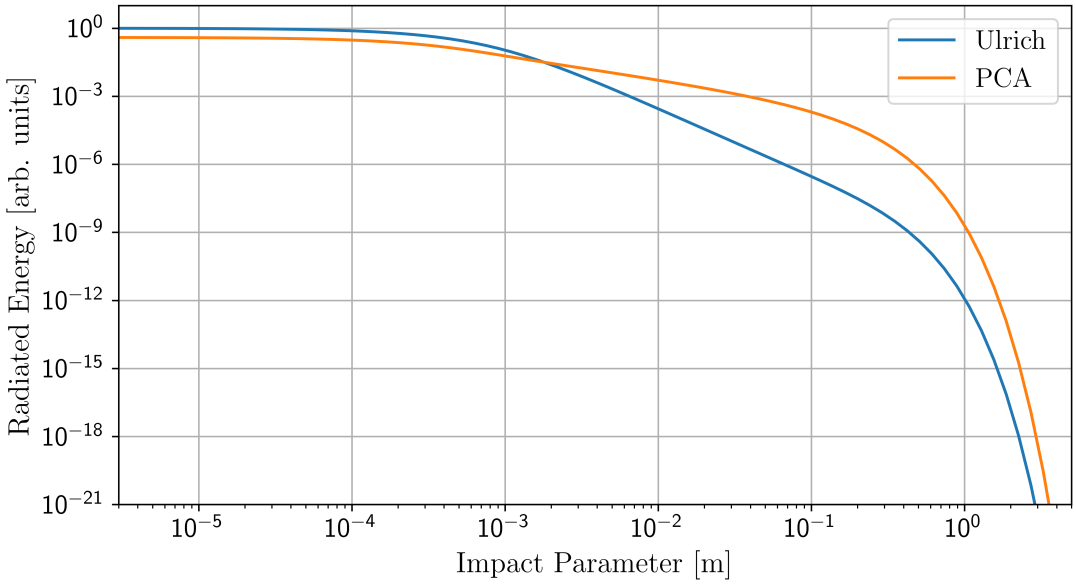

Figure 3.12: Impact parameter scan curves for 100 GHz ChDR.

The most fundamental constraint for particle velocity is that it has to exceed the c/n threshold for ChDR radiation to appear. Above this threshold, to discuss the effect of the particle velocity, it is the most convenient to use the Lorentz relativistic factor γ.

The electric field of a relativistic particle is not spherically symmetric but flattens towards the plane perpendicular to the direction of motion. As a consequence, the field of high-energy particle penetrates the radiator at larger depth. For a given wavelength λ one defines *effective radius* of the field, given as

$$r_{eff} = \gamma\lambda = \frac{2\pi\gamma}{\omega},$$

in order to estimate the limit distance at which the particle is still capable of effectively interact with the medium.

The impact of the effective radius can be observed in spectral distributions of the radiated energy predicted by stationary as well as non-stationary models. These are presented in Figs. 3.13 and 3.14 for few values of γ parameter. The width of the intermediate spectral regime of distributions strictly depends on the value of the relativistic γ factor. The intensity of ChDR drops abruptly if the effective radius is reduced to less than the impact parameter.

As a consequence, if one considers only the radiation emitted in a narrow band around a frequency $f = \frac{c}{\lambda}$, the ChDR yield changes with beam energy only if the effective radius is comparable or lower than the impact parameters. At sufficiently high beam energies, the ChDR yield stabilises

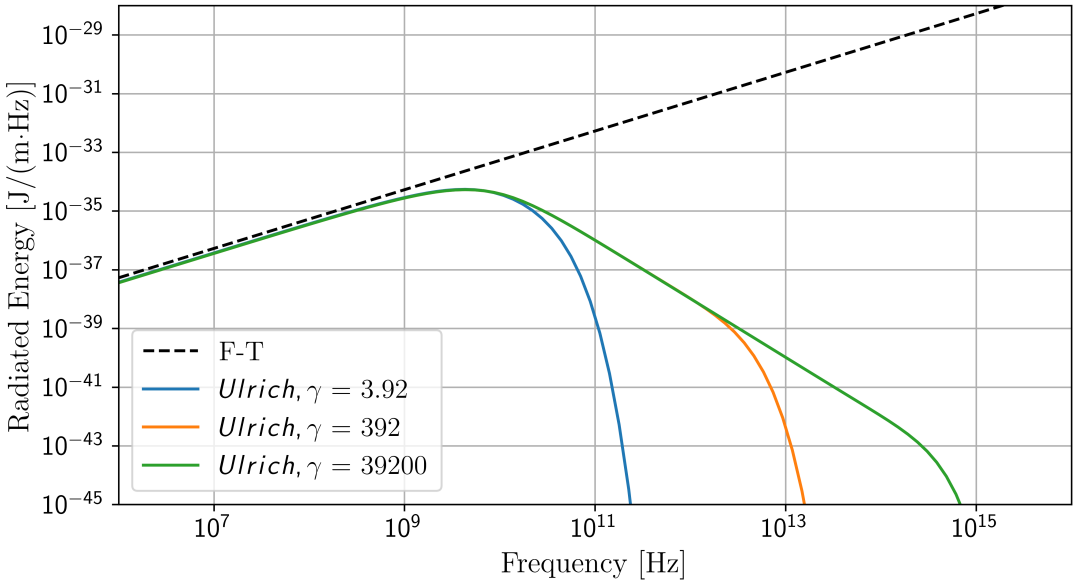

Figure 3.13: Effect of particle velocity on stationary ChDR.

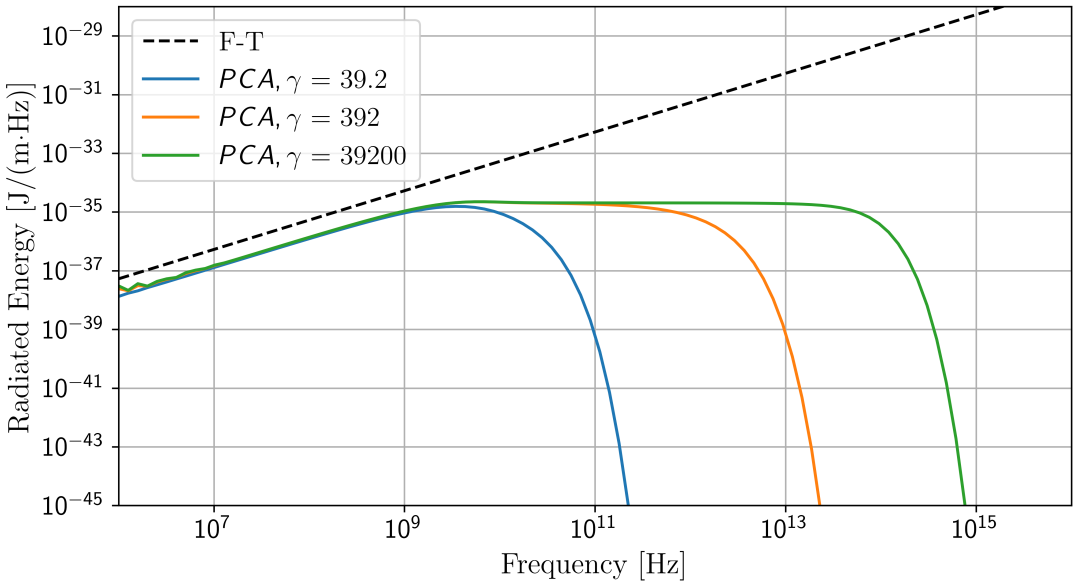

Figure 3.14: Effect of particle velocity on non-stationary ChDR.

at a constant value, as shown in Fig. 3.15, which describes the energy dependence of the ChDR emitted by a particle at 1 cm impact parameter.

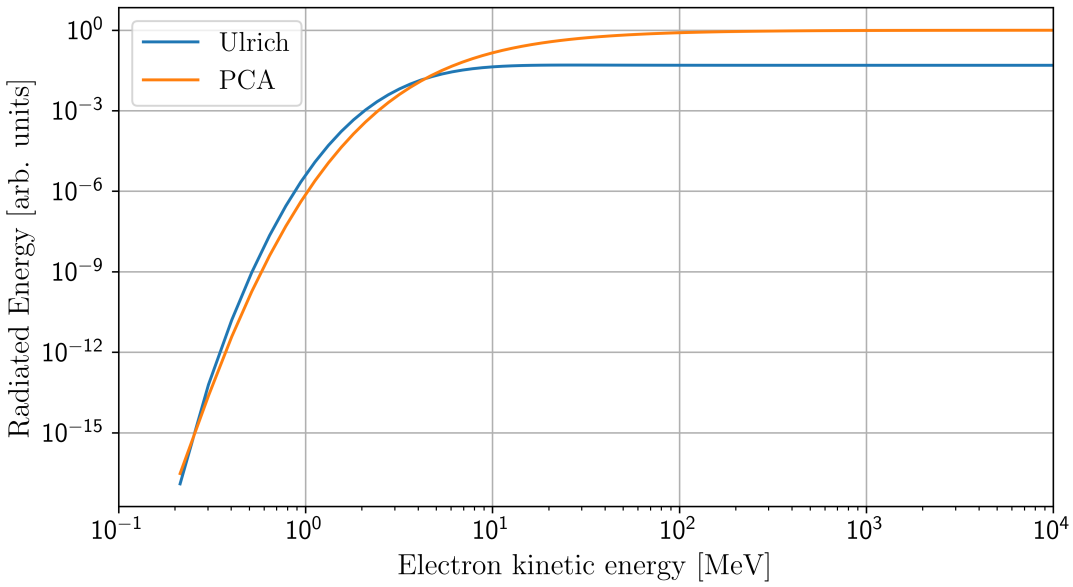

Figure 3.15: Kinetic energy dependence of 100 GHz ChDR yield.

3.3.3 Bunch Profile

As discussed in subsection 3.2.3, the spectral distribution of the radiation emitted by a particle bunch is a sum of a coherent and incoherent components. The coherent component represents the radiation emitted by a bunch acting as a single particle. At low frequencies the bunch length is short with respect to the wavelength, and hence individual particle contributions to the total radiation add up constructively. The intensity of coherent radiation is proportional to the squared charge of the particle bunch.

At high frequencies, when the radiation wavelength is much shorter than the longitudinal interval occupied by particles, individual radiation contributions add up with random phases, which might be either constructive or destructive for the total radiation yield. This represents an incoherent component of the radiation intensity, which scales on average with the total charge of the particle bunch.

The amount of energy radiated in the intermediate frequency regime, as predicted by Eqs. (3.7) and (3.8), depends on the Fourier transform of the bunch profile. In the simplest to analyze case of a Gaussian bunch profile, the transition between the coherent and incoherent regime is sharp and occurs at a frequency proportional to $\frac{1}{\sigma_\tau}$, where σ_τ is a standard deviation of the Gaussian bunch profile. This is shown in Fig. 3.16. For 1 ns bunch the coherent regime covers only frequencies below 1 GHz. If the case of 1 ps bunches, which is a typical value for e.g. the CLEAR facility, the

coherent radiation covers frequency range almost up to the far infrared. For extremely short 1 fs bunches, the whole range in which ChDR is effectively emitted is coherent.

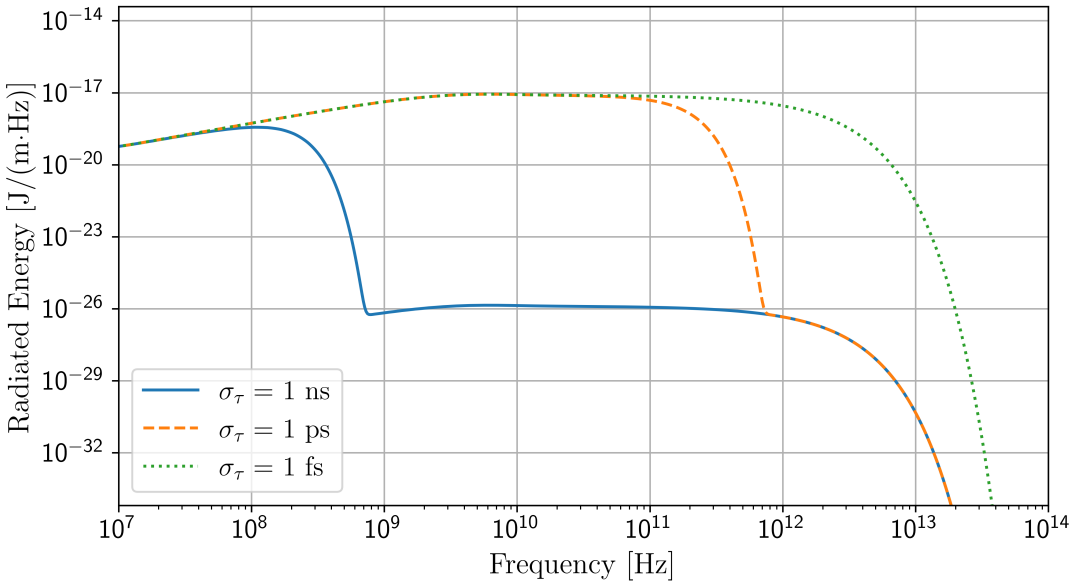

Figure 3.16: Effect of Gaussian bunch length σ_τ on ChDR.

A Gaussian bunch is however not a universal longitudinal profile. A variety of different profiles are observed in modern accelerators, and their form factors have a more complex form. In CERN's CLEAR facility, apart from Gaussian profiles, bunches of a skewed Gaussian form are also observed [111]. These can be parameterized, in addition to σ_τ, by a unitless skewness parameter α. For the skewed Gaussian profile given by

$$\mathcal{B}(t) = N \cdot C_{norm} \cdot e^{\frac{t^2}{2\sigma_\tau^2}} \left(1 + erf\left(\frac{\alpha t}{\sigma_\tau}\right)\right),$$

where C_{norm} is the normalisation constant and $erf(\cdot)$ denotes the Gauss error function, the form factor reads [111, Appendix]:

$$F(\omega) = e^{\frac{\sigma_\tau^2 \omega^2}{2}} \left[1 + erf\left(j \frac{\alpha \sigma_\tau^2 \omega}{\sqrt{1 + 2\alpha^2 \sigma_\tau^2}}\right)\right].$$

Another frequently observed profile, often assumed to be a reference LHC bunch profile, can be

described by the following expression:

$$\mathcal{B}(t) = N \cdot C_{norm} \cdot \left(1 - \left(\frac{2t}{\text{Bunch length}}\right)^2\right)^{\frac{5}{2}}. \tag{3.9}$$

In the scope of this thesis this type of profile will be called $\frac{5}{2}$-*parabolic profile*, as an analogy to *parabolic profile* described in Ref. [80]. The only difference between these two is the $\frac{5}{2}$ power present in Eq. (3.9). The form factor corresponding to this bunch profile has no simple analytical form, and a numerical evaluation of the form factor is required. Gaussian, skewed Gaussian and parabolic profiles of a comparable bunch length are depicted in Fig. 3.17 and the corresponding spectral distributions of non-stationary ChDR are presented in Fig. 3.18.

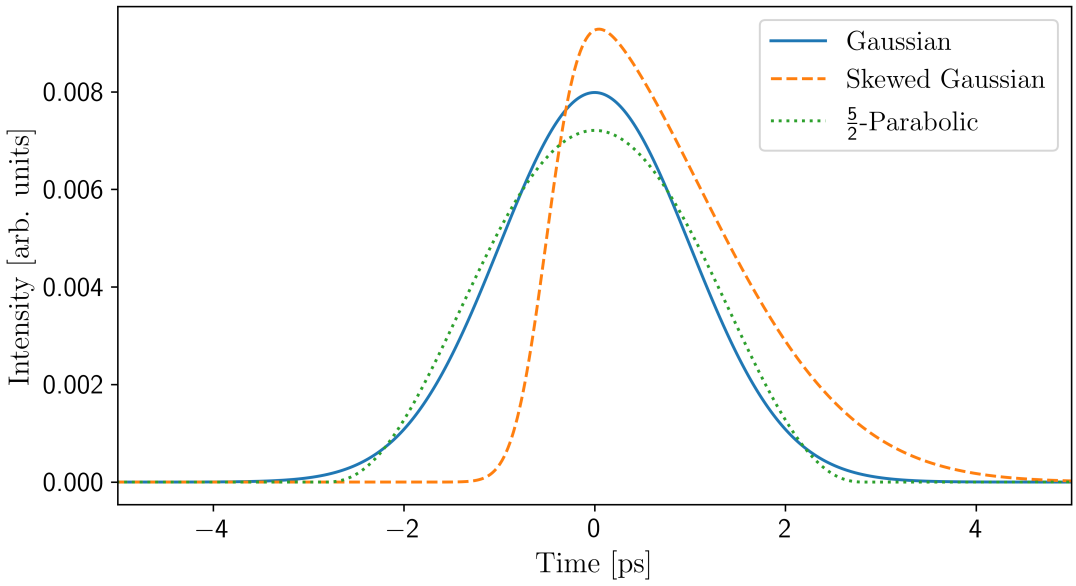

Figure 3.17: Gaussian, skewed Gaussian and $\frac{5}{2}$-parabolic bunch profiles profiles.

It can be seen that similarly as for the Gaussian spectrum, the skewed Gaussian results with a smooth distribution, but extended towards higher frequencies. On the other hand, the parabolic profile, which in principle does not differ drastically from the Gaussian one, has a significantly more complex spectrum. While at lower frequencies the coherent signal fade slightly faster, a series of resonances preserves some sort of coherent signal up to frequencies one order of magnitude higher than the Gaussian coherent regime limit. One can conclude that in addition to inherent fluctuations of the incoherent signal, mentioned in the previous section, radiation above the theoretical limit of

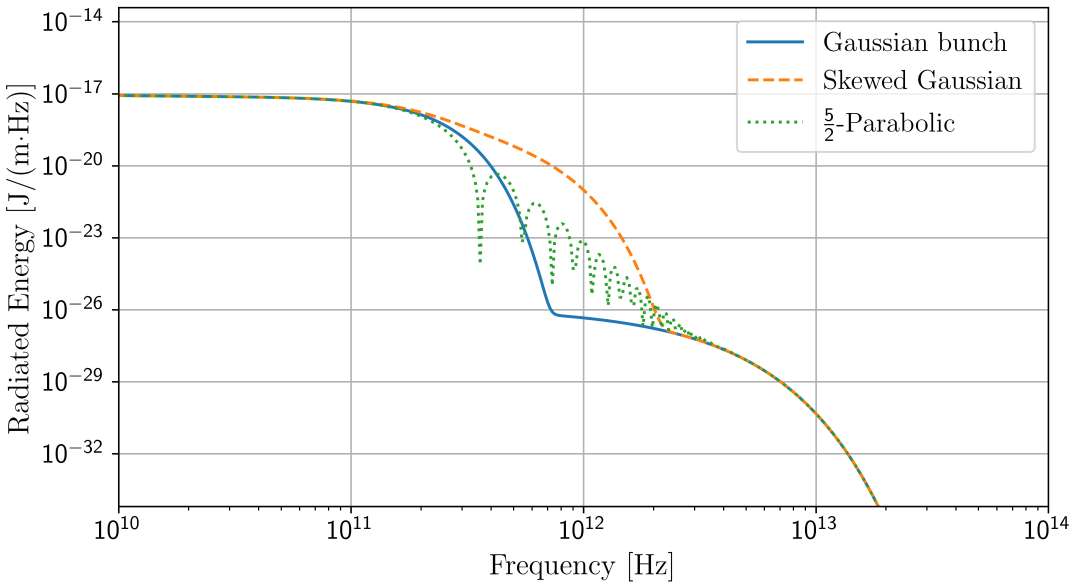

Figure 3.18: Effect of different bunch profiles velocity on non-stationary ChDR.

the coherent signal is very sensitive to changes in the bunch profile.

3.3.4 Dielectric Permittivity

For highly energetic beams, the dielectric permittivity of the medium primarily determines the ChDR emission angle. The radiation front propagates at angle $\theta = \arccos \frac{1}{n\beta}$, where the refractive index n is given as a square root of the permittivity. Assuming the real constant permittivity, the impact of the permittivity on ChDR intensity is, however, very limited. This situation changes if one assumes that the actual permittivity of the material is frequency dependent and complex, $\epsilon(\omega) = \epsilon'(\omega) + j\epsilon''(\omega)$. The positive imaginary permittivity leads to absorption losses within the medium. At so called *resonant frequencies*, value of the real permittivity changes, and the absorption is especially strong.

The issues and challenges related to the dependence of the permittivity on the frequency can be illustrated with an example of fused silica SiO_2, a dielectric medium commonly used in studies of visible radiation. The dielectric permittivity of SiO_2, reported in Ref. [133], is presented in Fig. 3.19. In the low frequency limit, the imaginary permittivity is negligible, and the real part is equal to approximately 3.8. Then, for frequencies in range 10-40 THz the real part of permittivity changes rapidly, and the imaginary part becomes significant. At these frequencies the medium is opaque to the radiation and the emission angle is difficult to predict. For certain frequencies, the real permittivity drops even below the Cherenkov threshold making the emission of ChDR

impossible. The emission is feasible again for infrared and visible wavelengths, where the real permittivity stabilises at the level of approximately $\epsilon = 2.1$. Then, the near-ultraviolet radiation is heavily absorbed by the medium. At higher frequencies the absorption vanishes, but the medium permittivity approaches the vacuum limit and no radiation can be emitted, as the Cherenkov velocity threshold approaches the velocity of light.

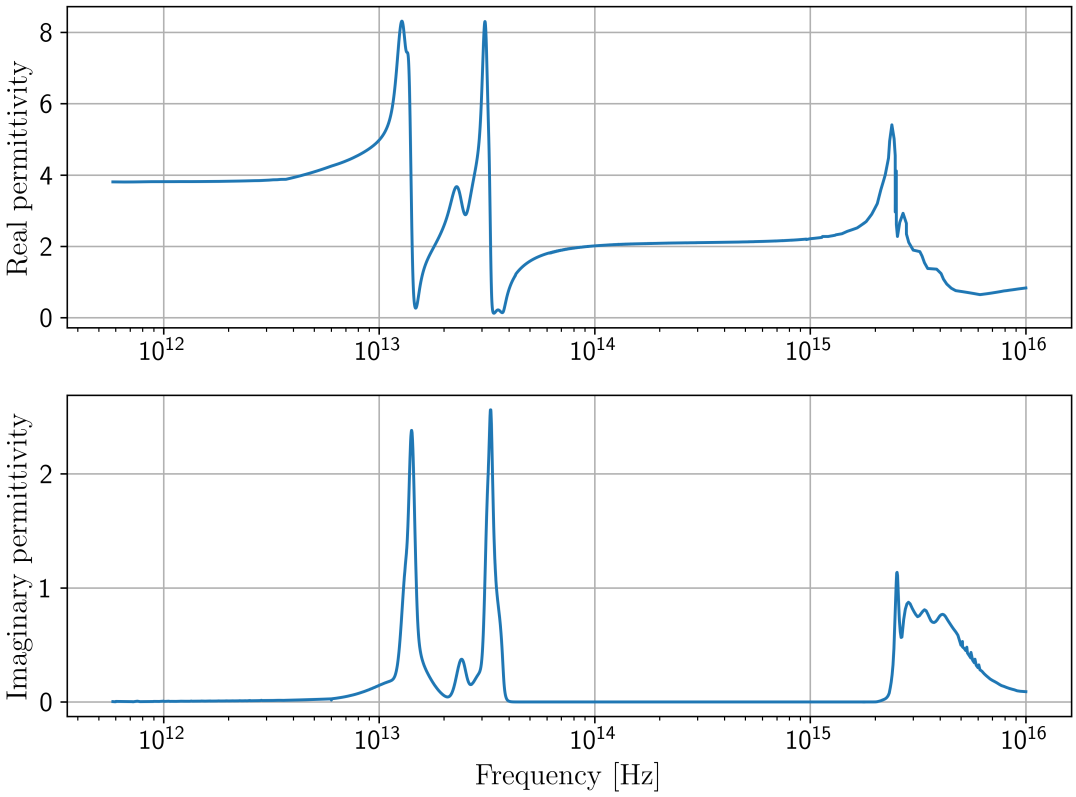

Figure 3.19: Real and imaginary permittivity of SiO_2.

3.4 Prediction of ChDR with IW2D Code

The theory presented in Section 3.2 and illustrated with various examples in Section 3.3 facilitates the characterisation of the basic properties of ChDR and the estimation of the expected radiation yield. On the other hand, analytic models serve well only in a limited spectrum of cases, due to the simplicity of the considered radiators. This motivates the need to develop a tool for the quantitative description of ChDR for real-life scenarios. Numerical simulations, such as those performed with the CST Particle Studio [134], are time consuming, especially if the radiator components differ significantly in size. The aim of this section is to present a semi-analytical approach, which is based on numerical calculations of the beam field propagating across surrounding materials, according to constraints set by the Maxwell equations. Although the presented procedure describes radiators infinite in the direction of beam propagation, sharing the limitations of stationary models, it gives the possibility for studying complex multilayer structures orthogonal to the direction of beam propagation.

The development of the framework for ChDR estimation in the case of multilayered radiators brings new possibilities in diagnostic device design. Although transparent dielectric materials still remain the core of the radiating structure, one can now also study the impact of thin coatings present on the surface of the dielectric. Such a study can be motivated by a range of, often completely independent, reasons. One might try to reshape a ChDR spectrum in such a way that the photon yield at the measurement frequencies is maximal. This can be achieved by adding a thin metallic coating on a surface of the dielectric. This will result in the presence of surface waves, excited on the coating surface, which due to the interaction with the dielectric also take part in the creation of Cherenkov radiation. Alternatively, it might be that coating of the dielectric is required due to the general accelerator constraints, for example, in order to prevent the creation of electron clouds. Then, it is important to know what effect the coating will have on the spectrum of created ChDR and if it can still be used for diagnostic purposes. Finally, as the IW2D framework is not limiting the number of layers, one may, e.g. also study the effects of ageing and material oxidation, adding to the simulation an additional thin layer of the formed oxide.

The proposed method was developed by the author of this thesis as an extension of ImpedanceWake2D (IW2D), a framework for beam impedance and wakefield calculations developed at CERN [135]. For that reason, in the scope of this thesis, it will be referred to as IW2D. Using the original code, it was possible to calculate the electromagnetic field in the time and frequency domain along the beam trajectory. With the extension, the field and therefore also the energy flow can be monitored at an arbitrary point of the structure surrounding the beam.

3.4.1 Cylindrical Geometry

The IW2D framework considers two distinct geometries, both of which are relevant from the point of view of accelerator physics. The geometry presented in Fig. 3.20 is described using cylindrical coordinates r, θ and s. A charged particle travels with velocity $v = \beta c$ along the s axis in the centre of an axisymmetric structure, consisting of an arbitrary number of layers. Each layer has its own relative permittivity ϵ_i and permeability μ_i, which may be frequency dependent. The central layer is constrained to be a vacuum, but the subsequent layers may be of any material, with the outermost layer extending to infinity.

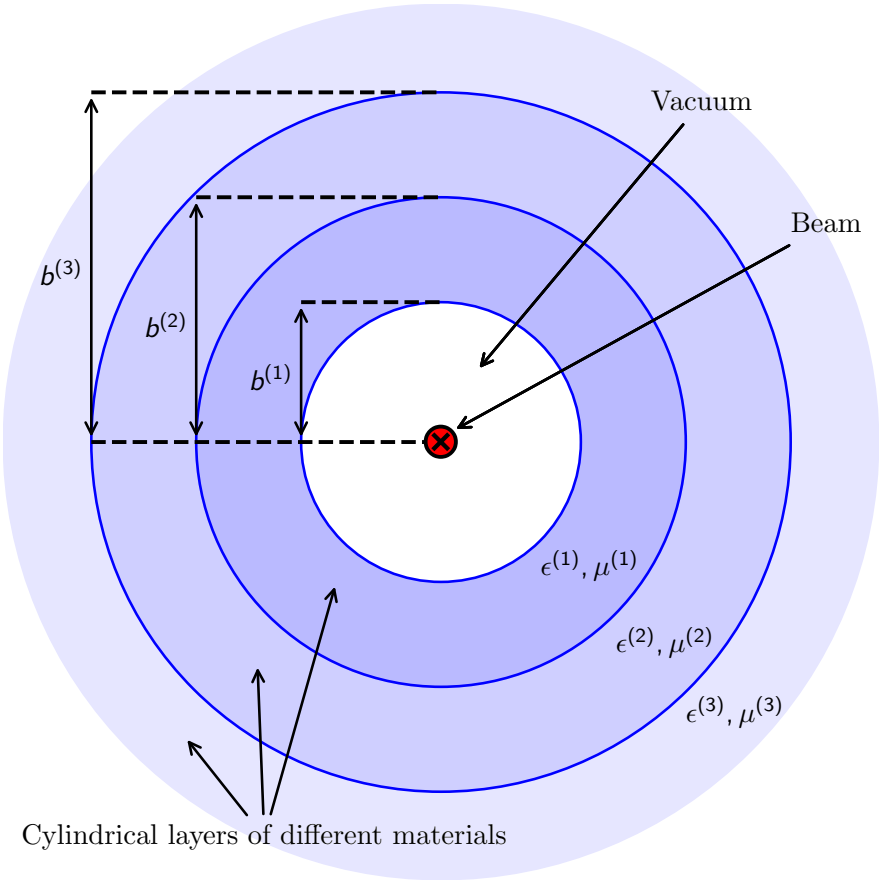

Figure 3.20: Cylindrical IW2D geometry with concentric layers of different materials.

The longitudinal components of the electric and magnetic field, $E_s^{(p)}$ and $H_s^{(p)}$, in a probe point $\vec{\mathbf{r}}$ at a distance r from the axis, located in the layer p, have the following explicit form in the frequency domain:

$$E_s^{(p)}(\vec{\mathbf{r}};\omega) = e^{-jks}\left[C_{Ie}^{(p)} I_0(\nu^{(p)} r) + C_{Ke}^{(p)} K_0(\nu^{(p)} r)\right],$$
$$H_s^{(p)}(\vec{\mathbf{r}};\omega) = 0,$$

where I_0 and K_0 are zero-order modified Bessel functions of the first and second kind, respectively, $k = \frac{\omega}{v}$ is a wave number and $\nu^{(p)} = k\sqrt{1-\beta^2\epsilon^{(p)}\mu^{(p)}}$ is a radial propagation constant. This follows from [135, Eq. (1.85)] by noting that for a centred beam, only mode $m = 0$ contributes to the field. Coefficients $C_{Ie}^{(p)}$ and $C_{Ke}^{(p)}$ can be calculated based on the frequency, particle velocity and boundary conditions within the considered structure, as described in Ref. [135, Ch. 1.4].

Based on Maxwell's equations, knowing the longitudinal components of magnetic and electric fields, one can also derive the transverse components [135, Appx. E.1.1]. In the discussed cylindrical geometry, the only non-zero transverse components will be E_r and H_θ.

In particular, the goal will be to obtain the energy radiated per unit length of the particle's trajectory. In order to derive this quantity, one defines

$$\vec{P}(\vec{\mathbf{r}};\omega) = \Re\left[\vec{E}(\vec{\mathbf{r}};\omega) \times \vec{H}^*(\vec{\mathbf{r}};\omega)\right],$$

where $\vec{H}^*$ is the complex conjugate of the magnetic field $\vec{H}$ and $\Re[\cdot]$ denotes the real part of a vector. As a consequence of the Poynting theorem, the total energy radiated outside a given volume V is given by

$$\Delta E(V) = \frac{1}{\pi}\int_0^\infty d\omega \oiint_{\mathbf{A}=\partial V} \vec{P}(\vec{\mathbf{r}};\omega)\cdot d\mathbf{A}. \tag{3.10}$$

One can take now V to be a cylinder of length l and radius r, concentric to other layers. It should be noted that due to the longitudinal invariance of a given geometry, the contributions to Eq. (3.10) of the front and back faces of the cylinder cancel each other out. One has then

$$\Delta E(V) = \frac{1}{\pi}\int d\omega \int_0^{2\pi} d\theta \int_0^l ds \vec{P}_r(r,\theta,z;\omega)_r,$$

where $\vec{P}_r$ is the radial component of $\vec{P}$. Again, using longitudinal invariance, together with the axis symmetry of the system, one can write

$$\vec{P}_r(r,\theta,z;\omega)_r = \vec{P}_r(r;\omega),$$

so that

$$\Delta E(V) = 2lr \int d\omega \ \vec{P}_r(r;\omega).$$

As a result,

$$\frac{dE}{ds}(r) = 2r \int d\omega \ \vec{P}_r(r;\omega), \tag{3.11}$$

where $\frac{dE}{ds}(r)$ is the total energy radiated outside the cylinder of radius r in the radial direction per unit length of the particle trajectory. It should be noted that the total energy radiated outside the cylinder may vary with the change of r, especially in the presence of layers having complex permittivity.

3.4.2 Flat Geometry

The second geometry considered is a flat geometry described using Cartesian coordinates x, y and s. It consists of a series of infinitely long and wide plates, each having its own thickness, permittivity ϵ_i and permeability μ_i. A charged particle travels in the longitudinal direction, along the s axis, inside the central layer, which again is constraint to be vacuum. It is also assumed that the top and bottom outermost layers are infinitely thick. An example of such a structure is presented in Fig. 3.21.

For a probe point $\vec{\mathbf{r}}$ placed in layer p, the longitudinal components of the electric and magnetic field are of the form [135, Eq. (1.180,1.181)]:

$$\begin{aligned} E_s^{(p)}(\vec{\mathbf{r}};\omega) &= e^{-jks} \int_0^\infty dk_x \cos(k_x x) \left[C_{e+}^{(p)}(k_x) e^{k_y^{(p)} y} + C_{e-}^{(p)}(k_x) e^{k_y^{(p)} y} \right], \\ H_s^{(p)}(\vec{\mathbf{r}};\omega) &= e^{-jks} \int_0^\infty dk_x \sin(k_x x) \left[C_{h+}^{(p)}(k_x) e^{k_y^{(p)} y} + C_{h-}^{(p)}(k_x) e^{k_y^{(p)} y} \right], \end{aligned} \tag{3.12}$$

where $k_y^{(p)} = \sqrt{k_x^2 + {\nu^{(p)}}^2}$ is the vertical wave number, with $\nu^{(p)}$ defined as in the previous section. Coefficients $C_{e\pm}, C_{h\pm}$ depend on k_x, frequency and the properties of all layers, and can be calculated as described in in Ref. [135, Ch. 1.5]). However, integration over k_x generally does not have a simple analytical form and requires numerical calculations. The transverse components of the electromagnetic field can be derived from the longitudinal ones thanks to Maxwell equations, see Ref. [135, Appx. E.2.1].

Having all the EM field components one can calculate the radiated energy. For that, one takes Eq. (3.10) and volume V in the form of a rectangular box

$$V = V_T \times [0, z] = [x_1, x_2] \times [y_1, y_2] \times [0, z].$$

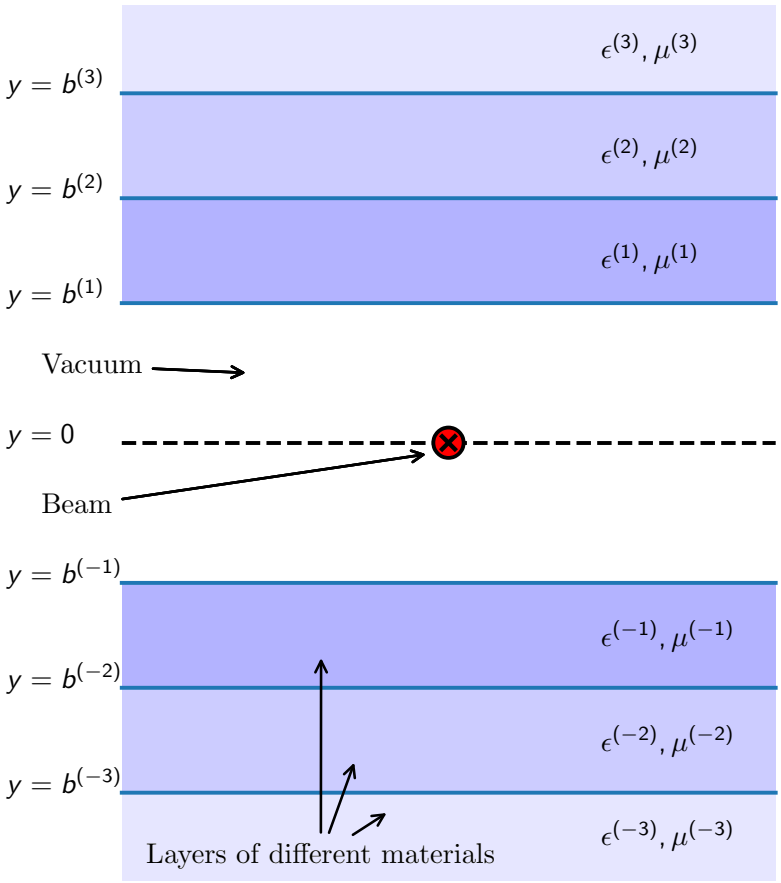

Figure 3.21: Flat IW2D geometry with parallel layers of different materials.

Similarly as in the cylindrical case, contributions from front and back faces cancel each other. One obtains the following:

$$\begin{aligned}\frac{dE}{ds}(V_T) =& \frac{1}{\pi}\int_0^\infty d\omega \int_{x_1}^{x_2} dx \vec{P}_y(x, y_2; \omega) - \vec{P}_y(x, y_1; \omega) \\ &+ \frac{1}{\pi}\int_0^\infty d\omega \int_{y_1}^{y_2} dx \vec{P}_x(x_2, y; \omega) - \vec{P}_x(x_1, y; \omega),\end{aligned} \tag{3.13}$$

where $\frac{dE}{ds}(V_T)$ is the total energy radiated outside the box V_T per unit length of the particle trajectory. As in the case of cylindrical geometry, the total energy radiated outside the box may vary with the choice of V_T, especially in the presence of layers having complex permittivity.

3.4.3 Code Implementation

The discussed formulas have been implemented in C++ language with a Python wrapper, which facilitates the analysis. As calculations require high-precision arithmetic, a 160-bit float arithmetic from ALGLIB [136] library is used. Bessel functions are evaluated using either their Taylor expansion (when the absolute value of an argument is less than 60), or with an asymptotic expression, both coming from Ref. [78]. The numerical integration of Eq. (3.10) follows the simple midpoint rule [137] and Eq. (3.12) is calculated using the adaptive integration QAG procedure, from the GNU Scientific Library [138].

The programme consists of two executable files, corresponding to, respectively, cylindrical and flat geometry. As input, a text file with probes' coordinates, frequency range, beam energy, and layers' characteristics, such as permittivity, permeability and thickness are provided. In the case of frequency-dependent permittivity or permeability, a loss tangents [139], Drude model [140] coefficients, or separate data files are accepted. The output files contain, for each probe and frequency, all components of electric and magnetic field, given in the frequency domain.

What should be emphasised is that in the case of cylindrical geometry, the computation involves only a small number of Bessel function evaluations and matrix multiplications, and is therefore very fast. On the other hand, in the flat case calculations require a time-consuming matrix inversion. On top of that, due to the complicated form of the integrand, the integration needs to be performed numerically. All this results in much slower field calculations. However, in both cases, the code supports the parallel computation of distinct probes, which can be distributed among the number of available cores.

3.4.4 Comparison with Well Established Models

To benchmark this approach, it can be compared with the predictions of analytical formulas discussed in Section 3.2. The case of a simple cylindrical geometry, with only one dielectric layer, can be compared to the Olsen model, Eq. (3.2). A spectral distribution of the energy radiated in the form of ChDR, emitted by a single electron travelling through the vacuum cylinder ($r = 3$ mm) is plotted in Fig. 3.22 for three different values of the relativistic γ factor. A non-dispersive and lossless dielectric with a refractive index $n = 1.45$, close to the value of fused silica in the visible range is assumed.

As can be seen in Fig. 3.22, predictions of the Olsen result and IW2D calculation are in perfect agreement.

The flat geometry might be benchmarked against the result of Ulrich, Eq. (3.3). A comparison

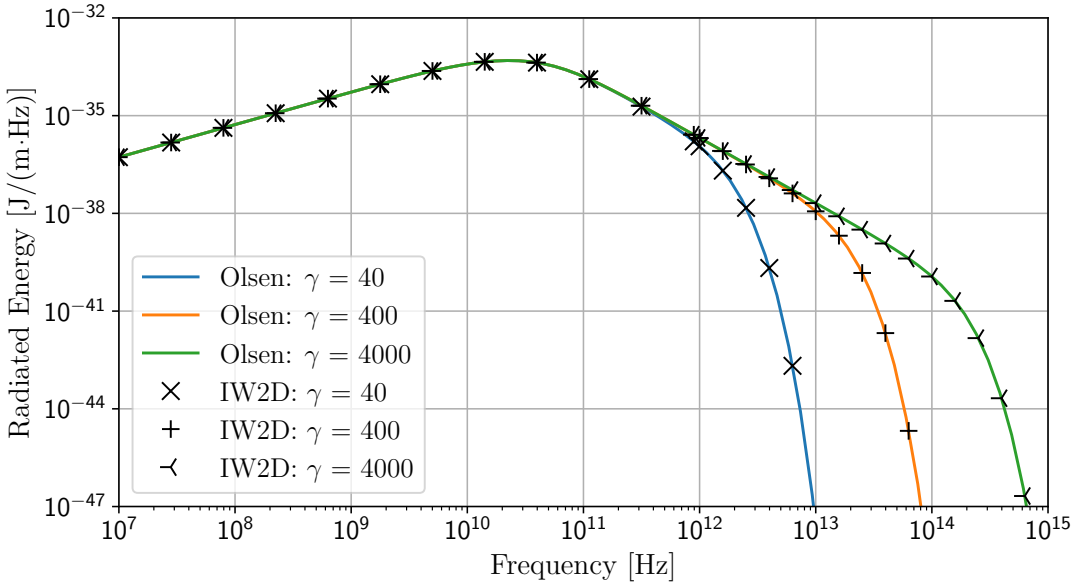

Figure 3.22: Energy radiated inside a single-layered cylindrical dielectric as predicted by IW2D and Olsen model.

between this result and the IW2D calculations is presented in Fig. 3.23. Again, the precision of IW2D has been confirmed.

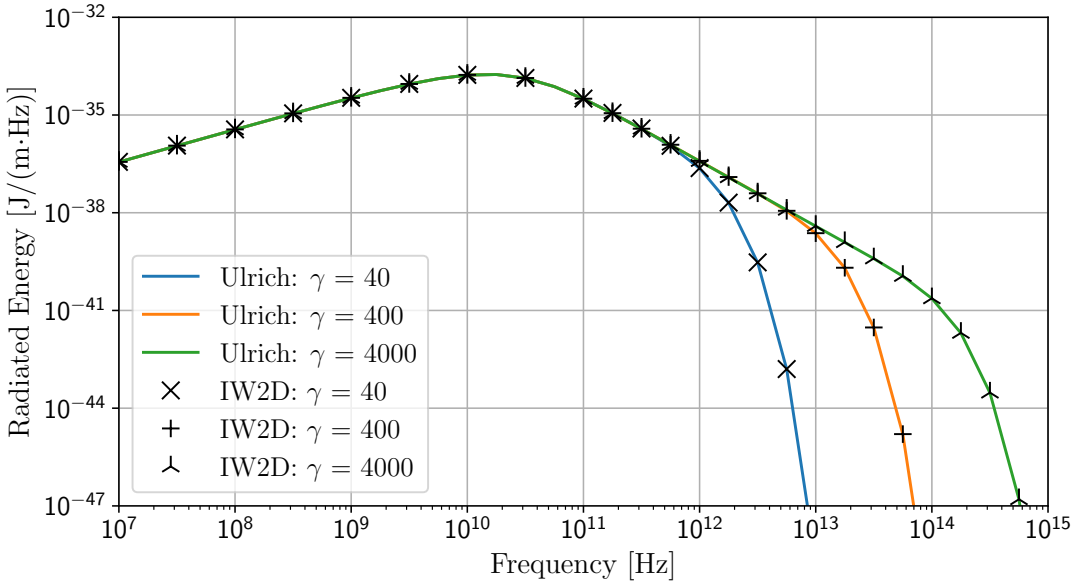

Figure 3.23: Energy radiated inside a single-layered flat dielectric as predicted by IW2D and Ulrich model.

3.4.5 Surface Plasmon Polaritons

The presence of a thin metallic layer between the beam and the dielectric may lead to the excitation of Surface Plasmon Polaritons (SPP) on the metal-vacuum and metal-dielectric intersection. As a consequence, one might observe the creation of monochromatic Cherenkov radiation with significantly enhanced intensity for particular frequencies. This effect was theoretically predicted and simulated in Ref. [31], but only for flat, infinitely wide beams, so-called *sheet beams*, or for hollow beams surrounding the cylindrical radiator.

The approach proposed in this Section allows studying the analogous effect for more realistic beam geometries, described in subsection 3.4.1 and subsection 3.4.2. It turns out that also in such cases one might observe the signal enhancement due to the thin metallic layers deposited on the surface of the radiator.

This effect can be demonstrated with the following setup, motivated by the beam parameters and dimensions of a Dielectric Laser Accelerator (DLA), reported in Ref. [141]. A point particle with a charge of 11 fC travels at a velocity corresponding to $\gamma \approx 118.42$ inside a thin silver cylinder surrounded by an infinite layer of dielectric with a refractive index of $n = 1.45$. The cylinder radius is 200 nm, and the silver layer is 80 nm thick.

For the permittivity of silver, the Drude model is adopted

$$\epsilon = \epsilon_\infty - \frac{\omega_p^2}{\omega^2 - j\gamma\omega},$$

where for silver one has $\epsilon_\infty = 5.3$ (high-frequency permittivity limit), $\omega_p = 1.39 \times 10^{16} \frac{\text{rad}}{\text{s}}$ (plasma frequency), and $\gamma = 3.2 \times 10^{13}$ Hz (damping constant), as given in Ref. [142].

In Fig. 3.24 the spectral distribution of the energy radiated in the case of just the bare dielectric and in the case of added 80 nm thick silver coating are presented. As can be observed, the presence of the metallic layer has transformed a broad ChDR spectrum into a monochromatic visible radiation of significantly higher intensity at that wavelength. The thickness of the metal layer was chosen to maximise this effect.

The resonance shape as a function of the thickness of the coating is shown in Fig. 3.25. For a thin 20 nm coating the spectral region of the increased radiation intensity covers frequencies from 600 up to 900 THz, but the overall increase is not significant. As the thickness grows, the resonance becomes thinner and higher, reaching its maximum for 80 nm coating, for which over a thin, approximately 10 THz wide band around 770 THz the radiation photon yield enhancement reaches a factor of 40. If one increases the thickness even further, the resonance curve gets thinner, but a maximum of the peak is also reduced.

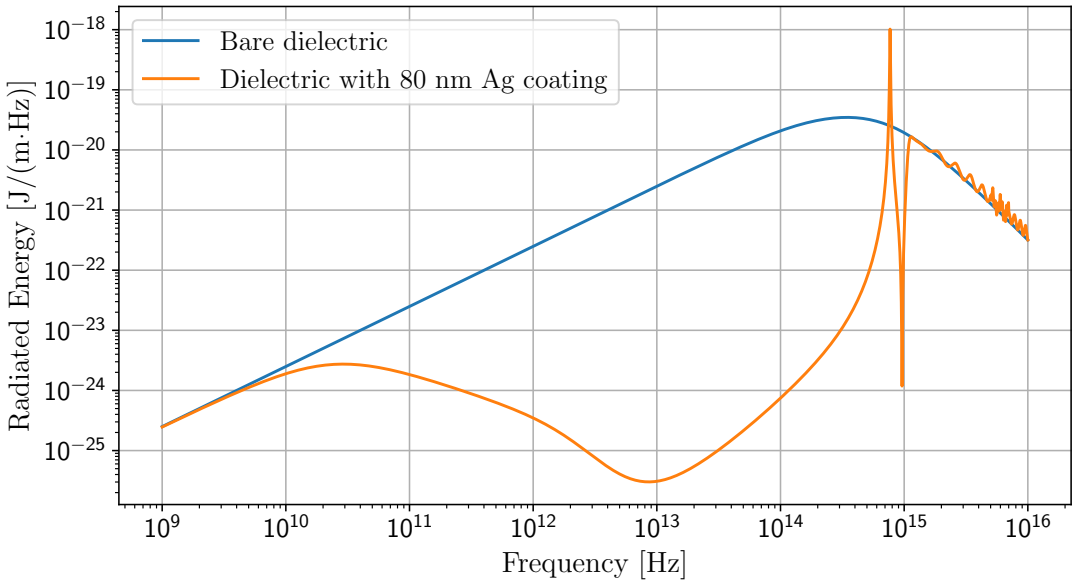

Figure 3.24: Surface Plasmon Polariton resonance at 770 THz in the cylindrical geometry compatible with a Dielectric Laser Accelerator.

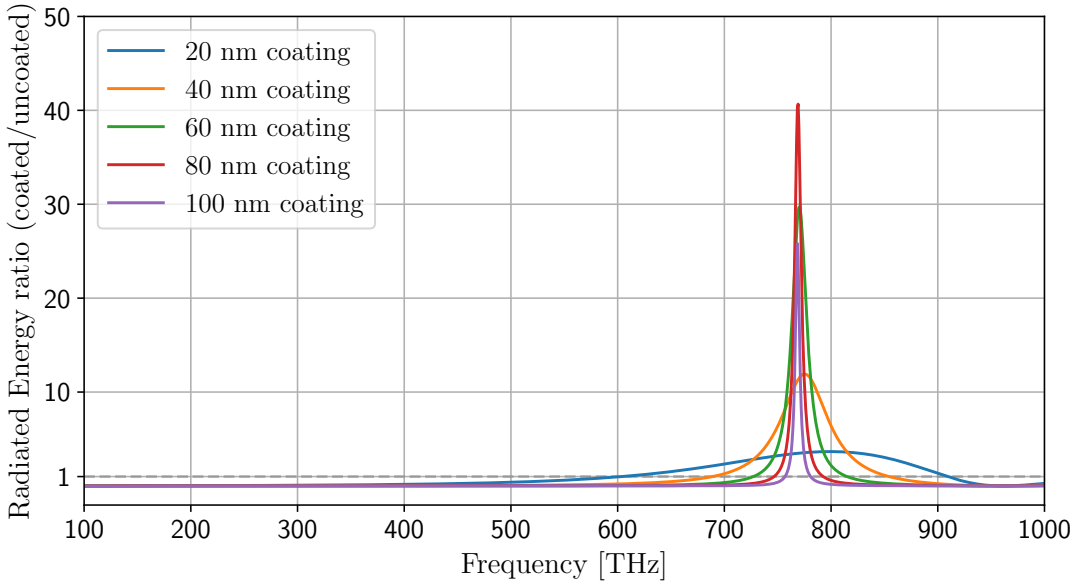

Figure 3.25: ChDR enhancement with respect to the cylindrical bare radiator for variable thickness of silver coating.

The discussed results look a little bit differently if instead of a hollow cylindrical radiator, we assume a flat one, located from one side of the particle beam. In the following, the same beam energy, intensity and distance from the surface of radiator as in the previous case will be maintained. As

can be seen in Fig. 3.26, the 80 nm thickness is not anymore a choice which leads to the highest increase in radiation yield. Moreover, adding coating does not result in the formation of narrow strong resonance peaks, but instead one can observe broad crests of the resonance lines, which span over relatively large frequency bands but only slightly surpass the original bare dielectric curve. Small discontinuities of the energy radiated in the case of coated dielectric, which can be seen in Fig. 3.26, are not physical but are artefacts of the numerical integration of Eq. (3.13).

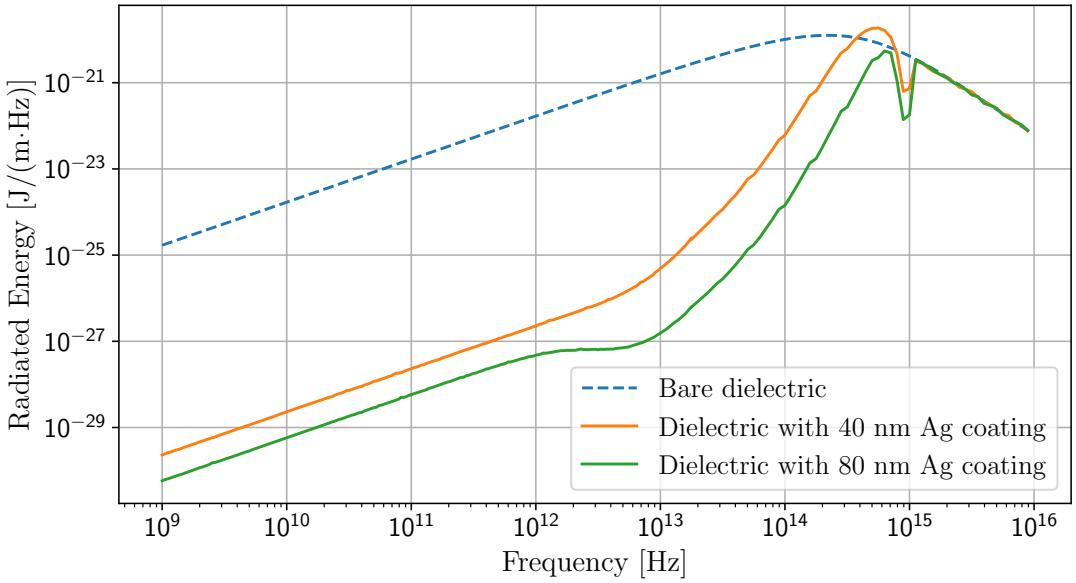

Figure 3.26: ChDR spectrum for the silver-coated radiator in the flat geometry compatible with a Dielectric Laser Accelerator.

Close examination of the ratio between the energy radiated with and without a silver coating in the case of a flat radiator reveals further differences with respect to the cylindrical case. As can be seen in Fig. 3.27, the frequency at which the enhancement is the most dominant shifts depending on the thickness of the applied coating. Yet again it can be noted that the enhancement spans in a wider range but is significantly weaker than in the case of cylindrical geometry.

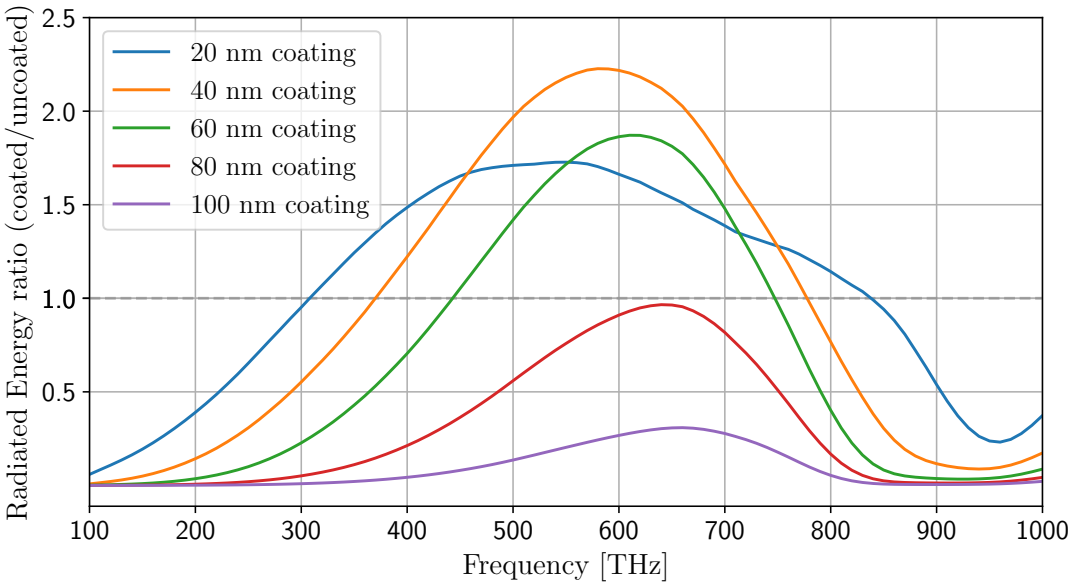

Figure 3.27: ChDR enhancement with respect to the flat bare radiator for variable thickness of silver coating.

3.5 Feasibility of ChDR-Based Diagnostics in the LHC

As predicted by theory, the intensity of ChDR falls drastically if the distance between the particle and the radiator exceeds $\gamma\lambda$, where γ is the relativistic Lorentz factor, and λ is the wavelength of the considered radiation. For this reason, most of the past investigations, discussed in Section 3.1, focused on electron or positron accelerators. The Large Hadron Collider (LHC) accelerates protons up to a velocity corresponding to $\gamma \approx 7000$, a value higher than that in the case of numerous electron machines operating today. Therefore, it is justified to ask whether ChDR diagnostics might be applied in the LHC and what are the main challenges involved.

3.5.1 Relevant Machine Parameters

Values of parameters relevant for the calculation of the ChDR radiation yield are presented in Table 3.1, including the typical characteristics of the LHC proton and ion beam. In the case of protons, *Inj* denotes the injection energy of 450 GeV, while *Flattop* stable beam energy is assumed to be equal to 6.5 TeV. For ions at Flattop, the considered energy per nucleon is equal to 2.3 TeV/u. The impact parameters considered correspond to either a standard LHC vacuum chamber dimension, 31.5 mm, or to the minimum distance, 1 mm, which could be obtained if the radiator was embedded in a collimator. For simplicity and for illustrative purposes, a frequency-independent relative permittivity of 2.1 was chosen. It is a value close to the permittivity of fused silica in the visible range and Teflon in the microwave regime, which is typically used in ChDR applications.

Table 3.1: Parameters used for ChDR estimation in the LHC

	Protons Inj	Protons Flattop	Pb^{82+}: Flattop
Relativistic γ factor	480	6928	2452
Number of particles	$1.15 \cdot 10^{11}$	$1.15 \cdot 10^{11}$	$7 \cdot 10^{7}$
Bunch length	1.2 ns		
Impact parameter	1 - 31.5 mm		
Dielectric permittivity	2.1		
Dielectric length	10 cm		

3.5.2 Radiation Yield

The energy emitted for a single-particle beam is calculated with the PCA, under assumption of a long 1 km radiator, but the result is then scaled down to correspond to more realistic, 10 cm long radiator. This configuration is chosen in order to exclude the contribution of DR from the estimates.

All results correspond to the energy radiated by a single-particle bunch, during a single passage along the radiator surface. Therefore, spectrum distortions due to the repetitive character of the radiation emission in circular machines are not included. It is assumed that the total energy spectral distribution is a sum of incoherent signals, proportional to the number of particles, and coherent longitudinal-bunch-shape-dependent signal, proportional to the number of particles squared, following the approach presented in Subsection 3.2.3.

In Fig. 3.28 a spectral density distribution is shown under the assumption of a perfectly Gaussian bunch ($4\sigma = 1.2$ ns). The strong coherent part of the spectrum ends abruptly around 1 GHz frequency, causing the measurement at higher frequencies to be extremely challenging. In addition, the observation of the visible radiation would only be possible at flat top energy and when considering a small impact parameter. It is also worth noting that the energy radiated in the coherent regime, i.e. less than a few GHz, is lower for ions compared to protons, but in the incoherent regime, the energy radiated by ions is larger than energy radiated by protons. This is because the intensity of coherent and incoherent radiation scales proportionally to q^2N^2 and q^2N respectively, where N is the number of individual charge carriers, and q is the charge of a particle.

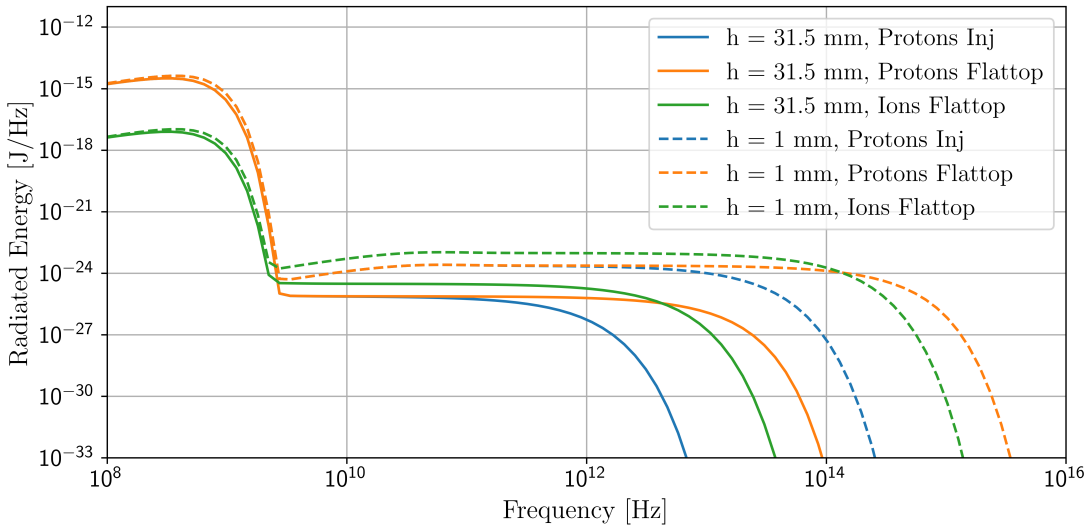

Figure 3.28: Spectral distribution of energy radiated by a Gaussian bunch.

Under realistic conditions, the LHC bunch profile deviates from a Gaussian shape. As a result,

transition between the coherent and incoherent part of the spectrum is gradual, as tails of coherence persist even for relatively high frequencies. In order to estimate to what extent this effect facilitates the measurement of ChDR in the GHz range, a non-Gaussian $\frac{5}{2}$ -parabolic profile given by Eq. (3.9) is adopted.

The resulting spectral energy distributions and peak powers, radiated in distinct frequency bands, are summarised in Fig. 3.29 and Table 3.2, respectively. In the latter case, when a frequency is given, a frequency range $[0.96 \cdot \text{Freq}; 1.04 \cdot \text{Freq}]$ is meant, over which the total radiated power is integrated. The peak power is calculated under the assumption that a shape of the instantaneous power is an exact copy of the bunch profile. As peak powers can be accurately measured down to the few tens of microWatts, both ions and protons bunch spectra could be measured at least up to 10GHz with ChDR diagnostic.

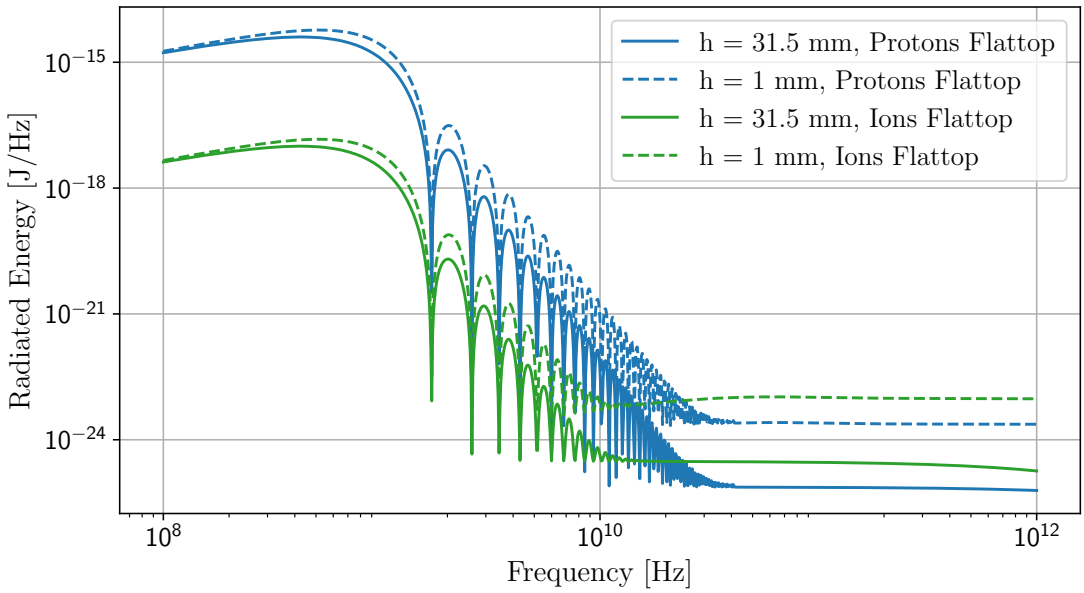

Figure 3.29: Spectral distribution of energy radiated by a non-Gaussian bunch.

3.5.3 Electron-Cloud Mitigation

One of the limiting factors in LHC performance, which can lead to instability and excessive heat load, is the creation of electron clouds inside the beam pipe [143]. One of the ways to mitigate this effect is to coat the inner walls of the beam pipe with an amorphous carbon (a-C) layer [144]. Such a coating characterises with a low secondary electron yield and therefore decreases the probability of the electron cloud build-up.

When using a Cherenkov diffraction radiator, the presence of secondary electrons at the surface

Table 3.2: Peak power emitted by a single non-Gaussian bunch

Freq [GHz]	Pb/1 mm P_p [W]	Pb/31.5 mm P_p [W]	p/1 mm P_p [W]	p/31.5 mm P_p [W]
1	$8.4 \cdot 10^{-1}$	$3.9 \cdot 10^{-1}$	$3.4 \cdot 10^{2}$	$1.6 \cdot 10^{2}$
3	$3.1 \cdot 10^{-3}$	$5.5 \cdot 10^{-4}$	$1.2 \cdot 10^{0}$	$2.2 \cdot 10^{-1}$
10	$1.0 \cdot 10^{-5}$	$6.2 \cdot 10^{-7}$	$1.4 \cdot 10^{-3}$	$8.6 \cdot 10^{-5}$
36	$4.7 \cdot 10^{-5}$	$1.4 \cdot 10^{-6}$	$1.3 \cdot 10^{-5}$	$4.0 \cdot 10^{-7}$
100	$1.4 \cdot 10^{-4}$	$3.9 \cdot 10^{-6}$	$3.3 \cdot 10^{-5}$	$9.8 \cdot 10^{-7}$

of the dielectric would be a risk both to build up the e-cloud but also to charge up the dielectric. Therefore, it is important to know whether low resistivity coatings can be used to mitigate this effect without significantly reducing the radiation power.

Such an analysis cannot be performed with the PCA model, as it describes only one-layer structures. An alternative approach was proposed in Section 3.4, where the ChDR was modelled for infinitely long multilayer cylindrical or flat geometries. Using this method, one can calculate the ChDR radiation suppression due to the presence of a thin 0.5 μm a-C layer on top of the dielectric placed within the beam pipe in the case of protons at flat top energy. As for adhesion purposes, a-C is sometimes coated on an intermediate 100 nm titanium layer, this case is also simulated. The thickness and electrical properties of the layers follow those reported in Ref. [145].

As shown in Fig. 3.30, in the sub-THz range the sole presence of the a-C coating does not lead to signal suppression stronger than 10%. The addition of an intermediate layer of titanium has a significant impact and reduces the radiation yield to 1.5% of the original value. Experimental validations of such an effect are foreseen to validate predictions of what coating to choose.

3.5.4 Beam Halo

In high-intensity rings such as LHC, outside the densely populated bunch core, a small fraction of particles acquire significantly high transverse energy, which results in the creation of the beam halo. In the context of ChDR diagnostics, estimating the impact of the halo population is especially interesting, as the radiation yield strongly increases if a particle shifts closer to the radiator. Under certain conditions, the tails of the transverse bunch distribution would dominate the signal emitted at well-defined wavelengths, providing thus a measurement of the tail population.

In order to study the effect of the halo on the ChDR spectral density, the assumption is made that the transverse profile of the bunch is a sum of two Gaussian distributions. The main core bunch of intensity $N = 1.15 \cdot 10^{11}$ can be characterised with a transverse standard deviation $\sigma_{core} = 0.25$

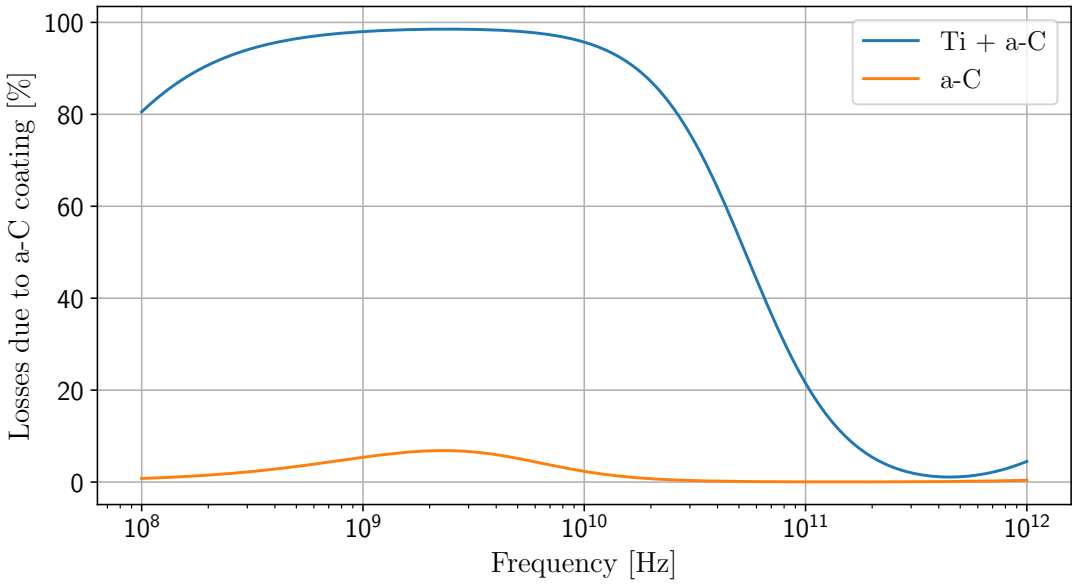

Figure 3.30: Signal reduction due to the presence of a-C coating.

mm, while the low-intensity halo Gaussian has $\sigma_{halo} = 0.5$ mm. In addition, it is assumed that, due to the collimators, no particles are present further than 1.25 mm from the centre of the bunch. These assumptions are presented graphically in Fig. 3.31, overscaled for illustrative purpose.

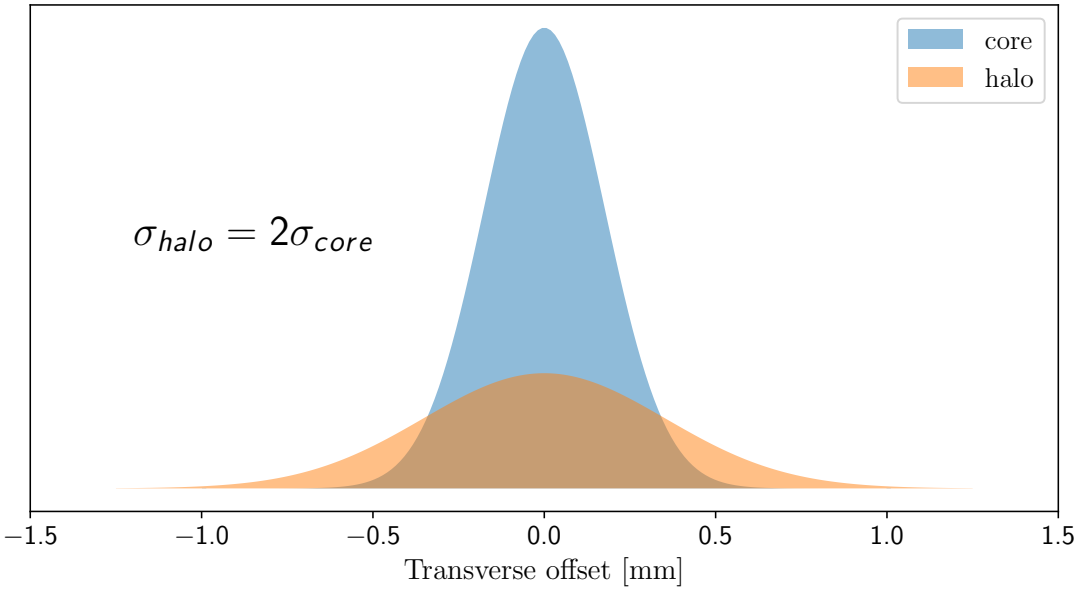

Figure 3.31: Schematic LHC bunch consisting of the highly populated core and low intensity halo.

One can now observe how the ChDR intensity varies with the change of beam halo population.

For that we assume that the radiator is placed 1.5 mm from the centre of the beam, which can be achieved if it is embedded in a collimator. As can be seen in Fig. 3.32, if measuring wavelengths in 570-630 nm band, the radiation from the core dominates and the halo population has no impact on the intensity of the radiation, if the intensity remains below 1% of the intensity of the core. From the shape of the radiation spectral distribution (Fig. 3.28) it can be deduced that the same will hold for higher wavelengths. However, if one considers the extreme ultraviolet band, it can be observed that the radiation intensity becomes proportional to the halo intensity after it exceeds approximately 10^{-5} of the core population. Having in mind that the High-Luminosity LHC upgrade design report [146] states the need to resolve the tails of 10^{-5} with respect to the core, ChDR diagnostics might be investigated as a potential halo measurement technique.

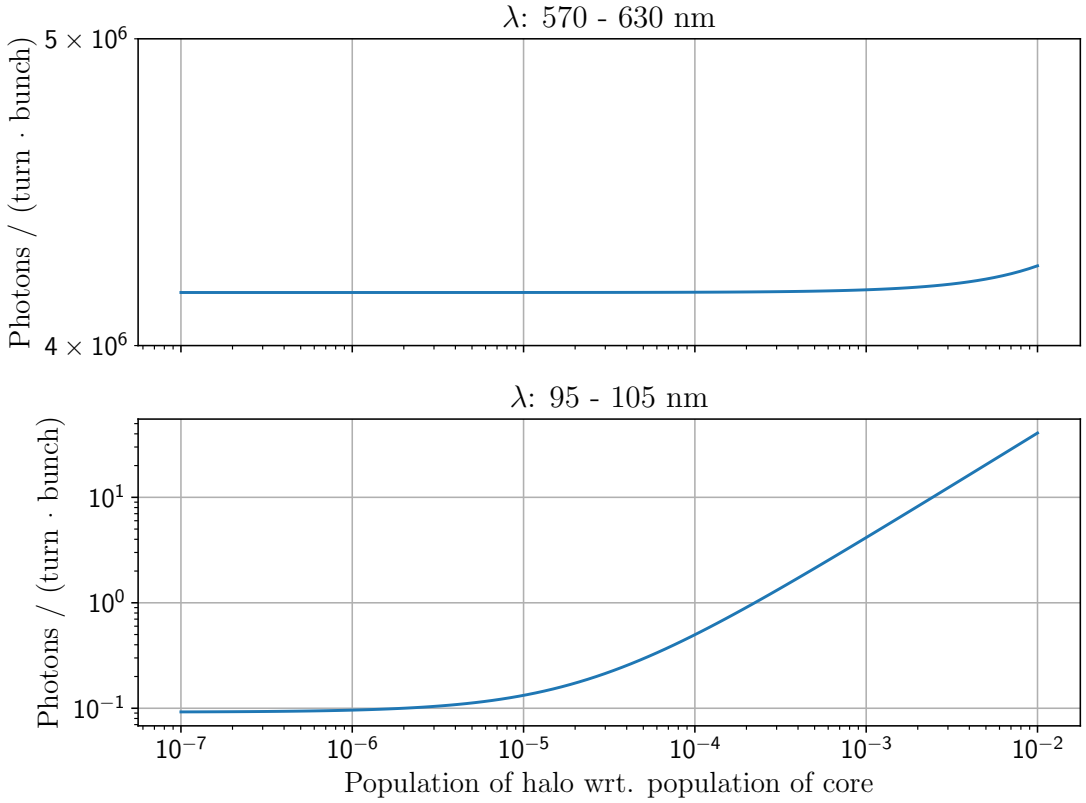

Figure 3.32: Number of photons emitted in orange color wavelength range (top plot) and extreme ultraviolet (bottom plot) frequency range, as a function of the relative halo population.

3.6 Experimental Verification of ChDR Models

As discussed in Section 3.2, the described stationary and non-stationary models of ChDR are compatible only at frequencies below the $\frac{c}{h}$ threshold, where c is the velocity of light and h is the impact parameter. The difference between the predictions of both models then grows with frequency, reaching the maximum approximately at a frequency equal to $\frac{c\gamma}{h}$.

In most of the so-far reported studies on ChDR, the focus is set on the low-frequency coherent part of the ChDR spectrum and low impact parameters, in order to maximise the radiation yield. Under such conditions, predictions of both theories are alike and their verification is not possible. On the other hand, observation of high-frequency incoherent signal is linked with various technical challenges, high level of the background noise and very small photon yield, which makes the quantitative verification of the theory difficult.

Answering the question of which model describes the reality is, however, very important in the context of beam diagnostics. Recent investigations determined the observation of incoherent high-frequency ChDR as a promising candidate for a diagnostic tool in the next generation of high-energy particle colliders, such as Compact Linear Collider (CLIC) or the Future Circular electron-positron Collider (FCC-ee) [147]. Taking the nominal 35 mm radius of the FCC beam pipe as the impact parameter and the beam energy of 45 GeV, what corresponds to the nominal FCC-ee beam energy during Z operation, stationary and non-stationary predictions of the ChDR yield in the visible range differ by over six orders of magnitude.

This section describes an experiment designed by the author of this thesis and conducted at CERN's CLEAR facility by himself and his colleagues from the CERN Beam Instrumentation Group. The aim of the experiment was to determine whether stationary or non-stationary models better describe the ChDR emitted in a configuration typical for beam diagnostics.

3.6.1 Verification Principles

The experiment relied on the observation, discussed previously in subsection 3.3.1, that the intensity of ChDR of a given wavelength λ scales differently with the change of the impact parameter according to each model. For impact parameters in the range $\lambda < h < \gamma\lambda$ stationary models predict a h^{-3} dependence, while according to PCA the intensity is proportional to h^{-1}. Performing an *impact scan*, that is, measuring the radiation intensity while changing the impact parameter over a broad range within the $\lambda < h < \gamma\lambda$ limit, makes it possible to compare the shape of the experimentally obtained dependence to the theoretical predictions.

The radiation detection system from the previous study on ChDR beam position monitoring

[110] was reused for the verification experiment. The key component of this setup was a Ka-band RF diode, sensitive to radiation at frequencies between 26.5 and 40 GHz or equivalently wavelengths between 7 and 11.32 mm.

In the case of the CLEAR facility, the range of impact parameters that can be scanned for such radiation wavelength spans between approximately 1 - 100 mm. The lower limit is due to the transverse size of the beam, and at small impact parameters the tails of the bunch may penetrate the radiator emitting large amounts of the standard Cherenkov radiation. The upper bound was determined experimentally, as for larger distances ChDR intensity was negligible. Most importantly, for nominal CLEAR energy corresponding to $\gamma = 392$ and Ka-wavelengths, the intersection of the 1 - 100 mm range with $\lambda < h < \gamma\lambda$ spans between approximately 1 and 10 cm.

Theoretical predictions of the radiation power given as a function of impact parameter are shown in Fig. 3.33, for nominal CLEAR energy, 36 GHz frequency, and an impact parameter between 1 and 10 cm. It confirms that the conditions at CLEAR are suitable for the verification of the validity of the discussed ChDR theories.

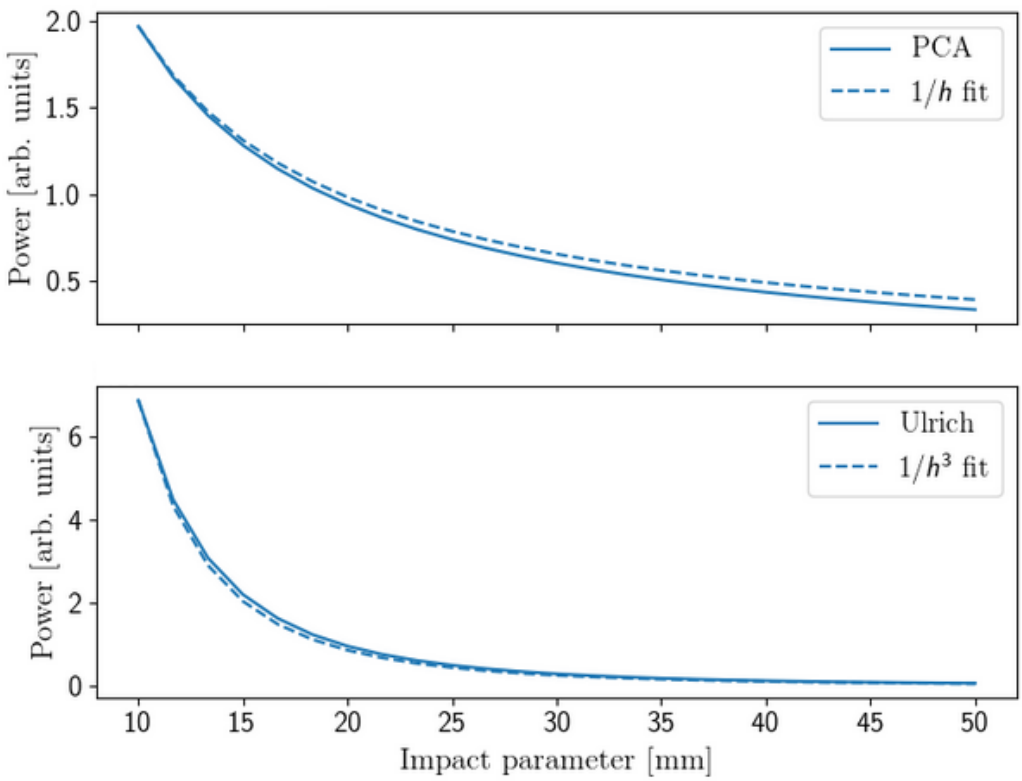

Figure 3.33: Radiation power as a function of impact parameter according to Ulrich and PCA models.

A great advantage of the proposed approach is that the verification is based on relative, rather than absolute, measurements. Obtaining the absolute amount of the radiated energy is difficult for several reasons. Firstly, the sensitivity of RF diodes to short radiation pulses is not well studied yet. Secondly, at frequencies of interest, the radiation is not fully coherent, so that the absolute level of the radiation intensity strongly depends on the bunch profile. Finally, relative measurement allows one to disregard all the attenuation effects and losses, as long as one can ensure that these are not position dependent.

3.6.2 Experimental Setup

The radiator used in the experiment is presented in Fig. 3.34. It is a PTFE rod with a 10 cm diameter and 10 cm length, cut at 45 degrees. The refractive index of PTFE in the 26.5-40 GHz range is close to $\sqrt{2}$, so that for a highly relativistic beam one has

$$\theta_{ChDR} = \arccos \frac{1}{n\beta} \approx 45^{\circ}.$$

The particle beam, passing in front of the ellipsoidal cross section, induces ChDR propagating within the radiator. The radiation wave hits the back face of the radiator at the right angle and transmits into the air.

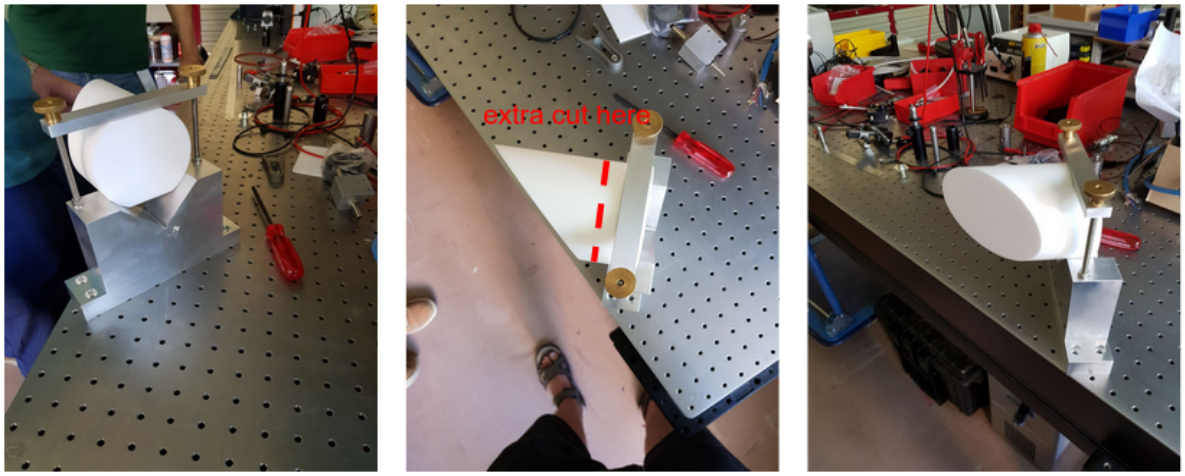

Figure 3.34: PTFE Radiator used for experimental verification of ChDR models.

The size of the radiator was chosen considering that the theory discussed in Section 3.2 assumed an infinite transverse radiator size. As in a real case this assumption cannot be fulfilled, one needs to ensure that only a negligible part of the total ChDR yield was supposed to transfer through the non-existing part of the radiator. The energy flow map can be created using the IW2D framework,

as presented in Fig. 3.35 for two different impact parameters. It was verified that according to IW2D, for impact parameters below 5 cm a dominant part of the radiated energy is confined within the central 10 cm of the radiator.

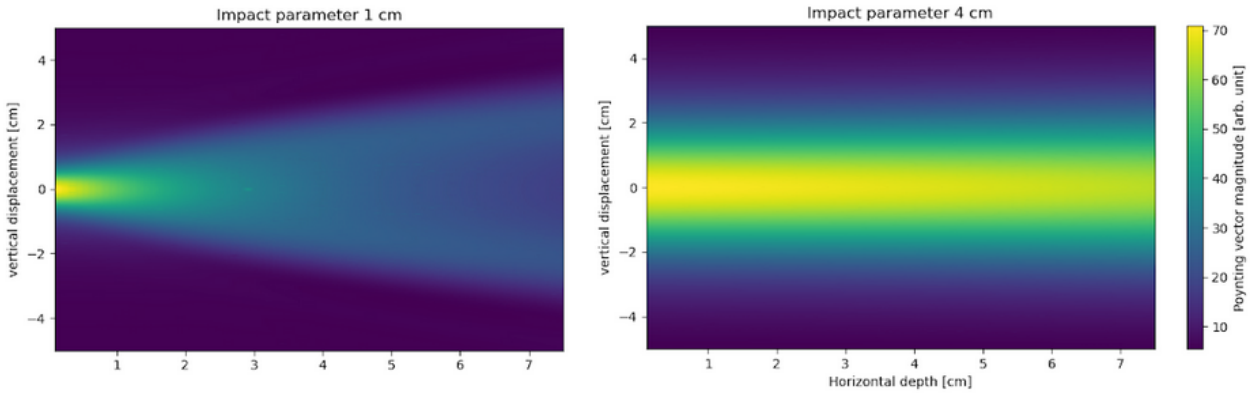

Figure 3.35: 36 GHz ChDR energy flow within the PTFE radiator, induced by 200 MeV electron beam.

The radiator was placed in an aluminium box in such a way that only the front face is visible, as can be seen in Fig. 3.36. The purpose of the box was to shield the radiator and the acquisition system from possible background noise. In addition, the internal walls of the box were covered with RF-absorbing foam. The setup was placed in the last section of the CLEAR accelerator beamline, in the so-called *in-air test stand*. The particles left the beam pipe and traveled in air approximately 1 meter, until they hit a lead target in the beam dump. The aluminium box with the radiator and the acquisition system was placed on a movable horizontal linear stage, which allowed changing the distance between the front face of the radiator and the beam in the 0.7 - 11 cm range.

The fact that particles travel through air before they induce ChDR in the radiator could have a significant impact on the background level. The relative permittivity of air is small, but higher than the vacuum permittivity. As a result, highly relativistic particles emit Cherenkov radiation, which can couple into the radiator and propagate to the acquisition system. On the other hand, the Cherenkov angle for air is very small. For the refractive index of air, $n_{\text{air}} \approx 1.0006$, one has

$$\theta_{ChR_{air}} = \arccos \frac{1}{n_{air}\beta} \approx 1.4^\circ \implies \tan\theta_{ChR_{air}} \approx 0.0245.$$

As a consequence, if a particle travels 50 cm through the air until it faces the radiator, the Cherenkov radiation propagation range in the transverse direction reaches approximately

$$50 \text{ cm} \cdot \tan\theta_{ChR_{air}} \approx 1.225 \text{ cm}.$$

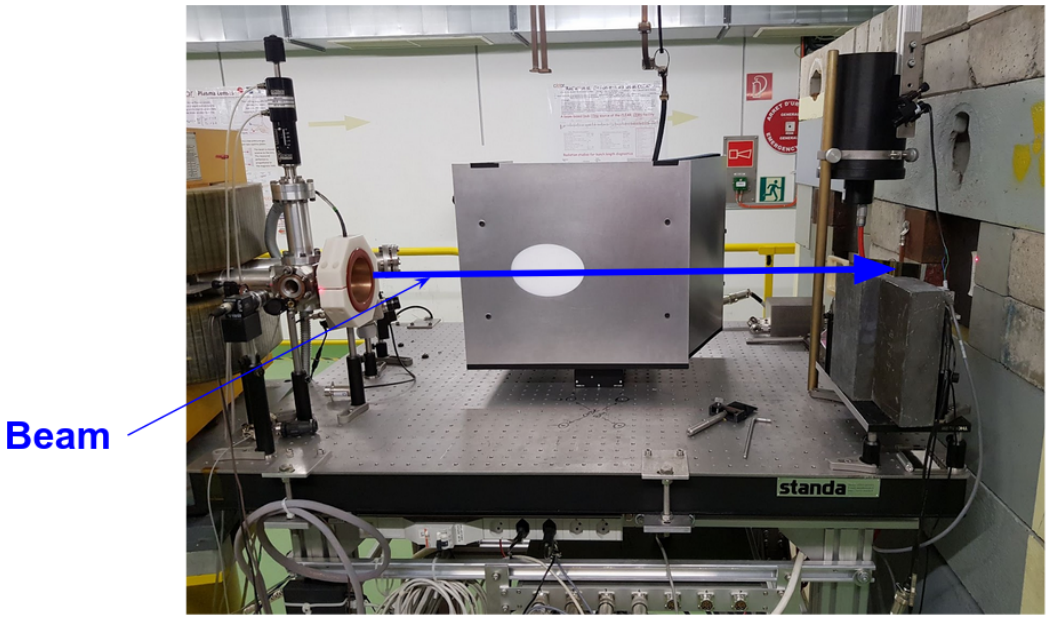

Figure 3.36: Experimental setup for the verification of ChDR theory.

Starting the impact parameter scan from a 2 cm distance between the beam and radiator should therefore exclude any potential contribution from the in-air Cherenkov radiation.

The first element of the acquisition system, as shown in Fig. 3.37, was a horn antenna located behind the back face of the radiator. The captured signal was then filtered using a narrow band-pass filter. Two filters were used during the experiment, one centred at 30 GHz with 300 MHz bandwidth, and other at 36 GHz with 1 GHz bandwidth. The filtered signal was guided through a system of W28 waveguides to the technical gallery, where the rest of the acquisition system was located. As the first section of the acquisition system moved with the radiator during the impact parameter scan, the waveguide connecting to the mentioned W28 waveguides was flexible. Using a signal generator, the waveguide system attenuation was verified to be independent of the setup position.

The sensitivity of a typical RF diode is not constant but depends on the input power. At low input powers, the output voltage is proportional to the input power. On the other hand, if the input power is high, the output voltage is proportional to the square root of the power. In order to avoid working in both of these regimes, the signal received at each impact parameter step was attenuated before reaching the RF diode. A manual attenuator was set so that at each impact parameter step the diode output voltage was kept at a constant level, at which the sensitivity is known to be linear. The actual input power can therefore be calculated on the basis of the RF diode output voltage and the attenuator settings. At the last step, the signal was amplified and digitised with an oscilloscope.

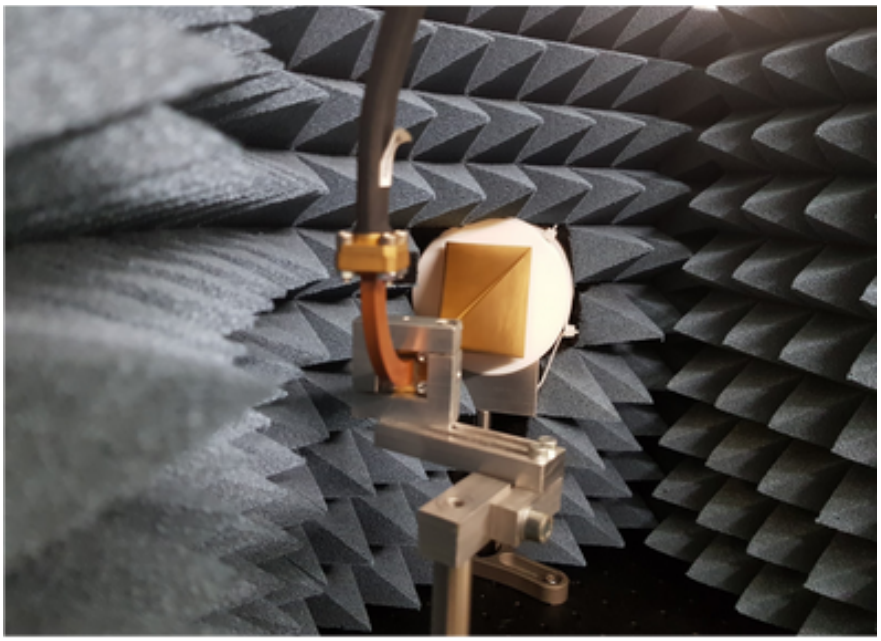

Figure 3.37: Initial part of the signal acquisition system for the ChDR theory verification experiment.

The elements of the acquisition system present in the upper gallery are shown in Fig. 3.38.

3.6.3 Data Collection, Analysis and Results

Impact parameter scans were obtained in two separate time periods in September and November 2021. The beam conditions and experimental settings are listed in Table 3.3. During the first period, the measurements were taken at a single beam energy, but two different band-pass filters were used to probe signal at two distinct frequencies. The aim of the second experimental period was to study the impact of energy on the impact parameter curves and to repeat the experiment under more controlled conditions.

Table 3.3: Beam and experimental parameters during both sessions of the ChDR theory verification experiment

	September 2021	November 2021
Beam Energy	220 MeV	100, 150, 200 MeV
Frequency	30, 36 GHz	36 GHz
Impact parameter	0.8-11 cm, 2 mm step	1-8 cm, 4 mm step
Acqs. per impact parameter	200	200
Additionally monitored	Charge	Charge, beam size & position

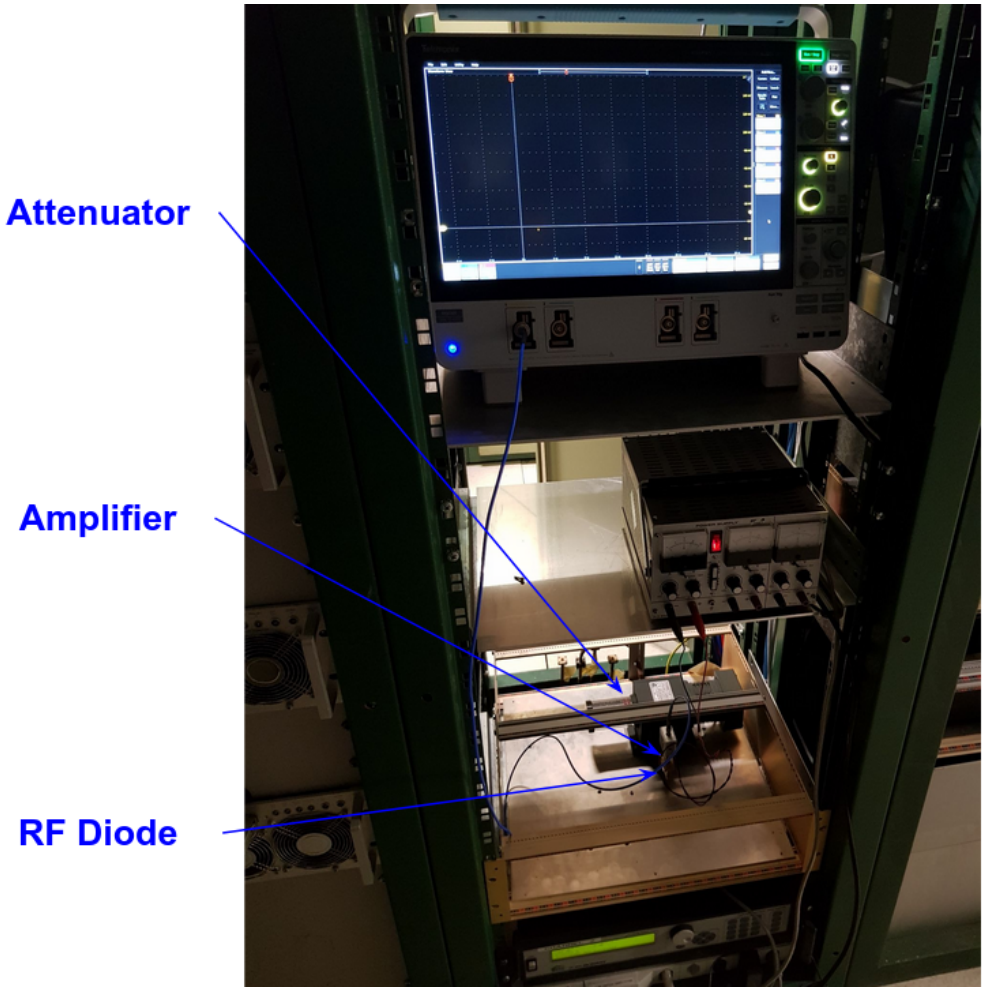

Figure 3.38: Final part of the signal acquisition system for the ChDR theory verification experiment.

During the experiment the CLEAR facility provided a bunched electron beam with 10 Hz repetition rate. The range of impact parameters was scanned in steps of either 2 or 4 mm. Starting from the closest position, the motor moved the radiator further away from the beam until the threshold of the impact parameter was reached or the signal was weaker than the noise level. At each step, the attenuator was manually set to ensure that the RF diode works in the linear regime, and then 200 consecutive signal acquisitions were taken with an oscilloscope.

As discussed in subsection 3.2.3, the power of coherent ChDR is proportional to the square of the total bunch charge. In CLEAR facility, stability of the bunch charge cannot be ensured for the entire duration of the impact parameter scan. As for the purpose of ChDR theory verification the power radiated by a single electron is desired, the charge has to be monitored in order to normalise the measured power of the whole bunch.

During the September experimental session, the ratio between the measured ChDR power and

the squared charge of the bunch was estimated at each impact parameter based on 200 ChDR and charge acquisitions, using linear regression. The results for the measured ratio are presented in Fig. 3.39. As a reference, the theoretical h^{-1} and h^{-3} curves are plotted with a scaling factor determined by the least squares fit to the data. As can be seen, at both frequencies the measurement deviates significantly from these predictions. On the other hand, the measurement fits perfectly with an exponential curve, which is not predicted by any of the models discussed in Section 3.2. If one parameterizes the exponential curve as ae^{-bh}, the values of b parameter obtained with least squares methods are

$$b_{30\text{ GHz}} = 58.58\text{ m}^{-1}, \quad b_{36\text{ GHz}} = 72.52\text{ m}^{-1},$$

which suggests that the value of the parameter b increases with the frequency.

As discussed, the impact parameters below 2 and above 5 cm should not be taken into account for the analysis, due to possible contribution of in-air Cherenkov radiation and the insufficient transverse size of the radiator, respectively. Nevertheless, it is worth noting that the same shape of the impact parameter curve is preserved over the whole scanned range, as can be seen in Fig. 3.40. In the case of 30 GHz radiation the measurements were stopped at an impact parameter equal to 8.2 cm, as at higher impact parameters the signal was dominated by noise. However, this does not mean that the radiation is stronger at 36 GHz, other parameters which have an impact on the absolute power of ChDR power, such as the bunch charge or the bunch length, were not equal during both scans.

The same procedure has been repeated in November 2021 with the beam at three distinct beam energies. This time the beam size and position oscillations were also monitored. Although the position of the motor still determined the impact parameter to a large extent, introducing small corrections corresponding to the beam position offset and transverse position spread resulted in a more precise measurement. Unfortunately, the bunch size and position measurements were updated with a 1 Hz rate, meaning that the values corresponding to the individual bunch had to be interpolated. Due to time constraints, the impact parameter step was increased to 4 mm and only the 36 GHz filter was used. The impact parameter scan was performed twice at the following beam energies: 100 MeV, 150 MeV and 200 MeV.

The results of the impact parameter scans, with the least squares fits of the appropriate theoretical curves, are presented in Fig. 3.41, where error bars are replaced with blue dots due to the measured beam position oscillations. It confirms that the impact parameter curve follows an exponential shape. In addition, the parameter b of the parametrisation of the exponential curve, ae^{-bh}, is within $64.1 - 72.6\text{ m}^{-1}$ for all scans and seems to be independent of the beam energy. Finally, the

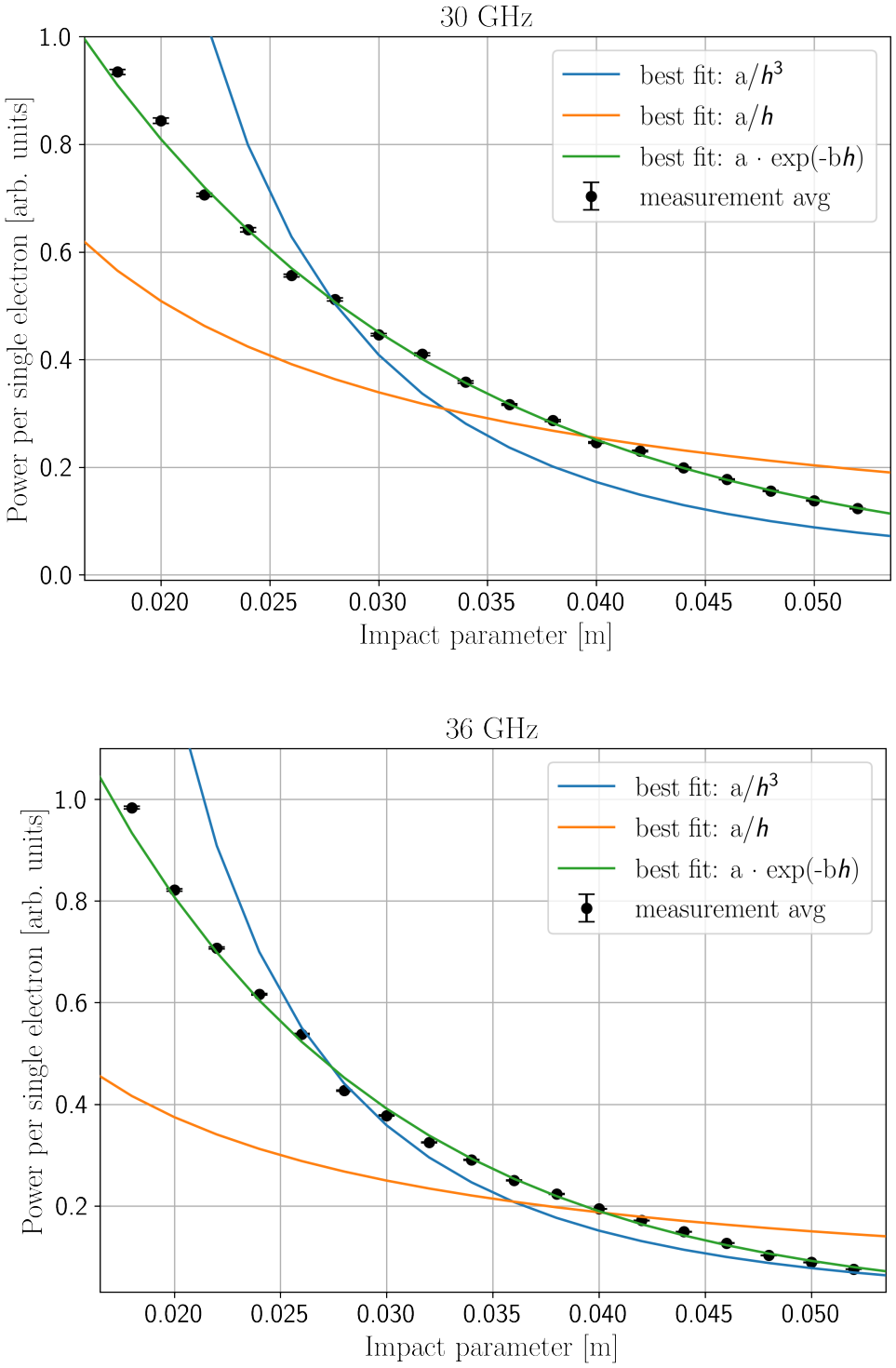

Figure 3.39: Impact parameter scans obtained in September period of ChDR theory verification experiment.

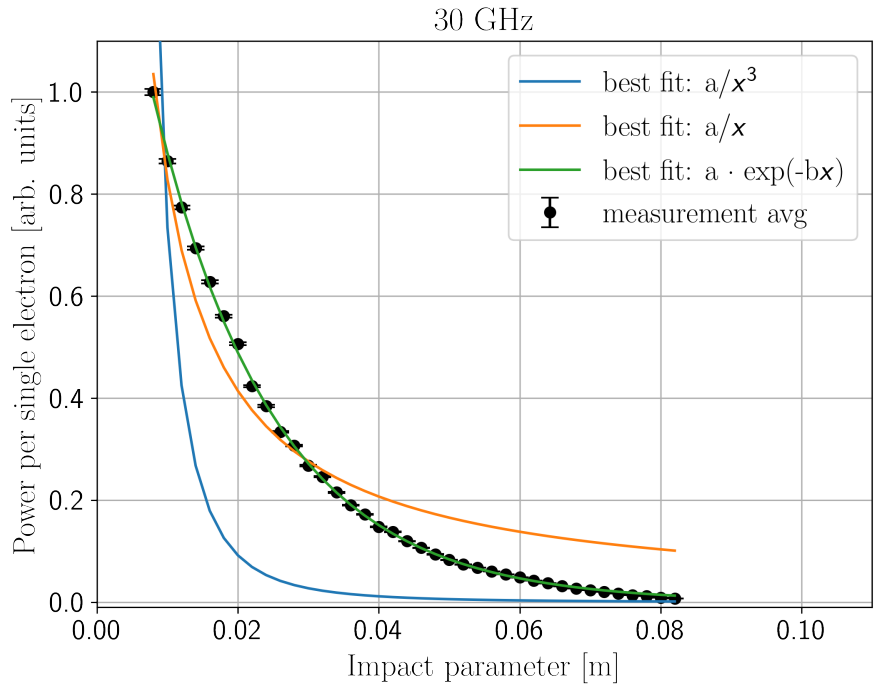

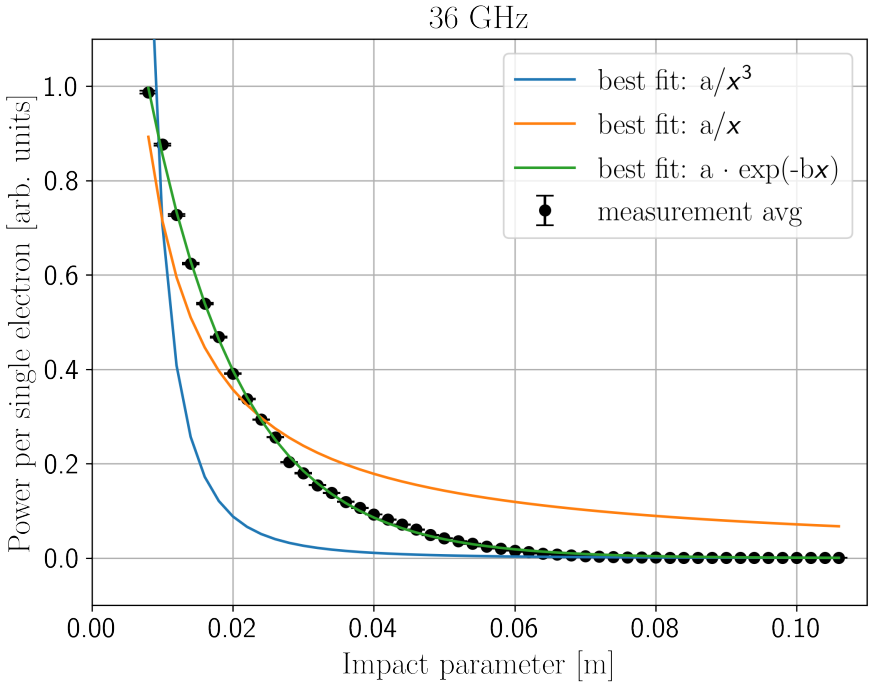

Figure 3.40: Impact parameter scans obtained in September period of ChDR theory verification experiment, broad impact parameter range.

same results hold for the extended scan covering 1-8 cm impact parameter range.

3.6.4 Discussion on the Results

The results of the experiment did not support the theoretical results discussed in Section 3.2. The measurements, repeated systematically for various beam conditions, proved that the ChDR power in the intermediate $\lambda < h < \gamma\lambda$ impact parameter range is given as an exponential function of the impact parameter.

The exponential dependence was previously observed in Refs. [110, 116] in a narrow range of impact parameters of magnitude comparable to the radiation wavelength. In [127] it was postulated that the amount of energy radiated in the form of ChDR is proportional to $e^{-4\pi h/\beta\gamma\lambda}$. This dependence was confirmed during the observation of incoherent ChDR in Ref. [54], but it does not match neither the findings of Ref. [110] nor the results of the experiment described in this section. Assuming, as suggested, that the exponential b parameter is given by $b = 4\pi/\beta\gamma\lambda$, the experimental settings would result in $b_{30\text{ GHz}} \approx 3.85$ m^{-1}, which is over one order of magnitude smaller than what was determined experimentally. Furthermore, as determined during the November experimental session, the b parameter does not depend on the beam energy.

One might then suspect that the $e^{-4\pi h/\beta\gamma\lambda}$ dependence holds in the high frequency limit $\lambda\gamma \sim h$ but is not valid for lower frequencies. The exponential shape of the impact parameter curve in the high frequency limit is also predicted by the theory described in Section 3.2, as can be deduced from Figs. 3.10 to 3.12.

At this stage, the author cannot give a conclusive answer to the question why none of the tested hypotheses match the experimental results. A possible explanation might be the impact of the radiator size, verified to be sufficient only based on the stationary analytical model. However, the study performed with such a radiator is more relevant to the actual needs of beam instrumentation. The experimental results presented, although they might not correspond to the idealised geometries of theoretical models, could serve as a reference for future designs of diagnostic devices based on Cherenkov diffraction radiation.

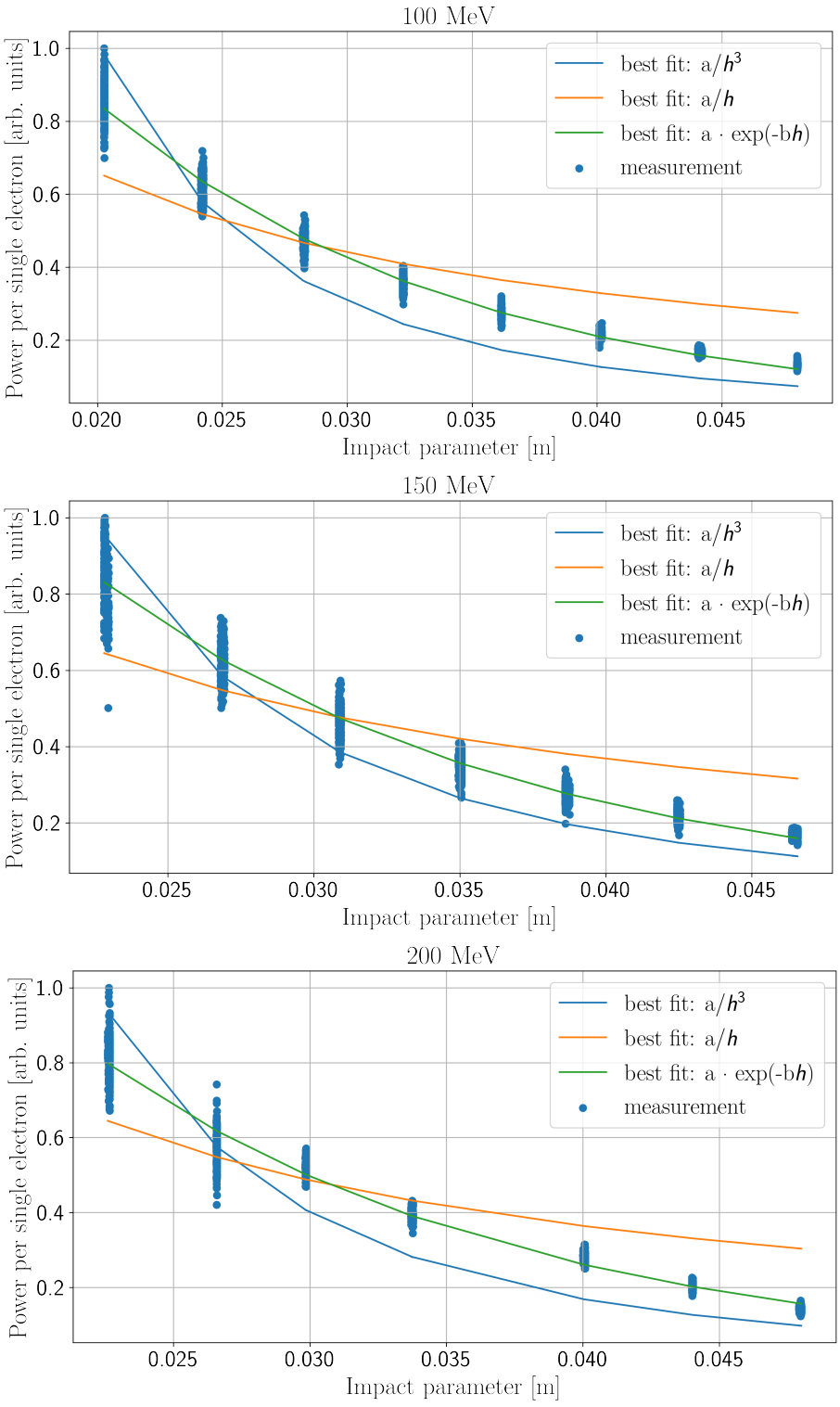

Figure 3.41: Impact parameter scans obtained in November period of ChDR theory verification experiment.

3.7 Summary

The second part of this dissertation was devoted to the properties of Cherenkov diffraction radiation, with an emphasis on how the radiation characteristics depend on various beam parameters.

The chapter has begun with a presentation of theoretical formulas describing the emission of ChDR in various geometrical configurations. In addition, the relationship between the longitudinal bunch profile and radiation intensity has been discussed, introducing the concepts of coherent and incoherent radiation.

Subsequently, the impact of the most relevant beam characteristics on ChDR has been systematically discussed. This analysis was not limited to any particular range of radiation wavelengths but considered the whole EM radiation spectrum. The conclusions of the practical importance for beam diagnostics have been supported with numerous examples of ChDR spectral energy distributions at various beam-radiator configurations.

In the next part of the chapter, a new framework for estimating ChDR was presented. Although the presented procedure describes radiators infinite in the direction of beam propagation, it gives the possibility of studying complex multilayer structures orthogonal to the direction of beam propagation. It allows investigating ChDR emitted in the case of coated radiators, deposited either to reshape the radiation spectrum or as a machine protection measure.

On the basis of the discussed theory and the new proposed method, feasibility of a ChDR-based diagnostic system in the LHC has been assessed. Apart from calculation of the expected radiation yield and identifying frequency ranges most suitable for diagnostic purposes, the problem of the impact of beam halo on ChDR has been addressed.

The last part of the chapter reported on the experimental verification of the validity of previously used ChDR theoretical models for beam diagnostic purposes. The results of the experiment, diverging from the theoretical prediction in the intermediate frequency range, suggest that special attention should be paid to the impact of the radiator size on the emitted ChDR and motivate further theoretical and experimental studies.

REFERENCES

[1] E. Rutherford, "Address of the President, Sir Ernest Rutherford, O. M., at the Anniversary Meeting, November 30, 1927," *Proceedings of the Royal Society of London, Series A*, vol. 117, no. 777, 1928. https://doi.org/10.1098/rspa.1928.0001

[2] R. J. Van de Graaff, K. T. Compton, and L. C. Van Atta, "The electrostatic production of high voltage for nuclear investigations," *Phys. Rev.*, vol. 43, pp. 149–157, Feb 1933. https://link.aps.org/doi/10.1103/PhysRev.43.149

[3] J. D. Cockcroft, E. T. S. Walton, and E. Rutherford, "Experiments with high velocity positive ions. further developments in the method of obtaining high velocity positive ions," *Proceedings of the Royal Society of London, Series A*, vol. 136, no. 830, 1932. https://doi.org/10.1098/rspa.1932.0107

[4] D. W. Kerst, "The acceleration of electrons by magnetic induction," *Phys. Rev.*, vol. 60, Jul 1941. https://doi.org/10.1103/PhysRev.60.47

[5] E. O. Lawrence and M. S. Livingston, "The production of high speed light ions without the use of high voltages," *Phys. Rev.*, vol. 40, Apr 1932. https://doi.org/10.1103/PhysRev.40.19

[6] G. Ising, "Prinzip einer Methode zur Herstellung von Kanalstrahlen hoher Voltzahl," *Ark. Mat. Astron. Fys.*, vol. 18, 1924. https://cds.cern.ch/record/433984

[7] R. Wideröe, "Über ein neues Prinzip zur Herstellung hoher Spannungen," *Arch. Elektrotech.*, vol. 21, no. 4, 1928. https://doi.org/10.1007/BF01656341

[8] O. S. Brüning *et al.*, *LHC Design Report*, CERN Yellow Reports: Monographs. Geneva: CERN, 2004. https://cds.cern.ch/record/782076

[9] M. Steiner *et al.*, "Preliminary measurements of SIS 18 beam parameters," *Nuclear Instruments and Methods in Physics Research Section A*, vol. 312, no. 3, 1992. https://doi.org/10.1016/0168-9002(92)90190-F

[10] *Conceptual design of the Relativistic Heavy Ion Collider (RHIC).* Upton: Brookhaven Nat. Lab., 1986. https://cds.cern.ch/record/108613

[11] *Design Report Tevatron 1 Project.* Batavia: Fermilab, Oct 1982. https://doi.org/10.2172/1413194

[12] W. K. H. Panofsky, "Evolution of particle accelerators and colliders," *SLAC Beam Line*, vol. 27N1, 1999. https://inspirehep.net/literature/457728

[13] J. Hémery and S. Maury, "The Antiproton Decelerator: Overview," *Nuclear Physics A*, vol. 655, no. 1, 1999. https://doi.org/10.1016/S0375-9474(99)00223-7

[14] W. Oelert, "The ELENA Project at CERN," *Acta Physica Polonica B*, vol. 46, no. 1, 2015. http://dx.doi.org/10.5506/APhysPolB.46.181

[15] G. I. Budker, "An effective method of damping particle oscillations in proton and anti-proton storage rings," *Sov. Atom. Energ.*, vol. 22, 1967. https://doi.org/10.1007/BF01175204

[16] J. Marriner, "Stochastic cooling overview," *Nuclear Instruments and Methods in Physics Research Section A*, vol. 532, no. 1, 2004. https://doi.org/10.1016/j.nima.2004.06.025

[17] D. Reggiani *et al.*, "Improving Machine and Target Protection in the SINQ Beam Line at PSI-HIPA," *Proc. 9th International Particle Accelerator Conference*. http://doi.org/10.18429/JACoW-IPAC2018-WEPAL068

[18] J. Thomason, "The ISIS Spallation Neutron and Muon Source — The first thirty-three years," *Nuclear Instruments and Methods in Physics Research Section A*, vol. 917, 2019. https://doi.org/10.1016/j.nima.2018.11.129

[19] M. Plum, "SNS machine status report," *Nuclear Physics B - Proceedings Supplements*, vol. 154, no. 1, 2006. https://doi.org/10.1016/j.nuclphysbps.2006.01.057

[20] R. Garoby, "Progress on the ESS Project Construction," *Proc. 8th International Particle Accelerator Conference*. https://doi.org/10.18429/JACoW-IPAC2017-MOXBA1

[21] T. Abe *et al.*, "Belle II Technical Design Report," 2010, arXiv preprint. https://doi.org/10.48550/arXiv.1011.0352

[22] D. M. Asner *et al.*, "Physics at BES-III," Sep. 2008, arXiv preprint. https://doi.org/10.48550/arXiv.0809.1869

[23] F. Willeke, "HERA status and perspectives of future lepton hadron colliders," *Proc. 8th European Particle Accelerator Conference*, Jun 2002. https://cds.cern.ch/record/580908

[24] E. C. Aschenauer *et al.*, "eRHIC Design Study: An Electron-Ion Collider at BNL," 2014, arXiv preprint. https://doi.org/10.48550/arXiv.1409.1633

[25] J. M. Jowett, "The LHC as a nucleus–nucleus collider," *Journal of Physics G: Nuclear and Particle Physics*, vol. 35, no. 10, p. 104028, sep 2008. https://doi.org/10.1088/0954-3899/35/10/104028

[26] K. Akai, K. Furukawa, and H. Koiso, "SuperKEKB collider," *Nuclear Instruments and Methods in Physics Research Section A*, vol. 907, 2018. https://doi.org/10.1016/j.nima.2018.08.017

[27] C. Zhang and G. Pei, "BEPC II-The Second Phase Construction of Beijing Electron Positron Collider," *Proc. 21st IEEE Particle Accelerator Conference*, 2005. https://doi.org/10.1109/PAC.2005.1590381

[28] C. Joshi *et al.*, "Ultrahigh gradient particle acceleration by intense laser-driven plasma density waves," *Nature*, vol. 311, no. 5986, Oct. 1984. https://doi.org/10.1038/311525a0

[29] C. Jing, "Dielectric wakefield accelerators," *Reviews of Accelerator Science and Technology*, vol. 09, 2016. https://doi.org/10.1142/S1793626816300061

[30] T. Plettner, P. P. Lu, and R. L. Byer, "Proposed few-optical cycle laser-driven particle accelerator structure," *Phys. Rev. ST Accel. Beams*, vol. 9, p. 111301, Nov 2006. https://doi.org/10.1103/PhysRevSTAB.9.111301

[31] E. A. Peralta *et al.*, "Demonstration of electron acceleration in a laser-driven dielectric microstructure," *Nature*, vol. 503, 2013. https://doi.org/10.1038/nature12664

[32] S. White *et al.*, "Commissioning and Restart of ESRF-EBS," *Proc. 12th International Particle Accelerator Conference*, Aug 2021. https://doi.org/10.18429/JACoW-IPAC2021-MOXA01

[33] M. Bieler *et al.*, "PETRA III Operation," *Proc. 8th International Particle Accelerator Conference*, May 2017. https://doi.org/10.18429/JACoW-IPAC2017-WEPAB014

[34] R. Walker, "Progress with the Diamond light source project," *Proc. 2003 Particle Accelerator Conference*, vol. 1, 2003. https://cds.cern.ch/record/748852

[35] S. Asaoka *et al.*, "Status report on the KEK photon factory," *Proc. 2nd Asian Particle Accelerator Conference*, 2001. https://cds.cern.ch/record/581957

[36] M. Boge, "First operation of the Swiss Light Source," *Proc. 8th European Particle Accelerator Conference*, 6 2002. https://accelconf.web.cern.ch/e02/PAPERS/TUXLA001.pdf

[37] A. Wawrzyniak *et al.*, "First Results of Solaris Synchrotron Commissioning," *Proc. 4th International Beam Instrumentation Conference*, 2016. https://10.18429/JACoW-IBIC2015-WEDLA01

[38] D. A. Edwards and J. J. Syphers, *An introduction to the physics of high energy accelerators*. Wiley, 1993. https://doi.org/10.1002/9783527617272

[39] M. Conte and W. W. MacKay, *An Introduction to the Physics of Particle Accelerators*, 2nd ed. Singapur: World Scientific, 2008. https://doi.org/10.1142/6683

[40] R. J. Steinhagen, "Tune and chromaticity diagnostics," *Proc. CERN Accelerator School: Beam Diagnostics course*, 2009. https://cds.cern.ch/record/1213281

[41] A. Wolski, *Beam Dynamics in High Energy Particle Accelerators*. London: Imperial College Press, 2014. https://doi.org/10.1142/p899

[42] C. Bovet *et al.*, "LHC BPM design," *Proc. 3rd European Workshop on Beam Diagnostics and Instrumentation for Particle Accelerators*, Dec 1997. https://cds.cern.ch/record/343810

[43] D. Belohrad *et al.*, "The LHC Fast BCT system: A comparison of Design Parameters with Initial Performance," *Proc. 14th Beam Instrumentation Workshop*, May 2010. https://cds.cern.ch/record/1267400

[44] G. Papotti *et al.*, "Longitudinal Beam Measurements at the LHC: The LHC Beam Quality Monitor," *Proc. 2nd International Particle Accelerator Conference*, 2011. https://cds.cern.ch/record/1399087

[45] M. Betz *et al.*, "Bunched-beam Schottky monitoring in the LHC," *Nuclear Instruments and Methods in Physics Research Section A*, vol. 874, 2017. https://doi.org/10.1016/j.nima.2017.08.045

[46] J. Seguinot and T. Ypsilantis, "Photo-ionization and Cherenkov ring imaging," *Nuclear Instruments and Methods*, vol. 142, no. 3, 1977. https://doi.org/10.1016/0029-554X(77)90671-1

[47] I. Adam *et al.*, "DIRC, the internally reflecting ring imaging Cherenkov detector for BABAR," *IEEE Transactions on Nuclear Science*, vol. 45, no. 3, 1998. https://10.1109/23.682602

[48] S. Fukuda *et al.*, "The Super-Kamiokande detector," *Nuclear Instruments and Methods in Physics Research Section A*, vol. 501, no. 2, 2003. https://doi.org/10.1016/S0168-9002(03)00425-X

[49] M. Körfer, "Beam Loss Position Monitor Using Cerenkov Radiation in Optical Fibers," *Proc. 7th European Workshop on Beam Diagnostics and Instrumentation for Particle Accelerators*, 2005. https://cds.cern.ch/record/924165

[50] R. B. Fiorito and D. W. Rule, "Optical transition radiation beam emittance diagnostics," *AIP Conference Proceedings*, vol. 319, no. 1, 1994. https://doi.org/10.1063/1.46965

[51] F. Sakamoto *et al.*, "Development of the High Resolution Electron Beam Profile Monitor for Medical Use X-Band Linac," *Proc. 3rd Asian Particle Accelerator Conference*, Mar. 2004. https://jacow.org/a04/papers/TUP11020.pdf

[52] B. Bolzon *et al.*, "Very high resolution optical transition radiation imaging system: Comparison between simulation and experiment," *Phys. Rev. Spec. Top. Accel. Beams*, vol. 18, p. 082803, Oct 2015. https://cds.cern.ch/record/2120825

[53] P. Karataev *et al.*, "Beam-Size Measurement with Optical Diffraction Radiation at KEK Accelerator Test Facility," *Phys. Rev. Lett.*, vol. 93, p. 244802, Dec 2004. https://doi.org/10.1103/PhysRevLett.93.244802

[54] R. Kieffer *et al.*, "Optical diffraction radiation for position monitoring of charged particle beams," *Nuclear Instruments and Methods in Physics Research Section B*, vol. 402, 2017. https://doi.org/10.1016/j.nimb.2017.03.089

[55] G. Kube, "Smith-Purcell Radiation in View of Particle Beam Diagnostics," *Proc. 6th European Workshop on Beam Diagnostics and Instrumentation for Particle Accelerators*, 2003. https://cds.cern.ch/record/923929

[56] T. Lefèvre *et al.*, "Cherenkov diffraction radiation as a tool for beam diagnostics," *Proc. 8th International Beam Instrumentation Conference*, Nov 2019. https://doi.org/10.18429/JACoW-IBIC2019-THAO01

[57] J. Emery *et al.*, "A fast and accurate wire scanner instrument for the CERN accelerators to cope with severe environmental constraints and an increased demand for availability," *2014 IEEE Conference on Control Applications*, 2014. https://10.1109/CCA.2014.6981482

[58] R. Jones, "Beam Diagnostics Examples from High Energy Colliders," *Proc. CERN Accelerator School: Beam Instrumentation course*, Jun 2018. https://cds.cern.ch/record/2723991

[59] T. Böhlen *et al.*, "First Experience with the LHC Beam Loss Monitoring System," *Proc. 2009 Particle Accelerator Conference*, May 2009. https://cds.cern.ch/record/1206505

[60] O. S. Brüning *et al.*, "Chromaticity Measurements via RF Phase Modulation and Continuous Tune Tracking," *Proc. 8th European Particle Accelerator Conference*, Jun 2002. https://cds.cern.ch/record/563396

[61] P. Forck *et al.*, "Tutorial on Beam Measurements using Schottky Signal Analysis," *Proc. 6th International Beam Instrumentation Conference*, 08 2017. https://accelconf.web.cern.ch/ibic2017/talks/mo2ab1_talk.pdf

[62] T. Tydecks *et al.*, "Status of the LHC Schottky Monitors," *Proc. 9th International Particle Accelerator Conference*, no. 9, June 2018, https://doi.org/10.18429/JACoW-IPAC2018-MOPMF058. http://jacow.org/ipac2018/papers/mopmf058.pdf

[63] K. Lasocha and D. Alves, "Estimation of longitudinal bunch characteristics in the lhc using schottky-based diagnostics," *Phys. Rev. Accel. Beams*, vol. 23, p. 062803, Jun 2020. https://doi.org/10.1103/PhysRevAccelBeams.23.062803

[64] K. Lasocha and D. Alves, "Estimation of transverse bunch characteristics in the lhc using schottky-based diagnostics," *Phys. Rev. Accel. Beams*, vol. 25, p. 062801, Jun 2022. https://doi.org/10.1103/PhysRevAccelBeams.25.062801

[65] K. Lasocha, D. Harryman, T. Lefèvre, N. Mounet, and A. Schloegelhofer, "Simulation of Cherenkov Diffraction Radiation for Various Radiator Designs," *Proc. 9th International Beam Instrumentation Conference*, 10 2020, https://doi.org/10.18429/JACoW-IBIC2020-TUPP28. https://www.jacow.org/ibic2020/papers/tupp28.pdf

[66] K. Lasocha *et al.*, "Feasibility Study of ChDR Diagnostic Device in the LHC," *Proc. 12th International Particle Accelerator Conference*, 08 2021. https://doi.org/10.18429/JACoW-IPAC2021-TUPAB283

[67] K. Lasocha *et al.*, "Experimental Verification of Several Theoretical Models for ChDR Description," *Proc. 13th International Particle Accelerator Conference*, 2022.

[68] F. Caspers and D. Möhl, "History of stochastic beam cooling and its application in many different projects," *The European Physical Journal H*, vol. 36, no. 4, 2012. https://doi.org/10.1140/epjh/e2012-20037-8

[69] A. Sukhanov *et al.*, "Processing of the Schottky Signals at RHIC," *Proc. International Conference on Accelerator and Large Experimental Control Systems*, Jan. 2018. https://doi.org/10.18429/JACoW-ICALEPCS2017-THMPA08

[70] R. J. Pasquinelli and A. Jansson, "Microwave Schottky diagnostic systems for the Fermilab Tevatron, Recycler, and CERN Large Hadron Collider," *Phys. Rev. ST Accel. Beams*, vol. 14, p. 072803, Jul 2011. https://doi.org/10.1103/PhysRevSTAB.14.072803

[71] R. Singh *et al.*, "Interpretation of transverse tune spectra in a heavy-ion synchrotron at high intensities," *Phys. Rev. ST Accel. Beams*, vol. 16, p. 034201, Mar 2013. https://doi.org/10.1103/PhysRevSTAB.16.034201

[72] M. E. Castro *et al.*, "Results from the SPS 1.7 GHz travelling wave Schottky monitor," *Proc. 7th European Workshop on Beam Diagnostics and Instrumentation for Particle Accelerators*, Apr 2005. http://cds.cern.ch/record/895158

[73] J. Bosser, "Measurements on the low-intensity beams of LEAR and the antiproton accumulator," *Proc. 2nd European Workshop on Beam Diagnostics and Instrumentation for Particle Accelerators*, Jun 1995. https://cds.cern.ch/record/284270

[74] M. E. Angoletta *et al.*, "Beam Measurement Systems for the CERN Antiproton Decelerator (AD)," *Proc. 19th IEEE Particle Accelerator Conference*, Jul 2001. https://cds.cern.ch/record/510663

[75] L. Søby *et al.*, "Elena Orbit and Schottky Measurement Systems," *Proc. 6th International Particle Accelerator Conference*, 2015. https://cds.cern.ch/record/2141807

[76] C. McGillem and G. Cooper, *Continuous and Discrete Signal and System Analysis*, Oxford series in electrical and computer engineering. Oxford University Press, 1991. https://doi.org/10.1093/oso/9780198860792.001.0001

[77] D. Alves and K. Lasocha, "Kalman filter-based longitudinal phase-space reconstruction method for hadron machines," *Phys. Rev. Accel. Beams*, vol. 24, p. 072801, Jul 2021. https://doi.org/10.1103/PhysRevAccelBeams.24.072801

[78] M. Abramowitz and I. A. Stegun, *Handbook of Mathematical Functions with Formulas, Graphs, and Mathematical Tables*, 9th ed. Dover, 1964. https://doi.org/10.1119/1.15378

[79] D. W. Ricker, *Echo signal processing.* New York: Springer, 2012, vol. 725. https://doi.org/10.1007/978-1-4615-0312-5

[80] J. L. Laclare, "Bunched beam coherent instabilities," *CAS - CERN Accelerator School: Accelerator Physics course*, 1987. https://cds.cern.ch/record/611596

[81] M. Betz, M. Wendt, and T. Lefevre, "Summary of LHC MD 377: Schottky pick-up," *LHC MD Notes*, Nov 2015. http://cds.cern.ch/record/2110648

[82] F. Caspers, "Schottky signals for longitudinal and transverse bunched-beam diagnostics," *Proc. CERN Accelerator School: Beam Diagnostics course*, 2009. https://cds.cern.ch/record/1213284

[83] S. Paret *et al.*, "Transverse Schottky and beam transfer function measurements in space charge affected coasting ion beams," *Phys. Rev. ST Accel. Beams*, vol. 13, p. 022802, Feb 2010. https://doi.org/10.1103/PhysRevSTAB.13.022802

[84] D. Boussard, "Schottky noise and beam transfer function diagnostics," *Proc. CERN Accelerator School: Advanced Accelerator Physics course*, 1995. https://cds.cern.ch/record/302475

[85] S. van der Meer, "Diagnostics with Schottky noise," *Proc. 3rd Joint US-CERN School on Particle Accelerators*, 1988. https://cds.cern.ch/record/195311

[86] A. Jansson, P. Lebrun, and R. Pasquinelli, "Experience with the 1.7 GHz Schottky Pick-ups in the Tevatron," *Proc. 9th European Particle Accelerator Conference*, 7 2004. https://accelconf.web.cern.ch/e04/PAPERS/THPLT135.pdf

[87] L. Schwartz, *Théorie des distributions, t. 1-2.* Paris: Hermann, 1951. https://cds.cern.ch/record/268690

[88] W. N. Bailey, "Some series of squares of Bessel functions," *Mathematical Proceedings of the Cambridge Philosophical Society*, vol. 26, no. 1, 1930. https://doi.org/10.1017/S0305004100015048

[89] R. Storn and K. Price, "Differential evolution - a simple and efficient heuristic for global optimization over continuous spaces," *Journal of Global Optimization*, vol. 11, 01 1997. https://doi.org/10.1023/A:1008202821328

[90] R. Byrd *et al.*, "A limited memory algorithm for bound constrained optimization," *SIAM Journal of Scientific Computing*, vol. 16, Sep. 1995. https://doi.org/10.1137/0916069

[91] A. Abdi *et al.*, "On the estimation of the K parameter for the Rice fading distribution," *IEEE Communications Letters*, vol. 5, no. 3, March 2001. https://doi.org/10.1109/4234.913150

[92] O. Chanon, "Schottky signal analysis: tune and chromaticity computation," *CERN Student Notes*, Sep 2016. https://cds.cern.ch/record/2212811

[93] E. Jones, T. Oliphant, P. Peterson *et al.*, "SciPy: Open source scientific tools for Python," 2001–. http://www.scipy.org/

[94] E. Shaposhnikova, T. Bohl, and T. Linnecar, "Longitudinal peak detected schottky spectrum," *Proc. 46th ICFA Advanced Beam Dynamics Workshop*, Jan 2010. https://accelconf.web.cern.ch/HB2010/papers/tuo1c04.pdf

[95] F. Tecker, "Longitudinal beam dynamics," 2014, cAS - CERN Accelerator School: Advanced Accelerator Physics course. https://cds.cern.ch/record/1982417

[96] A. S. Hassan and L. C. Kennedy, "Accelerating Schottky Analysis," *CERN Student Notes*, Aug 2021. https://cds.cern.ch/record/2778266

[97] L. C. Kennedy, "Accelerating Schottky Analysis pt. II," *CERN Student Notes*, Sep 2021. http://cds.cern.ch/record/2780270

[98] S. K. Lam, A. Pitrou, and S. Seibert, "Numba: A LLVM-based Python JIT compiler," *Proc. 2nd Workshop on the LLVM Compiler Infrastructure in HPC*, 2015. https://doi.org/10.1145/2833157.2833162

[99] C. Lattner and V. Adve, "LLVM: A Compilation Framework for Lifelong Program Analysis & Transformation," *Proc. 2004 International Symposium on Code Generation and Optimization*, Mar 2004. https://llvm.org/pubs/2004-01-30-CGO-LLVM.html

[100] S. G. Nash, "A survey of truncated-newton methods," *Journal of Computational and Applied Mathematics*, vol. 124, no. 1, 2000. https://doi.org/10.1016/S0377-0427(00)00426-X

[101] M. J. D. Powell, "An efficient method for finding the minimum of a function of several variables without calculating derivatives," *The Computer Journal*, vol. 7, no. 2, 1964. https://doi.org/10.1093/comjnl/7.2.155

[102] C. Zannini *et al.*, "Bunch by bunch tune shifts for HL-LHC: tune separation along the bunch train," *173rd HiLumi WP2 Meeting*, 2020. https://indico.cern.ch/event/903324/#23-tune-separation-along-the-b

[103] T. M. Apostol, *Introduction to analytic number theory.* New York: Springer, 1976. https://doi.org/10.1007/978-1-4757-5579-4

[104] O. Marqversen and S. Jensen, "Schottky Signal From Distributed Orbit Pick-Ups," *Proc. 10th International Beam Instrumentation Conference*, 2021. https://doi.org/10.18429/JACoW-IBIC2021-WEPP04

[105] P. Cherenkov, "Visible radiation produced by electrons moving in a medium with velocities exceeding that of light," *Physical Review*, vol. 52, no. 4, 1937. https://doi.org/10.1103/PhysRev.52.378

[106] I. Frank and I. Tamm, *Coherent Visible Radiation of Fast Electrons Passing Through Matter*. Berlin, Heidelberg: Springer, 1991, pp. 29–35. https://doi.org/10.1007/978-3-642-74626-0_2

[107] V. L. Ginzburg and I. M. Frank, *Doklady Akad. Nauk S.S.S.R.*, vol. 56, no. 699, 1947.

[108] J. G. Linhart, "Čerenkov Radiation of Electrons Moving Parallel to a Dielectric Boundary," *Journal of Applied Physics*, vol. 26, no. 5, 1955. https://doi.org/10.1063/1.1722033

[109] R. Ulrich, "Zur Cerenkov-Strahlung von Elektronen dicht über einem Dielektrikum," *Zeitschrift fur Physik*, vol. 194, no. 2, Apr. 1966. https://doi.org/10.1007/BF01326045

[110] E. Senes, *Development of a beam position monitor for co-propagating electron and proton beams*, 2020, Doctoral Thesis. https://cds.cern.ch/record/2753708

[111] A. Curcio *et al.*, "Noninvasive bunch length measurements exploiting Cherenkov diffraction radiation," *Phys. Rev. Accel. Beams*, vol. 23, p. 022802, Feb 2020. https://doi.org/10.1103/PhysRevAccelBeams.23.022802

[112] R. Kieffer *et al.*, "Direct observation of incoherent Cherenkov diffraction radiation in the visible range," *Phys. Rev. Lett.*, vol. 121, p. 054802, Aug 2018. https://doi.org/10.1103/PhysRevLett.121.054802

[113] R. Kieffer *et al.*, "Generation of incoherent Cherenkov diffraction radiation in synchrotrons," *Phys. Rev. Accel. Beams*, vol. 23, p. 042803, Apr 2020. https://doi.org/10.1103/PhysRevAccelBeams.23.042803

[114] D. M. Harryman *et al.*, "First measurements of Cherenkov-diffraction radiation at Diamond Light Source," *Proc. 8th Int. Beam Instrumentation Conference*, 2019. https://doi.org/10.18429/JACoW-IBIC2019-WEPP037

[115] K. Fedorov *et al.*, "Experimental observation of submillimeter coherent Cherenkov radiation at CLARA facility," *Proc. 8th Int. Beam Instrumentation Conference*, 2019. https://doi.org/10.18429/JACoW-IBIC2019-TUCO02

[116] S. Ninomiya *et al.*, "Measurement of Cherenkov diffraction radiation from a short electron bunches at t-ACTS," *Proc. 10th Int. Particle Accelerator Conference*, 2019. https://doi.org/10.18429/JACoW-IPAC2019-WEPGW031

[117] A. V. Tyukhtin, S. N. Galyamin, and V. V. Vorobev, "Peculiarities of cherenkov radiation from a charge moving through a dielectric cone," *Phys. Rev. A*, vol. 99, p. 023810, Feb 2019. https://doi.org/10.1103/PhysRevA.99.023810

[118] S. N. Galyamin, V. V. Vorobev, and A. V. Tyukhtin, "Radiation of a charge in dielectric concentrator for cherenkov radiation: Off-axis charge motion," *Phys. Rev. Accel. Beams*, vol. 22, p. 083001, Aug 2019. https://doi.org/10.1103/PhysRevAccelBeams.22.083001

[119] S. N. Galyamin and A. V. Tyukhtin, "Cherenkov radiation of a charge in axicon-based dielectric concentrator," *Phys. Rev. Accel. Beams*, vol. 23, p. 113001, Nov 2020. https://doi.org/10.1103/PhysRevAccelBeams.23.113001

[120] A. V. Tyukhtin *et al.*, "Cherenkov radiation of a charge flying through the inverted conical target," *Phys. Rev. A*, vol. 102, p. 053514, Nov 2020. https://doi.org/10.1103/PhysRevA.102.053514

[121] A. V. Tyukhtin, S. N. Galyamin, and V. V. Vorobev, "Cherenkov radiation from a hollow conical target: off-axis charge motion," *J. Opt. Soc. Am. B*, vol. 39, no. 3, Mar 2022. https://doi.org/10.1364/JOSAB.439682

[122] D. V. Karlovets and A. P. Potylitsyn, "Universal description for different types of polarization radiation," 2009, arXiv preprint. https://doi.org/10.48550/arXiv.0908.2336

[123] B. Bolotovskii, "Teoriya effekta Vavilova-Cherenkova," *Uspekhi Fizicheskikh Nauk*, vol. 75, no. 10, 1961.

[124] H. A. Olsen and H. Kolbenstvedt, "Čerenkov radiation and transition radiation from small systems: Čerenkov radiation generated in a cylinder," *Phys. Rev. A*, vol. 21, Jun 1980. https://doi.org/10.1103/PhysRevA.21.1987

[125] M. Danos, "Čerenkov Radiation from Extended Electron Beams," *Journal of Applied Physics*, vol. 26, no. 1, 1955. https://doi.org/10.1063/1.1721856

[126] M. Amusia, "Atomic Bremsstrahlung: Retrospectives, current status and perspectives," *Radiation Physics and Chemistry*, vol. 75, no. 10, 2006. https://doi.org/10.1016/j.radphyschem.2006.04.009

[127] A. P. Potylitsyn and S. Y. Gogolev, "Radiation Losses of the Relativistic Charge Moving Near a Dielectric Radiator," *Russian Physics Journal*, vol. 62, no. 12, Apr. 2020. https://doi.org/10.1007/s11182-020-01965-0

[128] D. V. Karlovets and A. P. Potylitsyn, "Diffraction radiation from a finite-conductivity screen," *Journal of Experimental and Theoretical Physics Letters*, vol. 90, no. 5, Nov. 2009. https://doi.org/10.1134/S0021364009170032

[129] O. Grimm and P. Schmüser, "Principles of longitudinal beam diagnostics with coherent radiation." *Proc. 10th European Particle Accelerator Conference*, Jan 2006. https://cds.cern.ch/record/972240

[130] O. Grimm *et al.*, "Transverse Electron Beam Size Effect on the Bunch Profile Determination with Coherent Radiation Diagnostics," *Proc. 11th European Particle Accelerator Conference*, 2008. https://accelconf.web.cern.ch/e08/papers/tupc030.pdf

[131] D. Gamba *et al.*, "The CLEAR user facility at CERN," *Nuclear Instruments and Methods in Physics Research Section A*, vol. 909, 2018. https://doi.org/10.1016/j.nima.2017.11.080

[132] J. W. Strutt, "The problem of the random walk," *Nature*, vol. 72. https://doi.org/10.1038/072318a0

[133] R. Kitamura, L. Pilon, and M. Jonasz, "Optical constants of silica glass from extreme ultraviolet to far infrared at near room temperature," *Appl. Opt.*, vol. 46, no. 33, Nov 2007. https://doi.org/10.1364/AO.46.008118

[134] "CST Studio Suite," 2008. http://www.cst.com

[135] N. Mounet, "The LHC Transverse Coupled-Bunch Instability," 2012, Doctoral Thesis. https://doi.org/10.5075/epfl-thesis-5305

[136] S. Bochkanov, "Alglib." https://www.alglib.net

[137] D. Griffiths and I. Smith, *Numerical Methods for Engineers: A Programming Approach.* Blackwell Scientific Publications, 1991.

[138] M. Galassi *et al.*, "Gnu scientific library reference manual," 2018. https://www.gnu.org/software/gsl/

[139] M. T. Sebastian, "Chapter two - measurement of microwave dielectric properties and factors affecting them," in *Dielectric Materials for Wireless Communication.* Amsterdam: Elsevier, 2008. https://doi.org/10.1016/B978-0-08-045330-9.00002-9

[140] P. Drude, "Zur Elektronentheorie der Metalle; II. Teil. Galvanomagnetische und thermomagnetische Effecte," *Annalen der Physik*, vol. 308, no. 11, Jan. 1900. https://doi.org/10.1002/andp.19003081102

[141] E. Peralta *et al.*, "Demonstration of electron acceleration in a laser-driven dielectric microstructure," *Nature*, vol. 503, 09 2013. https://doi.org/10.1038/nature12664

[142] S. Liu *et al.*, "Surface Polariton Cherenkov Light Radiation Source," *Phys. Rev. Lett.*, vol. 109, p. 153902, Oct 2012. https://doi.org/10.1103/PhysRevLett.109.153902

[143] R. Cimino *et al.*, "Can low-energy electrons affect high-energy physics accelerators?" *Phys. Rev. Lett.*, vol. 93, p. 014801, Jun 2004. https://doi.org/10.1103/PhysRevLett.93.014801

[144] R. Salemme *et al.*, "Vacuum performance of amorphous carbon coating at cryogenic temperature with presence of proton beams," *Proc. 7th Int. Particle Accelerator Conference*, 2016. https://doi.org/10.18429/JACoW-IPAC2016-THPMY007

[145] B. Salvant, N. Wang, C. Zannini, "Update on new triplet beam screen impedance," Dec 2015, presented at Impedance Working Group meeting. https://indico.cern.ch/event/467922/

[146] G. Apollinari *et al.*, *High-Luminosity Large Hadron Collider (HL-LHC): Technical Design Report V. 0.1*, CERN Yellow Reports: Monographs. Geneva: CERN, 2017. https://cds.cern.ch/record/2284929

[147] A. Schloegelhofer, *Cherenkov diffraction radiation in beam diagnostics - investigation of a potential tool for FCC-ee*, 2020, Master Thesis. http://cds.cern.ch/record/2750140

[148] A. Papoulis and S. U. Pillai, *Probability, Random Variables, and Stochastic Processes*, 4th ed. Boston: McGraw Hill, 2002.

APPENDIX A
APPENDIX

The aim of this appendix is to derive formula which relates the longitudinal bunch profile with the distribution of synchrotron amplitudes, Eq. (2.25). For highly populated bunches under stationary conditions, the longitudinal bunch profile, denoted by $\mathcal{B}(\tau)$, can be interpreted as a probability distribution of finding a particle with the temporal delay τ with respect to the synchronous particle. Moreover, the assumption of no coherent intra-bunch motion implies that the distribution of initial synchrotron phases, φ_s, is independent of the distribution of synchrotron amplitudes $\widehat{\tau}$ and uniform. As a result, the probability of finding any particle with the time difference τ with respect to the synchronous particle can be written as a function of its amplitude of oscillations $\widehat{\tau}$ only. The bunch profile can be then expressed as

$$\mathcal{B}(\tau) = \int_0^\infty g_{\tau,\widehat{\tau}}(\tau,\widehat{\tau})d\widehat{\tau} = \int_{|\tau|}^\infty g_{\tau,\widehat{\tau}}(\tau,\widehat{\tau})d\widehat{\tau},$$

where $g_{\tau,\widehat{\tau}}(\tau,\widehat{\tau})$ is the joint probability density of a particle having synchrotron amplitude and a temporal delay with respect to the synchronous particle.

Obtaining the explicit form of $g_{\tau,\widehat{\tau}}(\tau,\widehat{\tau})$ is not straightforward, as τ and $\widehat{\tau}$ are not independent, but it can be derived from the joint distribution of initial synchrotron phases and amplitudes $g_{\varphi_s,\widehat{\tau}}$. One can write

$$g_{\varphi_s,\widehat{\tau}}\left(\varphi_s,\widehat{\tau}\right) = g_{\varphi_s}\left(\varphi_s\right) g_{\widehat{\tau}}\left(\widehat{\tau}\right) = \frac{g_{\widehat{\tau}}\left(\widehat{\tau}\right)}{2\pi}, \tag{A.1}$$

as these random variables are independent and φ_s is uniformly distributed. In addition, let us define the transformation

$$u = (u_1, u_2) : (\varphi_s, \widehat{\tau}) \mapsto (\tau, \widehat{\tau}),$$

where u_1 comes from Eq. (2.2) and u_2 is the identity function of $\widehat{\tau}$:

$$\begin{aligned} u_1\left(\varphi_s,\widehat{\tau}\right) &= \widehat{\tau}\cos\left(\Omega_s t + \varphi_s\right), \\ u_2\left(\varphi_s,\widehat{\tau}\right) &= \widehat{\tau}. \end{aligned}$$

Conversely, having the pair $(\tau,\widehat{\tau})$, one can determine φ_s as one of the following:

$$\begin{aligned} \phi_{s_a}(\tau,\widehat{\tau}) &= \arccos\left(\frac{\tau}{\widehat{\tau}}\right), \\ \phi_{s_b}(\tau,\widehat{\tau}) &= 2\pi - \arccos\left(\frac{\tau}{\widehat{\tau}}\right). \end{aligned}$$

This gives two possible inverse transforms

$$u_i^{-1} = (v_{1,i}, v_2) : (\tau, \widehat{\tau}) \mapsto (\varphi_s, \widehat{\tau}),$$

where $i = a, b$ and functions $v_{1,i}, v_2$ are given by

$$\begin{aligned} v_{1,i}(\tau, \widehat{\tau}) =& \phi_{s_i}(\tau, \widehat{\tau}), \\ v_2(\tau, \widehat{\tau}) =& \widehat{\tau}. \end{aligned}$$

The relationship between the joint distributions of two sets of random variables related by known transformation functions is given in [148, p. 201]. Using this, one obtains

$$g_{\tau,\widehat{\tau}}(\tau, \widehat{\tau}) = \sum_{i=a,b} g_{\varphi_s,\widehat{\tau}}(v_{1,i}(\tau, \widehat{\tau}), v_2(\tau, \widehat{\tau})) \left\| \begin{matrix} \frac{\partial v_{1,i}}{\partial \tau} & \frac{\partial v_2}{\partial \tau} \\ \frac{\partial v_{1,i}}{\partial \widehat{\tau}} & \frac{\partial v_2}{\partial \widehat{\tau}} \end{matrix} \right\|,$$

where by $||\cdot||$ the absolute value of the determinant of a matrix is denoted. The Jacobian in the equation above can be calculated by noting, that $\frac{\partial v_2}{\partial \tau} = \frac{\partial \widehat{\tau}}{\partial \tau} = 0$ and $\frac{\partial v_2}{\partial \widehat{\tau}} = \frac{\partial \widehat{\tau}}{\partial \widehat{\tau}} = 1$, so

$$\left| \begin{matrix} \frac{\partial v_{1,i}}{\partial \tau} & \frac{\partial v_2}{\partial \tau} \\ \frac{\partial v_{1,i}}{\partial \widehat{\tau}} & \frac{\partial v_2}{\partial \widehat{\tau}} \end{matrix} \right| = \left| \begin{matrix} \frac{\partial v_{1,i}}{\partial \tau} & 0 \\ \frac{\partial v_{1,i}}{\partial \widehat{\tau}} & 1 \end{matrix} \right| = \frac{\partial v_{1,i}}{\partial \tau} = \pm \frac{1}{\sqrt{\widehat{\tau}^2 - \tau^2}}.$$

One has then that

$$\begin{aligned} g_{\tau,\widehat{\tau}}(\tau, \widehat{\tau}) =& \sum_{i=a,b} \frac{g_{\varphi_s,\widehat{\tau}}(v_{1,i}(\tau, \widehat{\tau}), v_2(\tau, \widehat{\tau}))}{\sqrt{\widehat{\tau}^2 - \tau^2}} = \\ =& \sum_{i=a,b} \frac{g_{\varphi_s}(v_{1,i}(\tau, \widehat{\tau})) g_{\widehat{\tau}}(v_2(\tau, \widehat{\tau}))}{\sqrt{\widehat{\tau}^2 - \tau^2}} = \\ =& \sum_{i=a,b} \frac{g_{\widehat{\tau}}(v_2(\tau, \widehat{\tau}))}{2\pi\sqrt{\widehat{\tau}^2 - \tau^2}} = \frac{g_{\widehat{\tau}}(v_2(\tau, \widehat{\tau}))}{\pi\sqrt{\widehat{\tau}^2 - \tau^2}} = \\ =& \frac{g_{\widehat{\tau}}(\widehat{\tau})}{\pi\sqrt{\widehat{\tau}^2 - \tau^2}}, \end{aligned}$$

where $g_{\varphi_s,\widehat{\tau}}$ are separated into the product of two distributions using Eq. (A.1). It allows to finally write

$$\mathcal{B}(\tau) = \int_{|\tau|}^{\infty} \frac{g_{\widehat{\tau}}(\widehat{\tau})}{\pi\sqrt{\widehat{\tau}^2 - \tau^2}} d\widehat{\tau}.$$